Frontier Orbitals of Photosubstitutionally Active Ruthenium Complexes: An Experimental Study of the Spectator Ligands' Electronic Properties Influence on Photoreactivity

Hyo Jin Jang,[a] Samantha L. Hopkins,[a] Maxime A. Siegler,[b] and Sylvestre Bonnet*[,a]

[a] Leiden Institute of Chemistry, Leiden University, Einsteinweg 55, 2300 RA Leiden, The Netherlands
[b] Small Molecule X-ray Facility, Department of Chemistry, Johns Hopkins University, Baltimore, Maryland 21218, United States

Corresponding author: bonnet@chem.leidenuniv.nl

Supporting Information

Contents

1. Synthesis and characterization of 4,4′ -bis(trifluoromethyl)-2,2′ -bipyridine

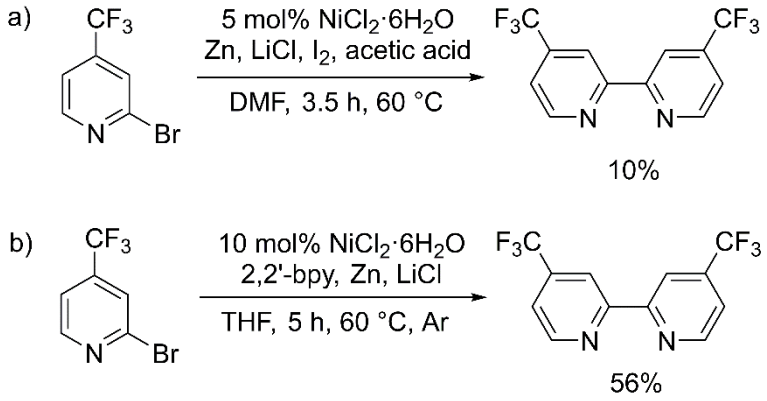

Scheme S1. Homocoupling reactions for the synthesis of the tfmbpy ligand. a) The result of applying the method by Liao *et al.* b) The result after the modifications.

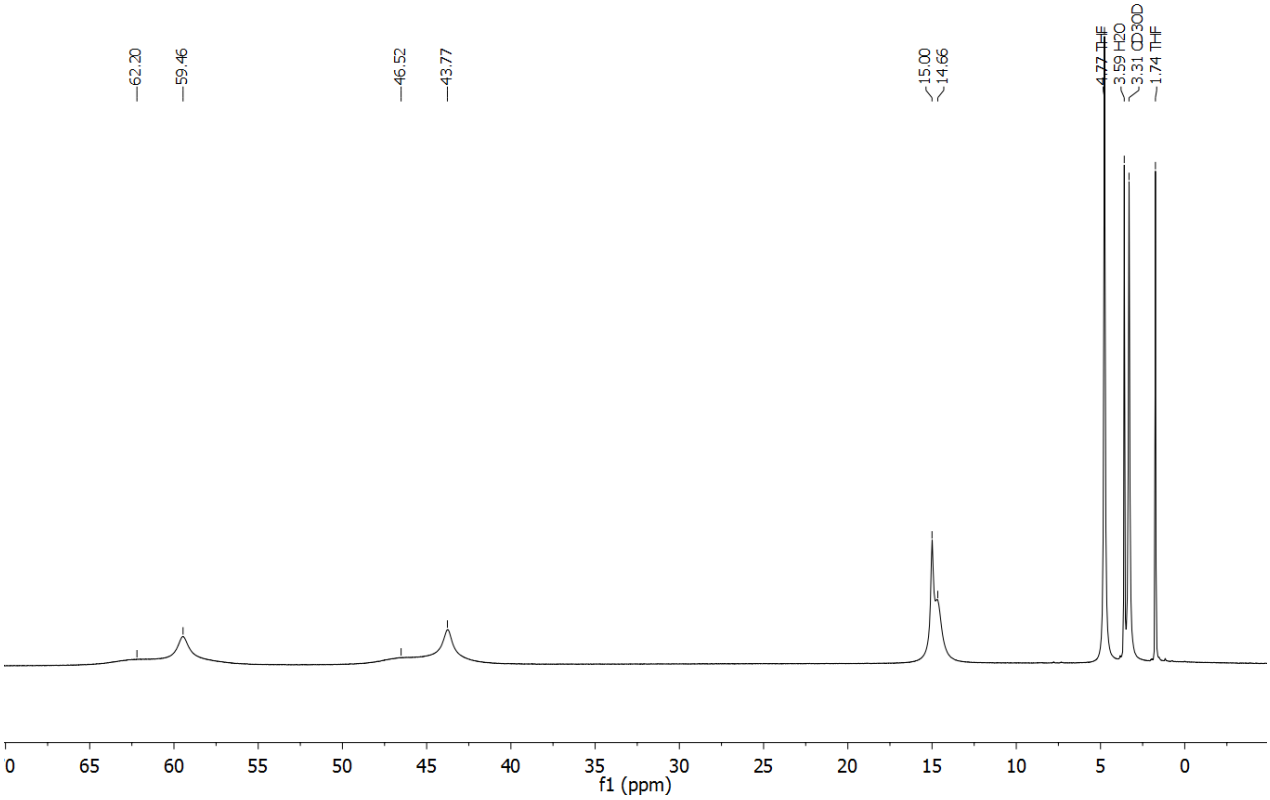

Figure S1. ^{1}H NMR (300 MHz, CD_3OD) spectrum taken after $NiCl_2{\cdot}6H_2O$ and 2,2′ -bpy were dissolved in THF at 40 °C ([Ni(bpy)Cl_2]).

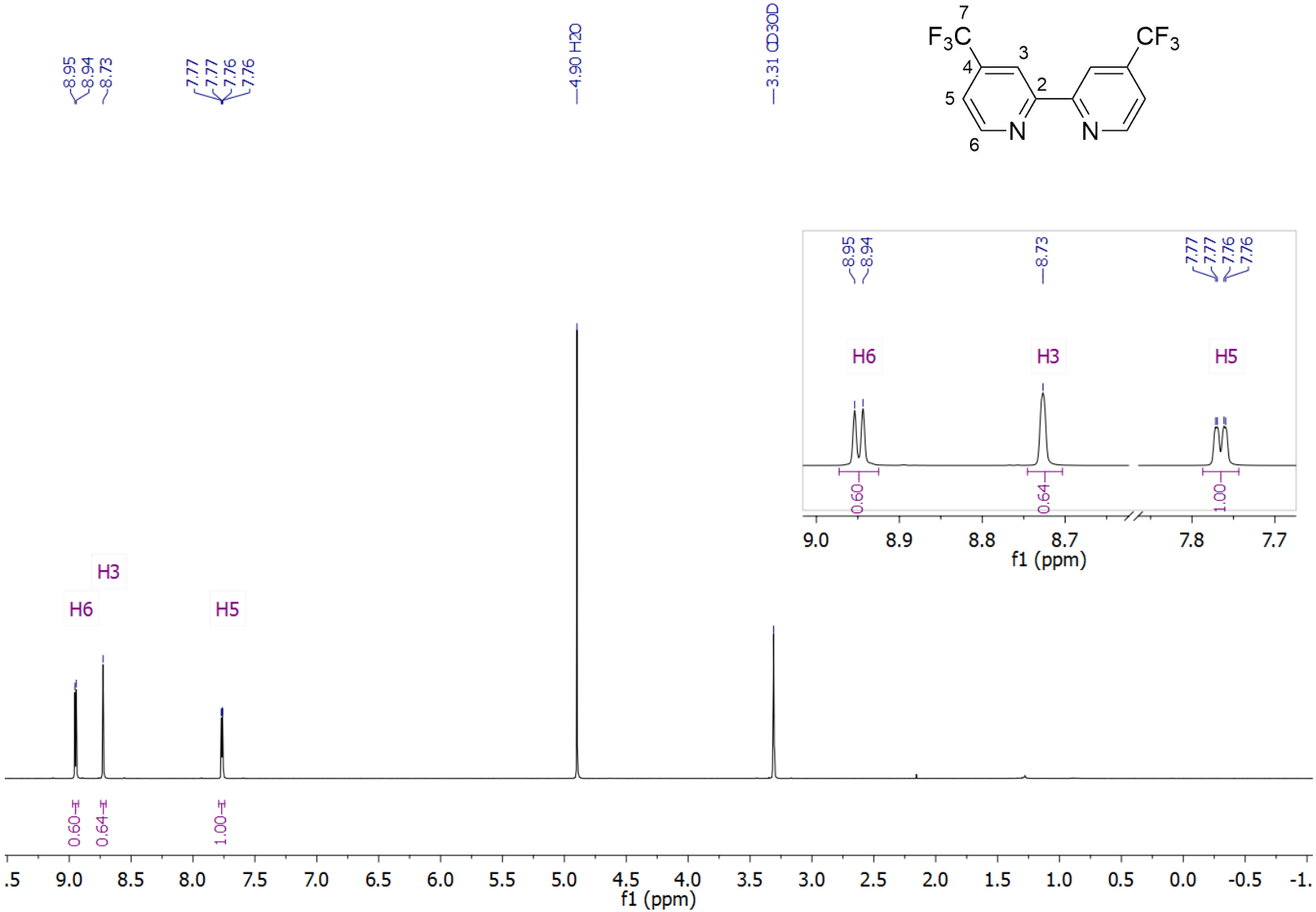

Figure S2. ^{1}H NMR (500 MHz, CD_3OD) of 4,4′ -bis(trifluoromethyl)-2,2′ -bipyridine.

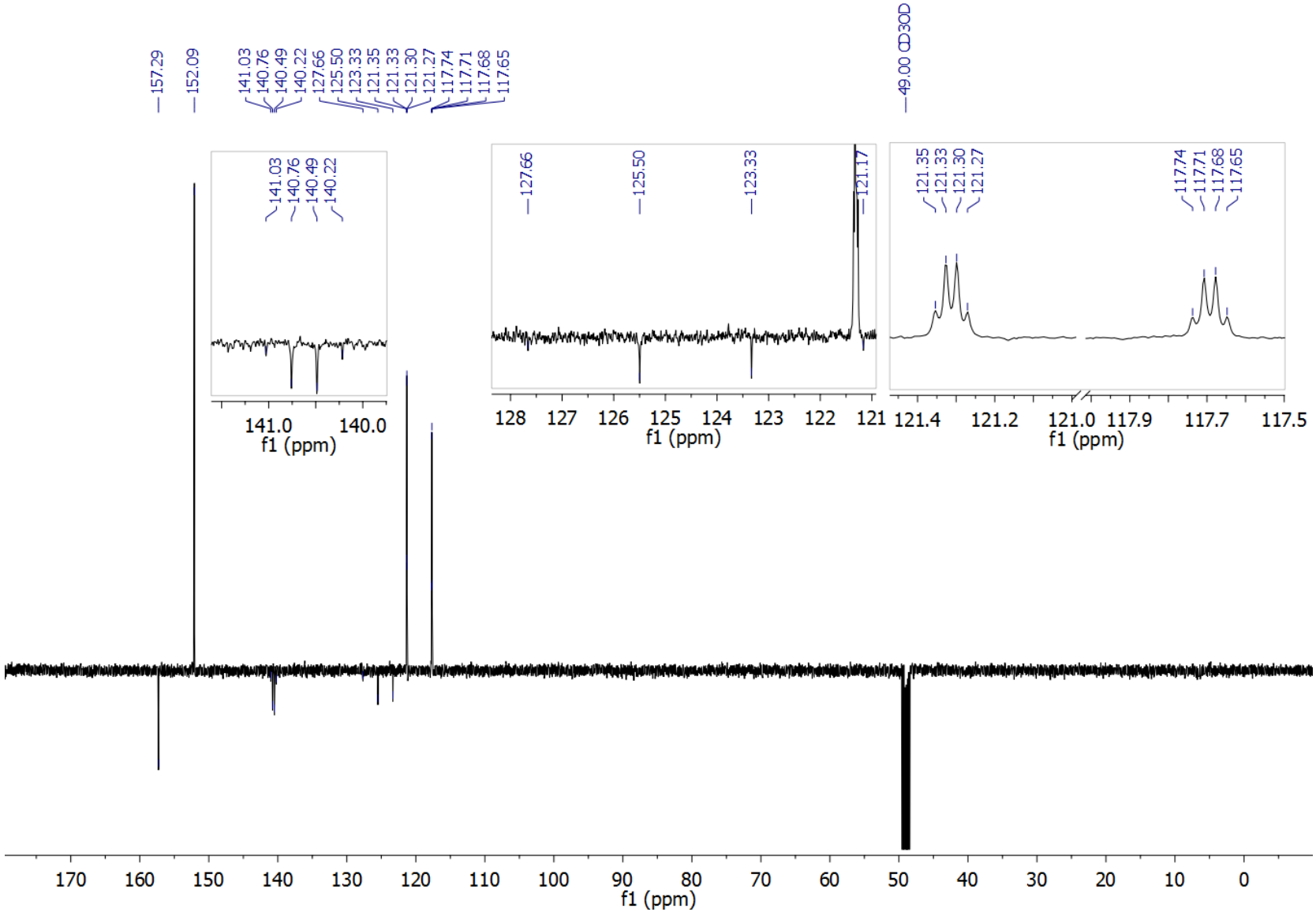

Figure S3. ^{13}C NMR (500 MHz, CD_3OD) of 4,4′ -bis(trifluoromethyl)-2,2′ -bipyridine.

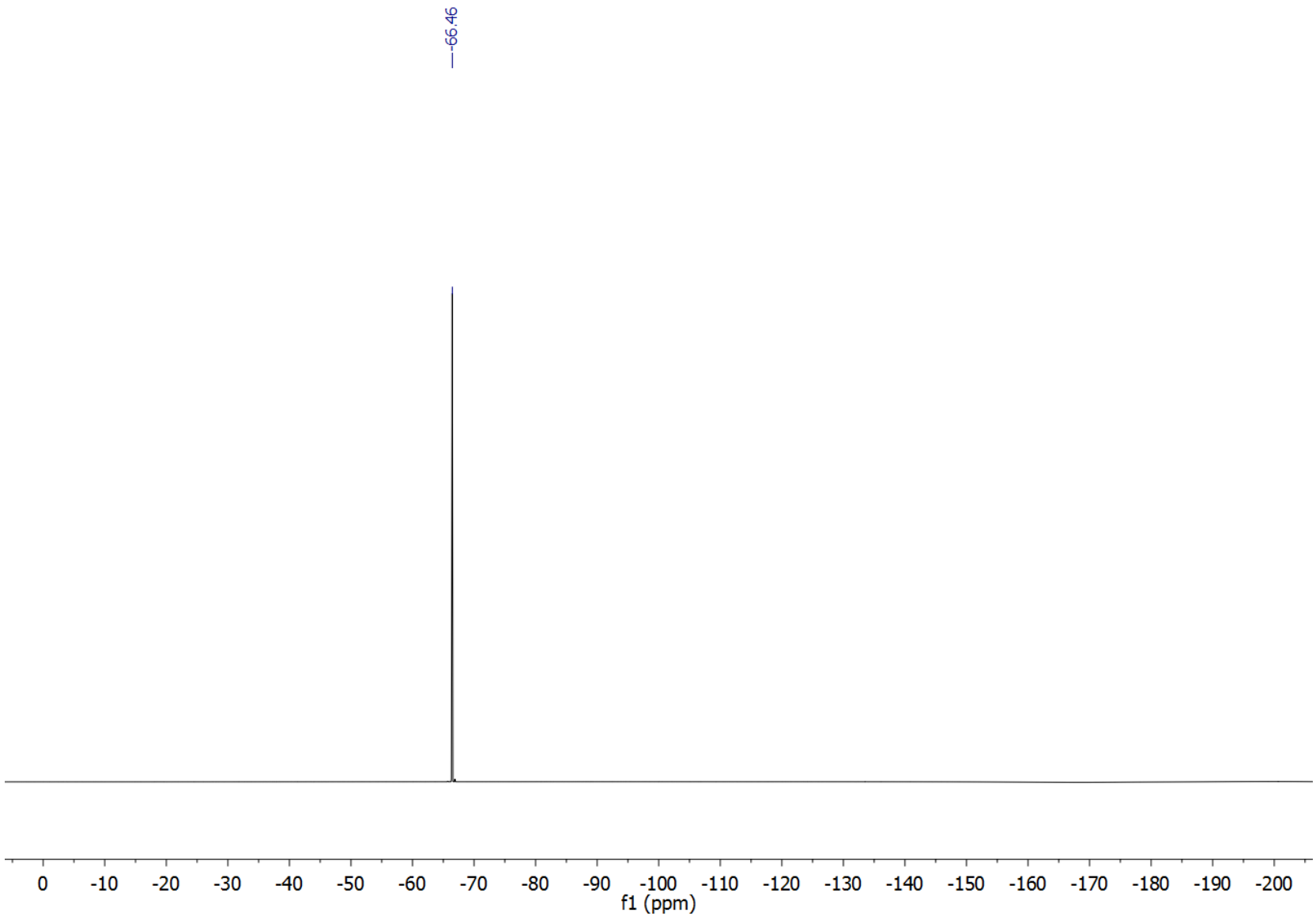

Figure S4. ^{19}F NMR (500 MHz, CD_3OD) of 4,4′ -bis(trifluoromethyl)-2,2′ -bipyridine.

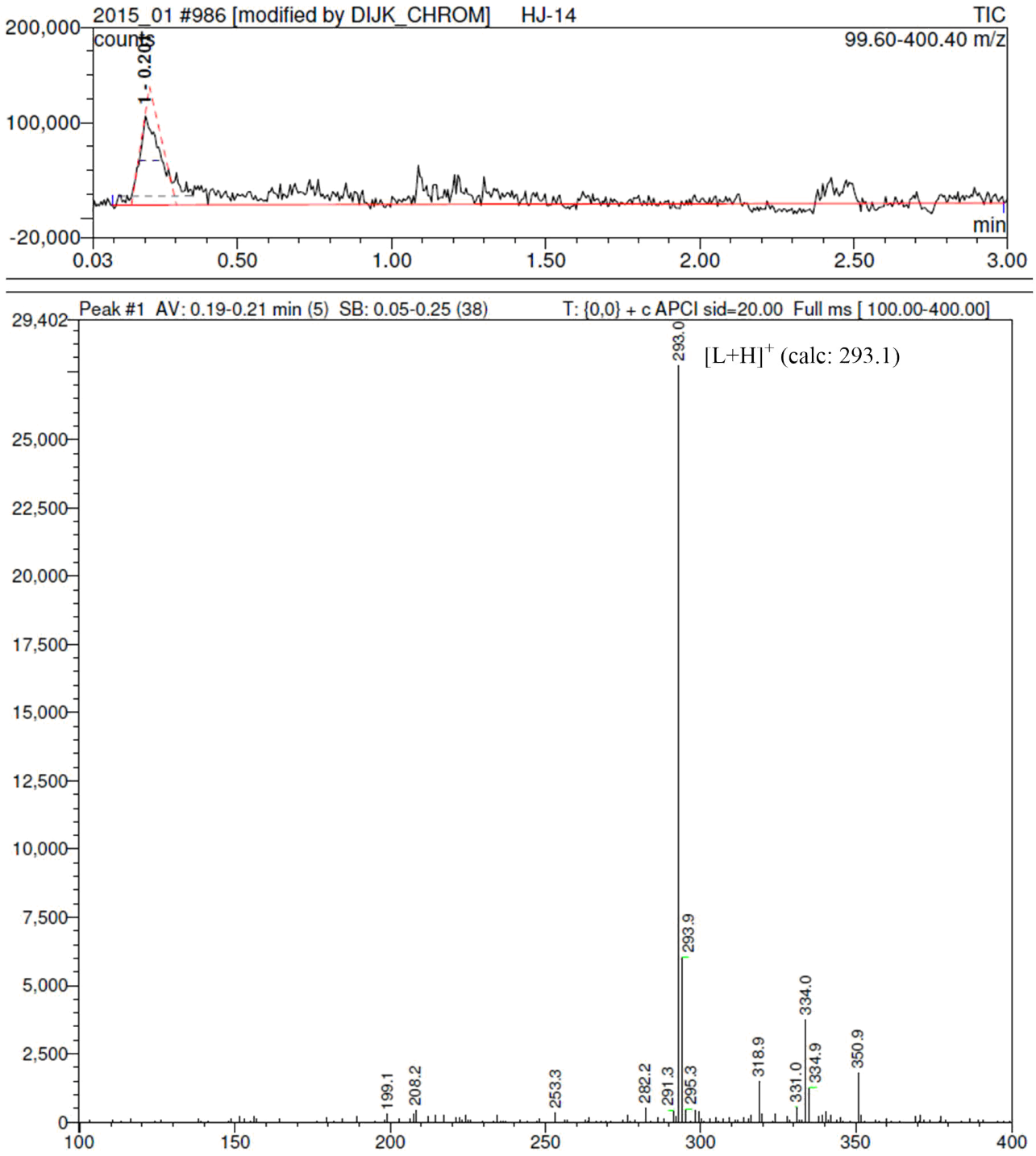

Figure S5. ES-MS of 4,4′ -bis(trifluoromethyl)-2,2′ -bipyridine

2. NMR spectra of the Ru complexes

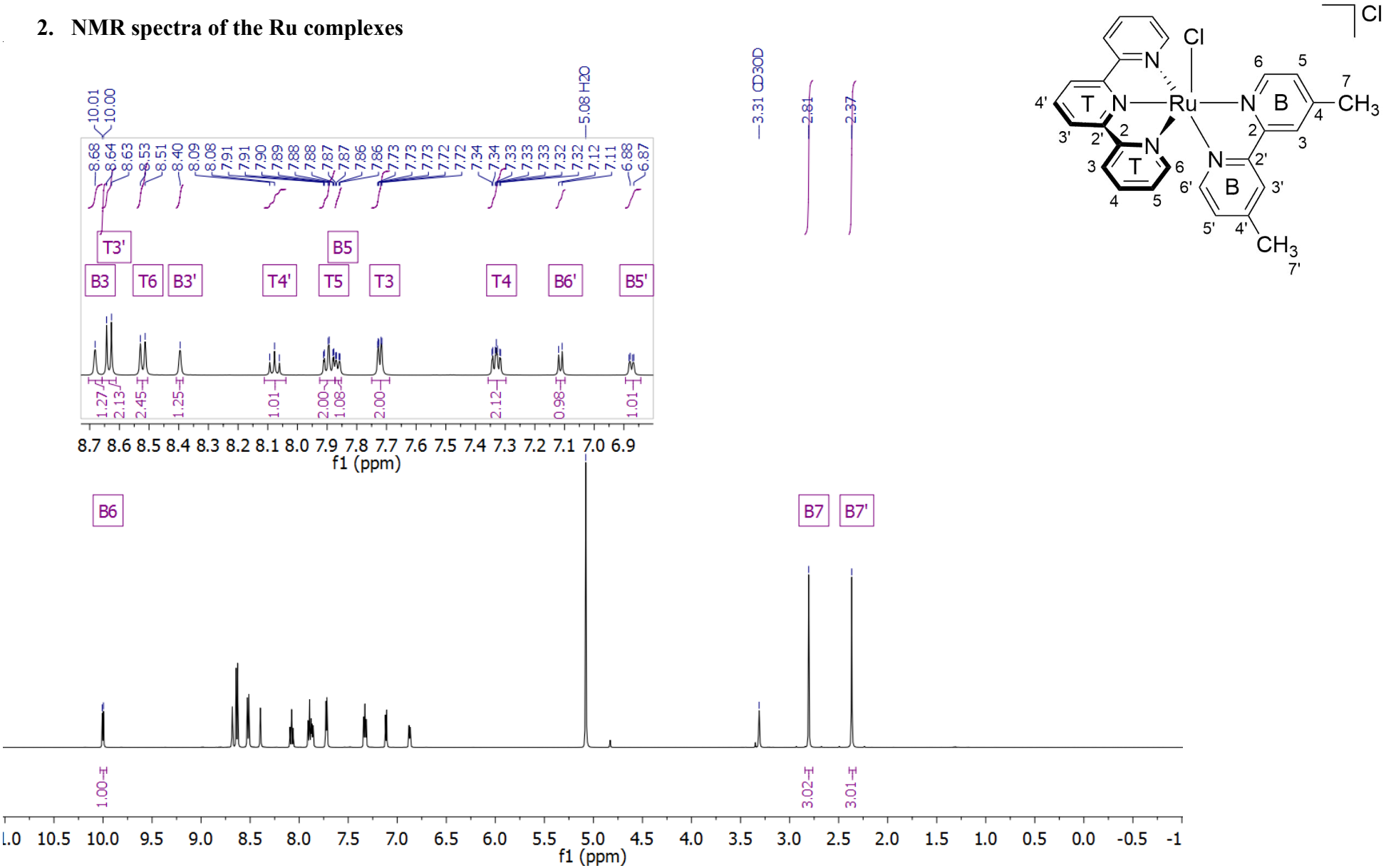

Figure S6. ^{1}H NMR (500 MHz, CD_3OD) of [Ru(tpy)(dmbpy)Cl]Cl, [**1**]Cl.

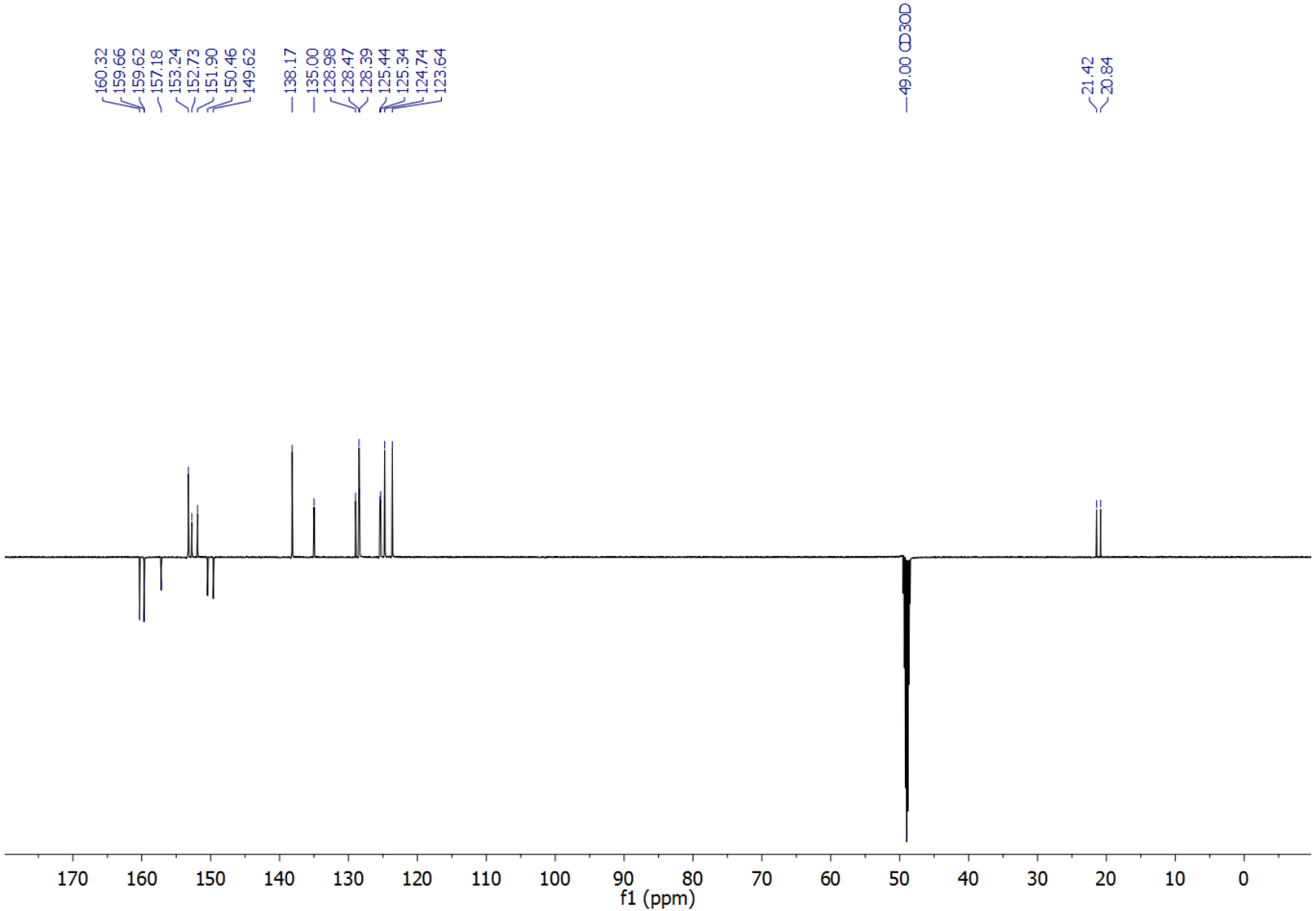

Figure S7. ^{13}C NMR (500 MHz, CD_3OD) of [Ru(tpy)(dmbpy)Cl]Cl, [**1**]Cl.

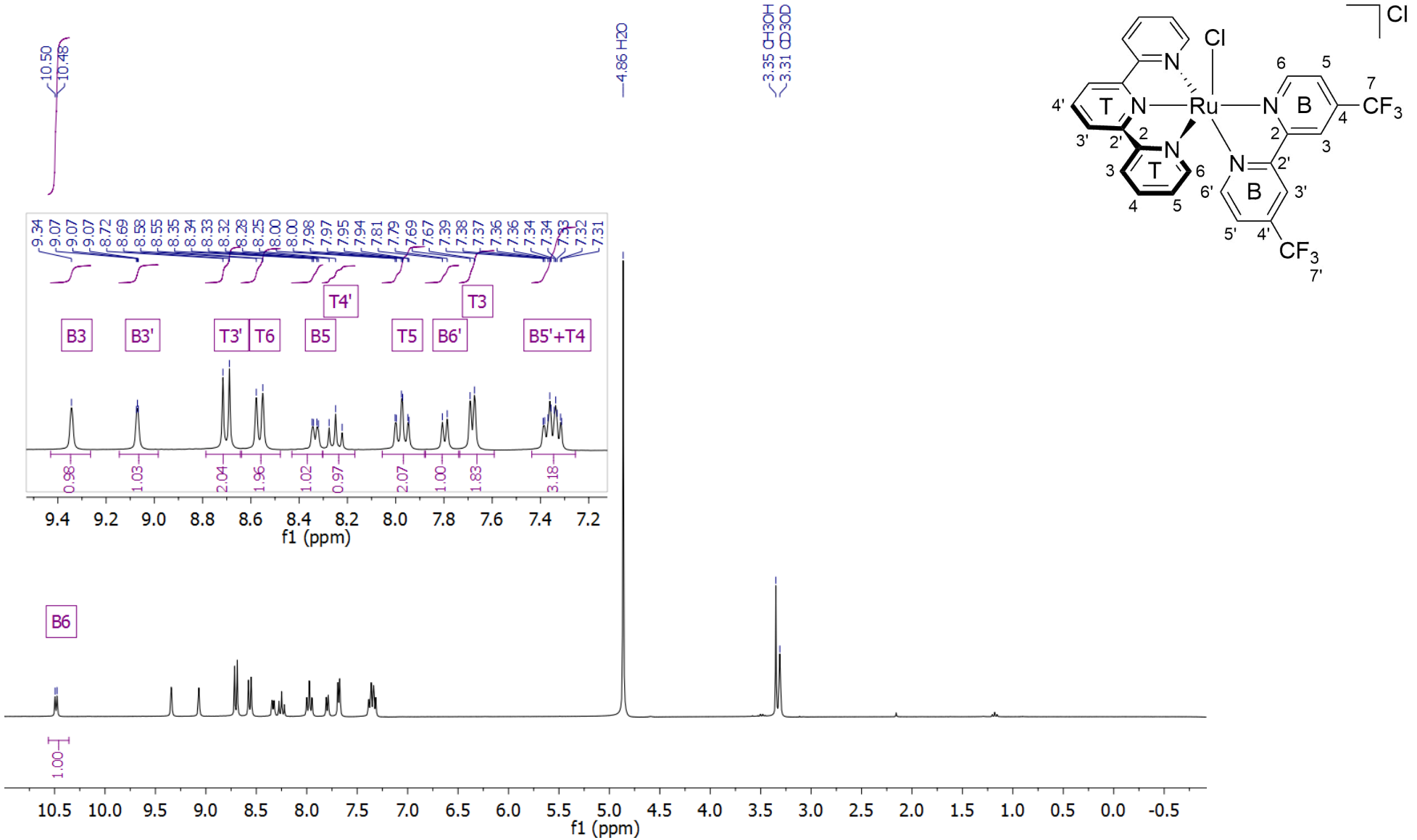

Figure S8. ^{1}H NMR (300 MHz, CD_3OD) of [Ru(tpy)(tfmbpy)Cl]Cl, [**2**]Cl.

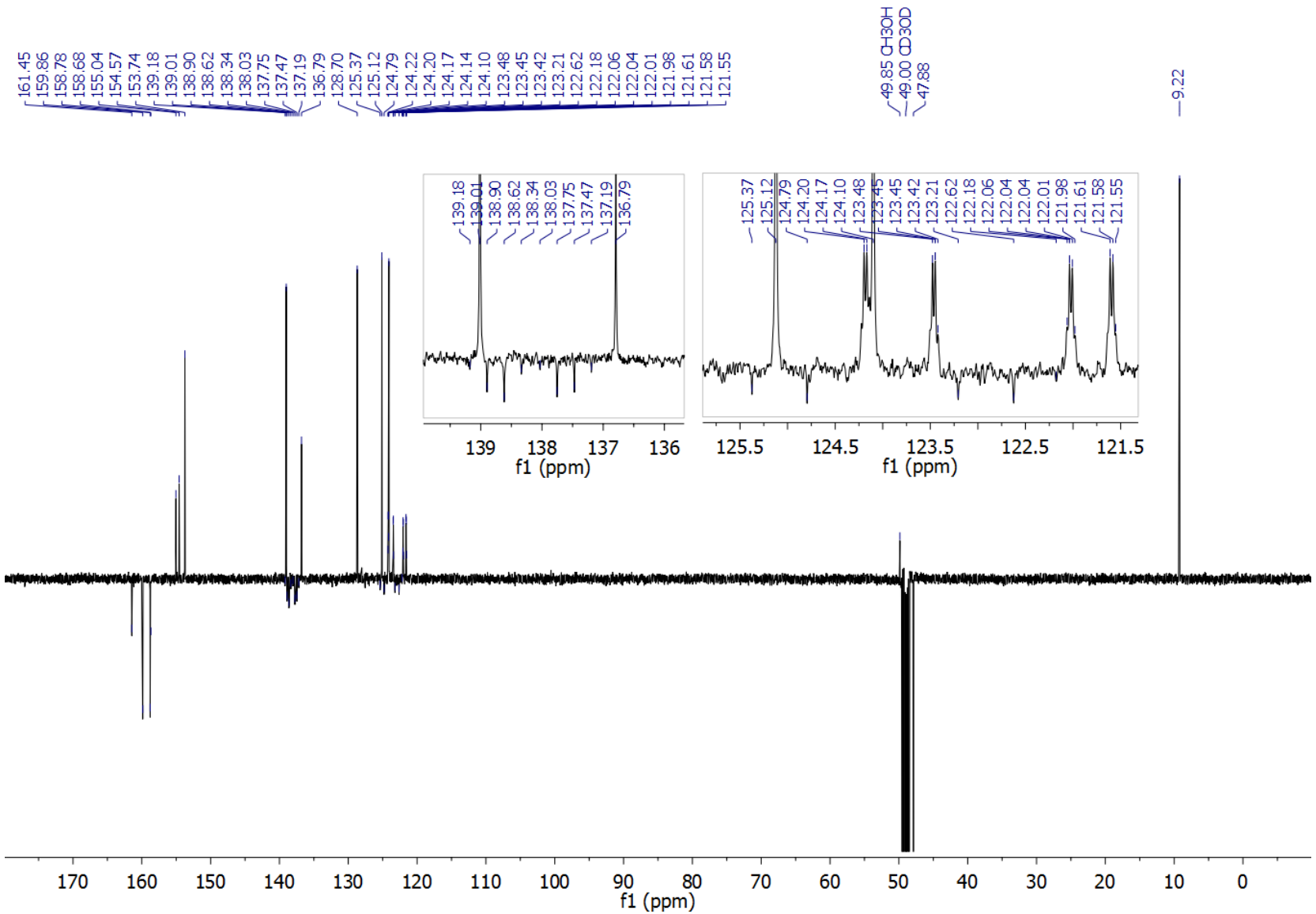

Figure S9. ^{13}C NMR (500 MHz, CD_3OD) of [Ru(tpy)(tfmbpy)Cl]Cl, [**2**]Cl.

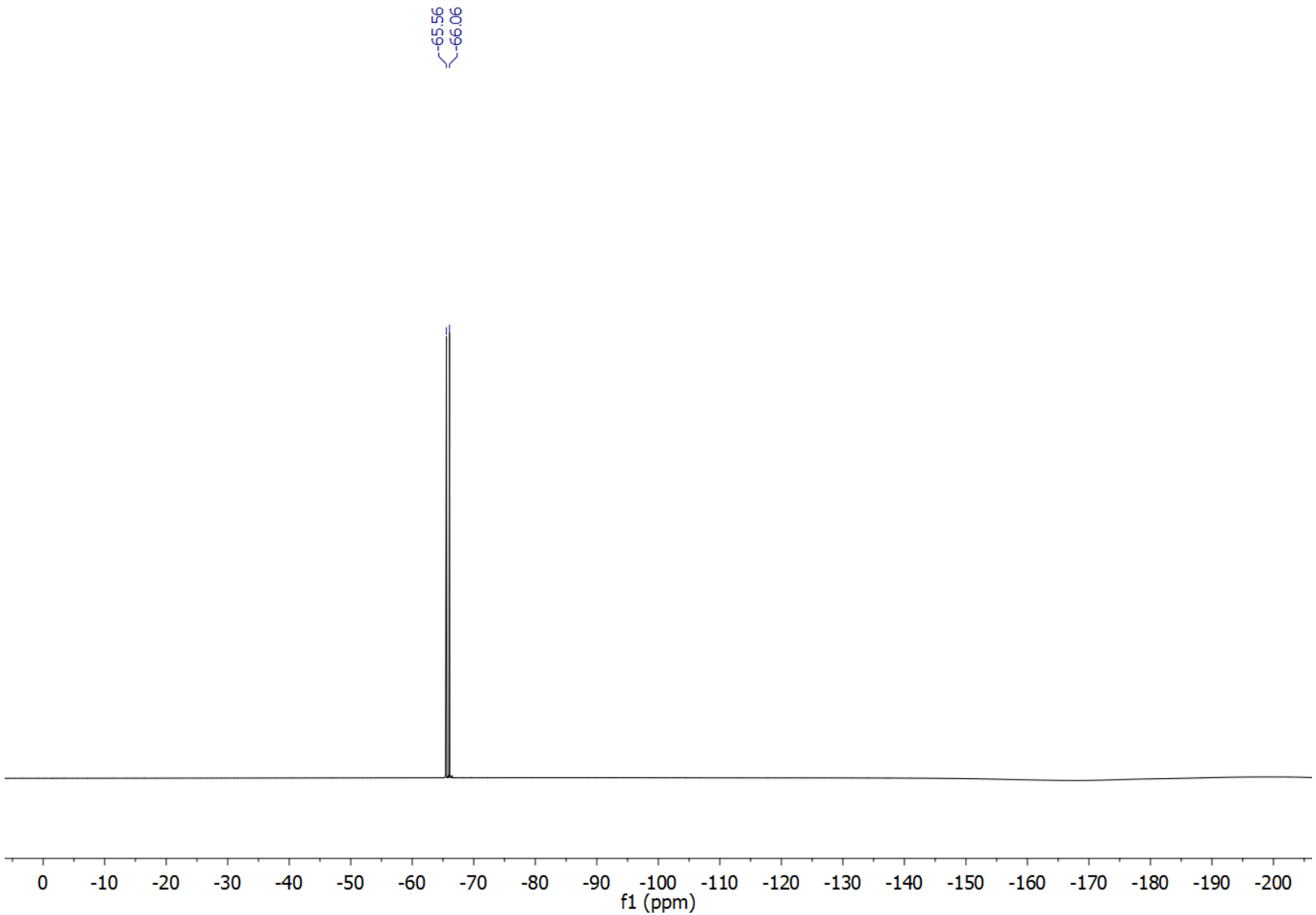

Figure S10. ^{19}F NMR (500 MHz, CD_3OD) of [Ru(tpy)(tfmbpy)Cl]Cl, [**2**]Cl.

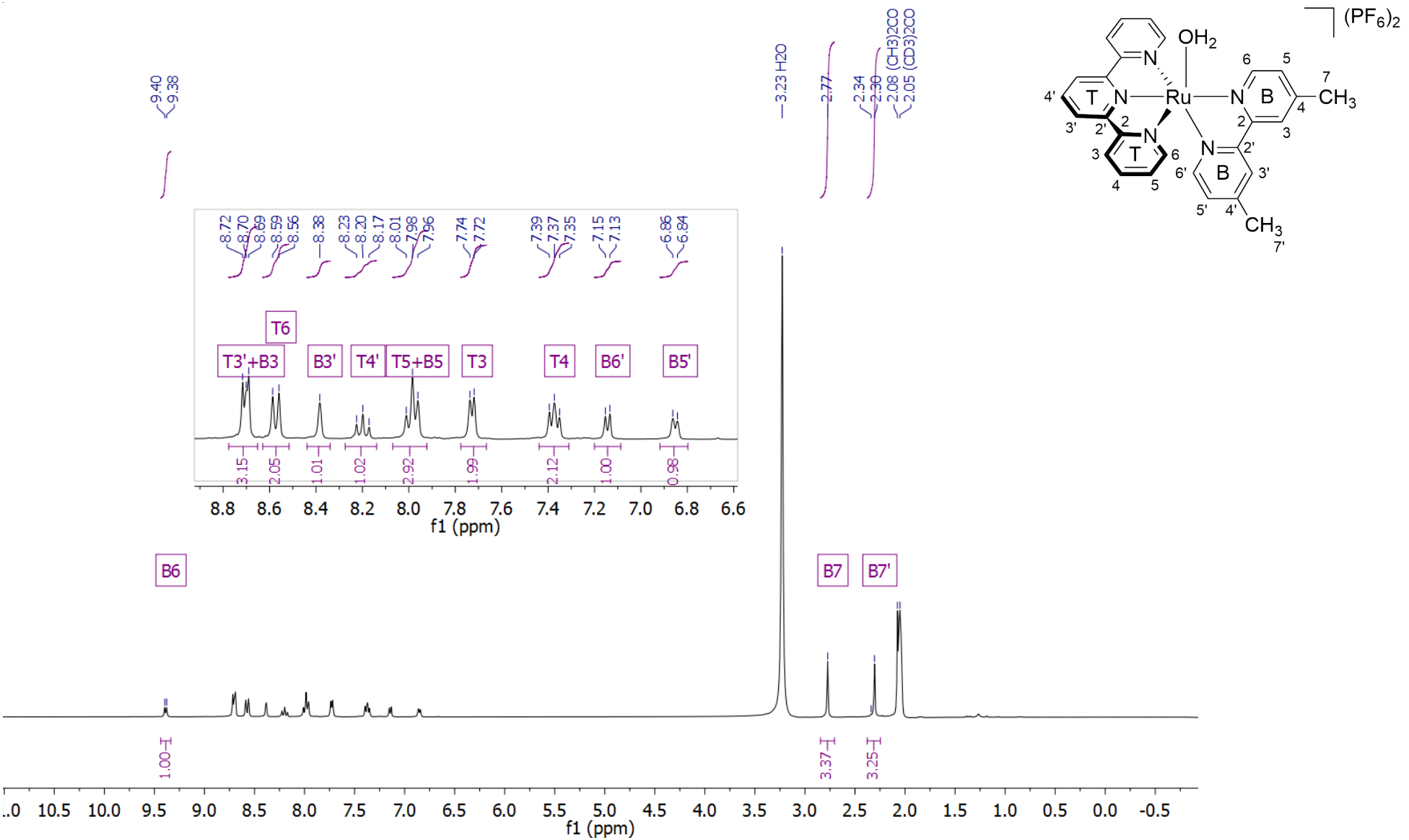

Figure S11. ^{1}H NMR (300 MHz, $(CD_3)_2CO$) of $[Ru(tpy)(dmbpy)(OH_2)](PF_6)_2$, [**3**]$(PF_6)_2$.

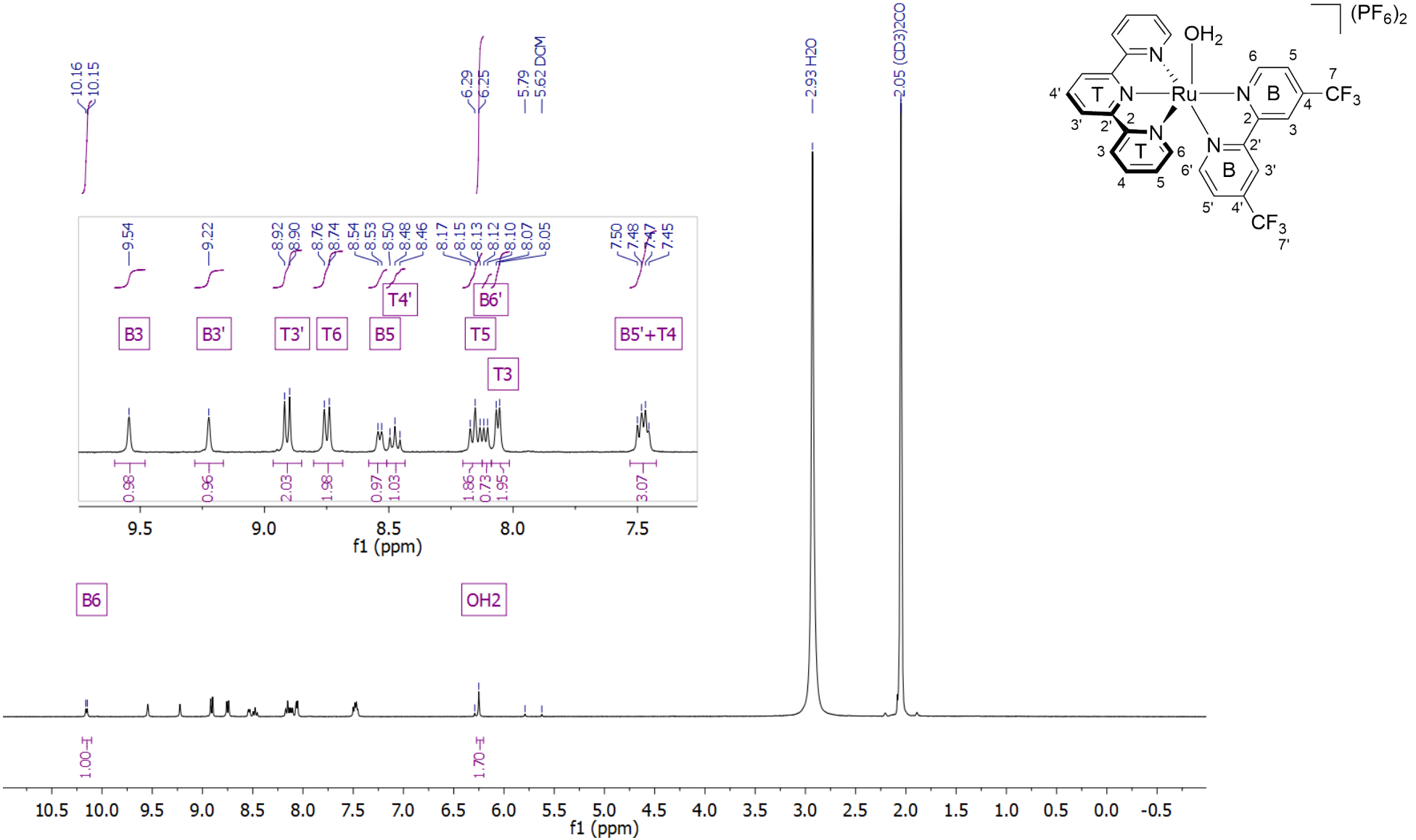

Figure S12. ^{1}H NMR (400 MHz, $(CD_3)_2CO$) of $[Ru(tpy)(tfmbpy)(OH_2)](PF_6)_2$, [**4**]$(PF_6)_2$.

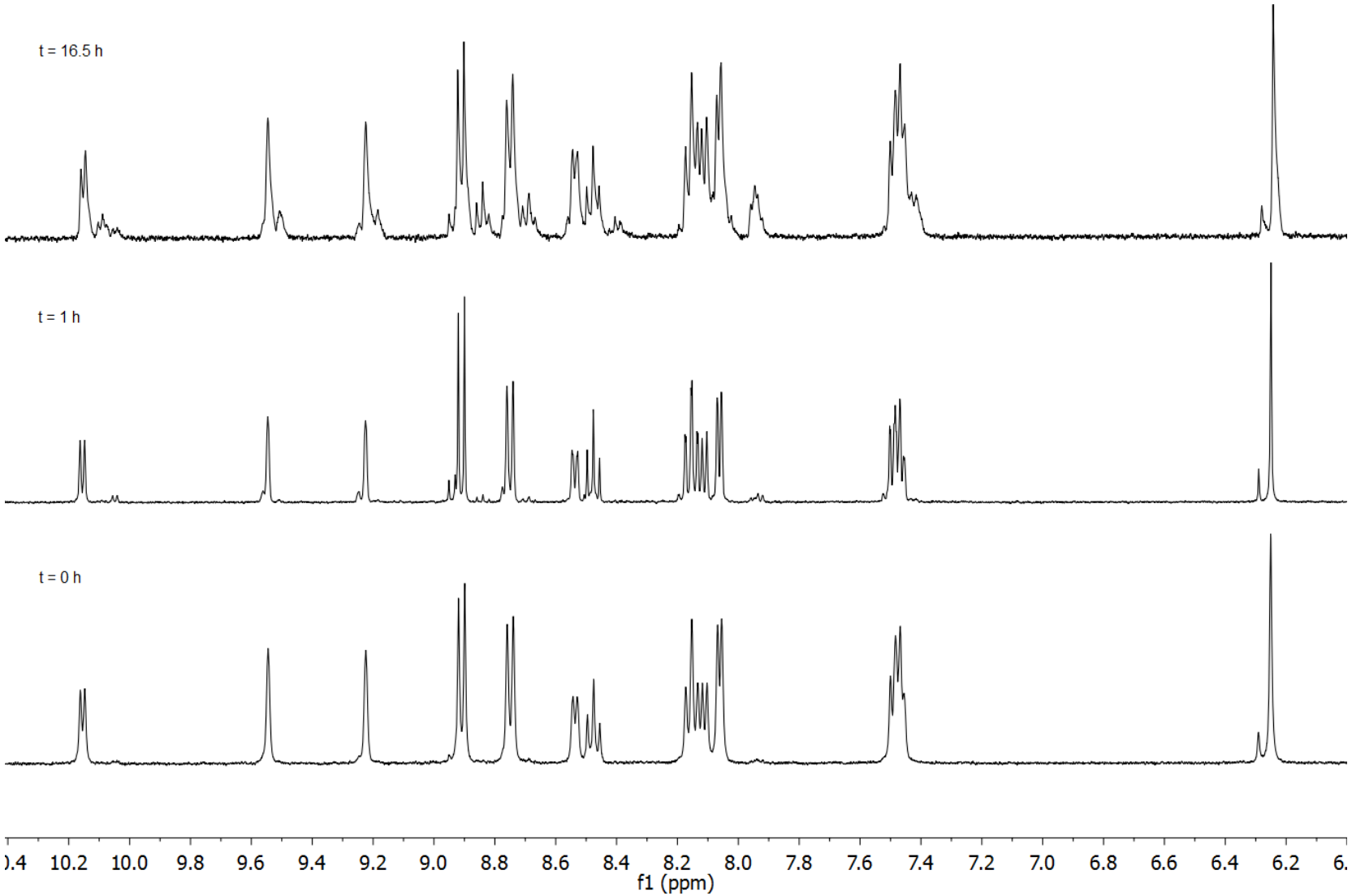

Figure S13. ^{1}H NMR (400 MHz, $(CD_3)_2CO$) of [**4**]$(PF_6)_2$ over time at room temperature. Due to the reactivity of [**4**]$(PF_6)_2$ with acetone, acetone was eliminated from the reaction conditions.

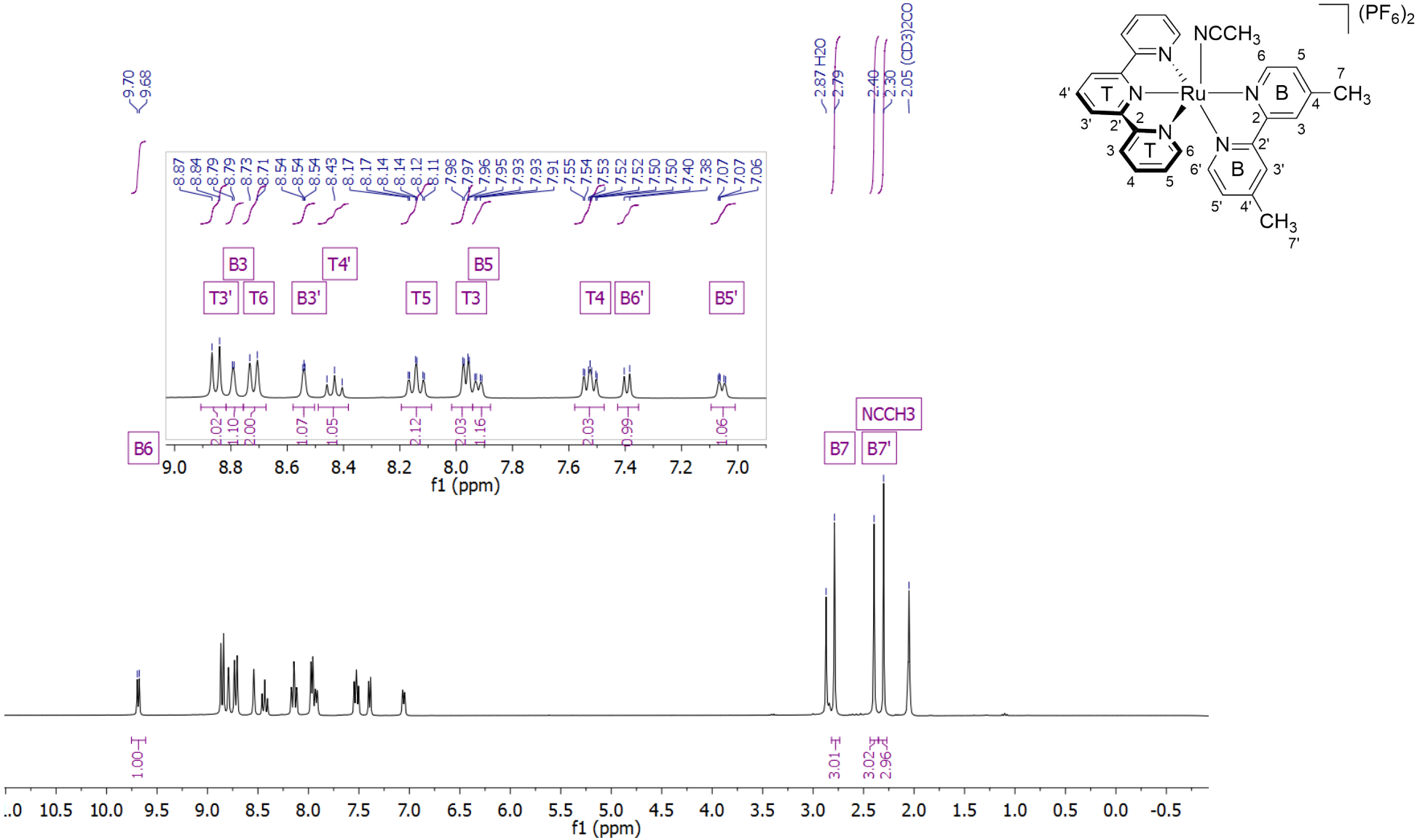

Figure S14. ^{1}H NMR (300 MHz, $(CD_3)_2CO$) of $[Ru(tpy)(dmbpy)(NCCH_3)](PF_6)_2$, [**5**]$(PF_6)_2$.

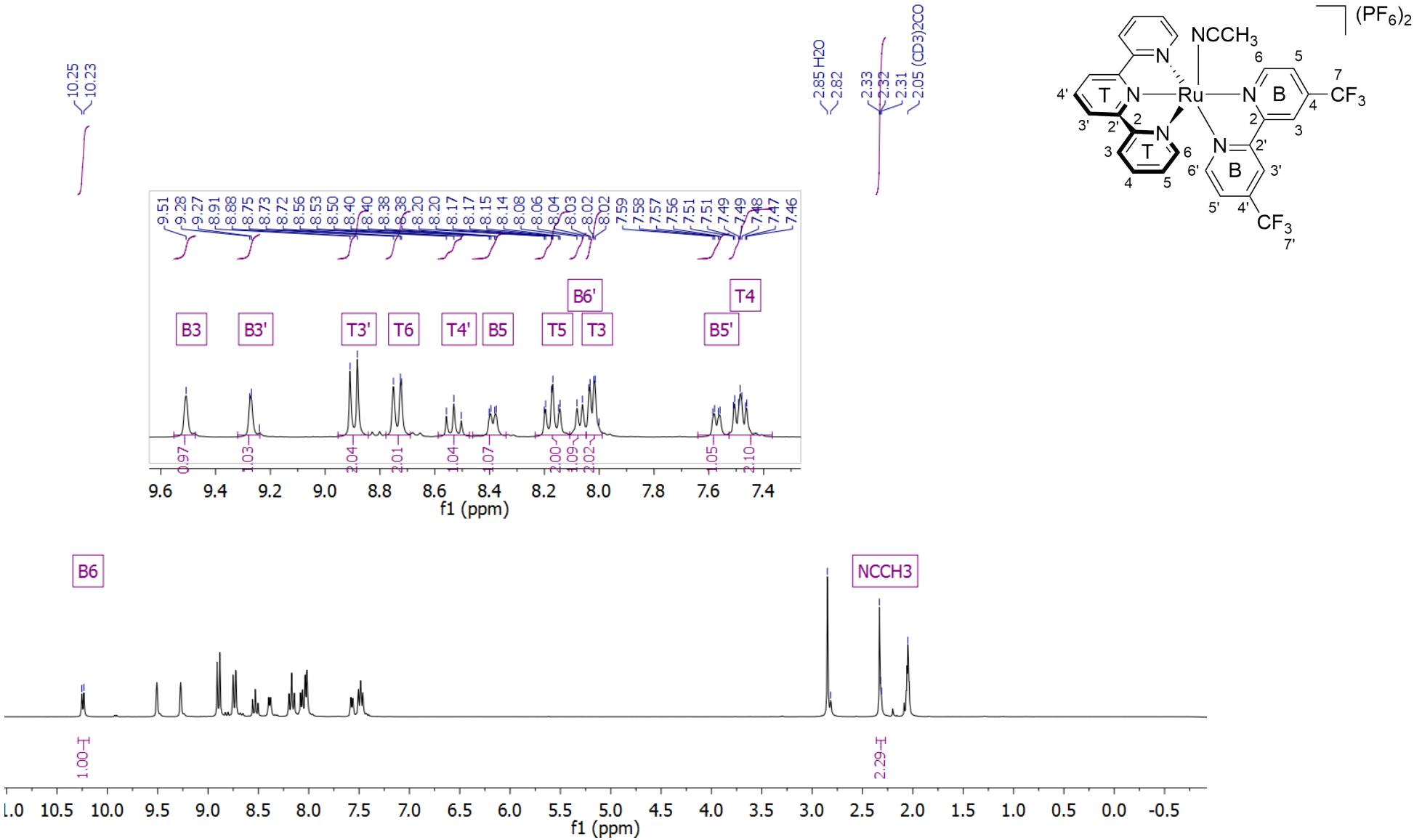

Figure S15. ^{1}H NMR (300 MHz, $(CD_3)_2CO$) of $[Ru(tpy)(tfmbpy)(NCCH_3)](PF_6)_2$, [**6**]$(PF_6)_2$

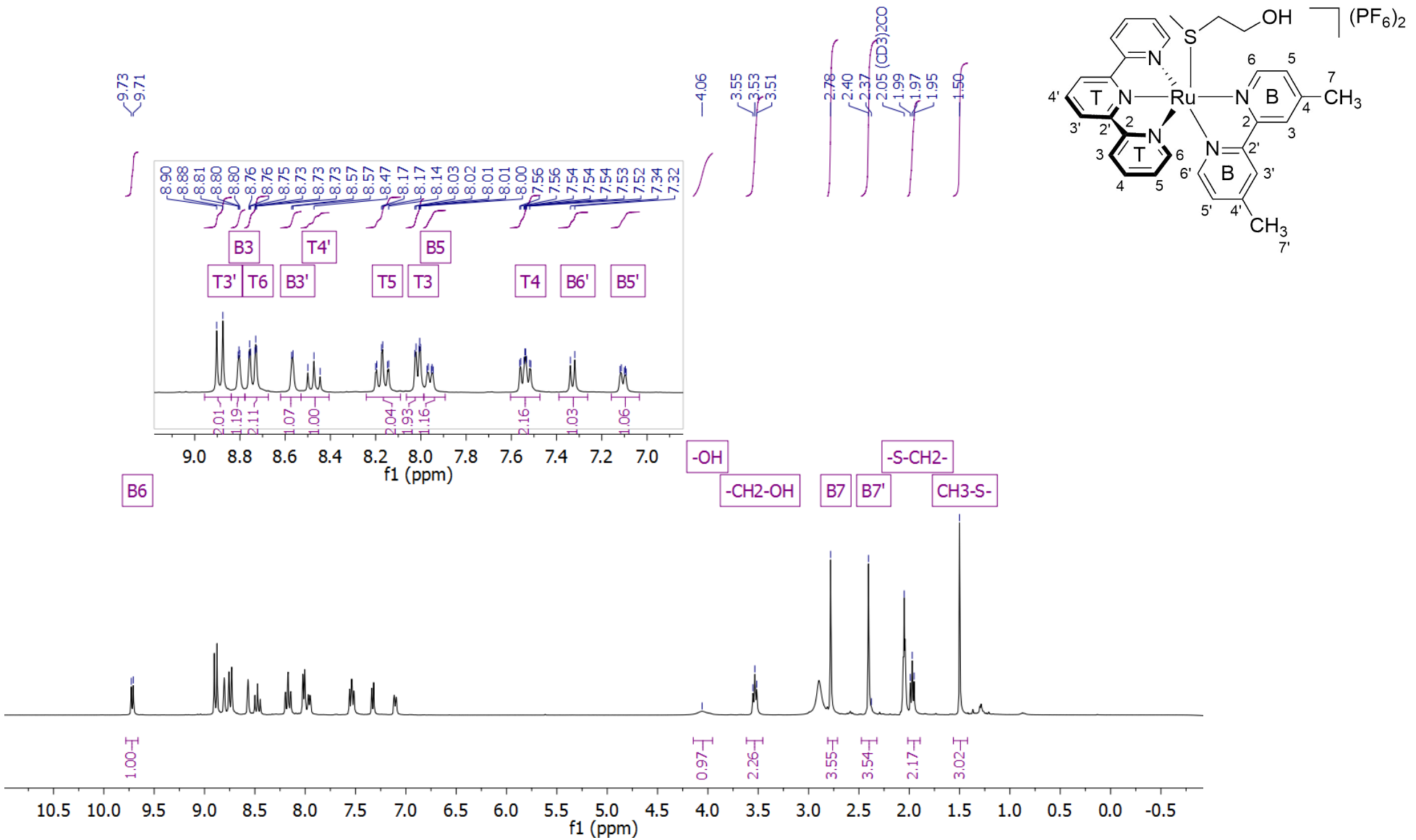

Figure S16. ^{1}H NMR (300 MHz, $(CD_3)_2CO$) of $[Ru(tpy)(dmbpy)(Hmte)](PF_6)_2$, **[7]**$(PF_6)_2$.

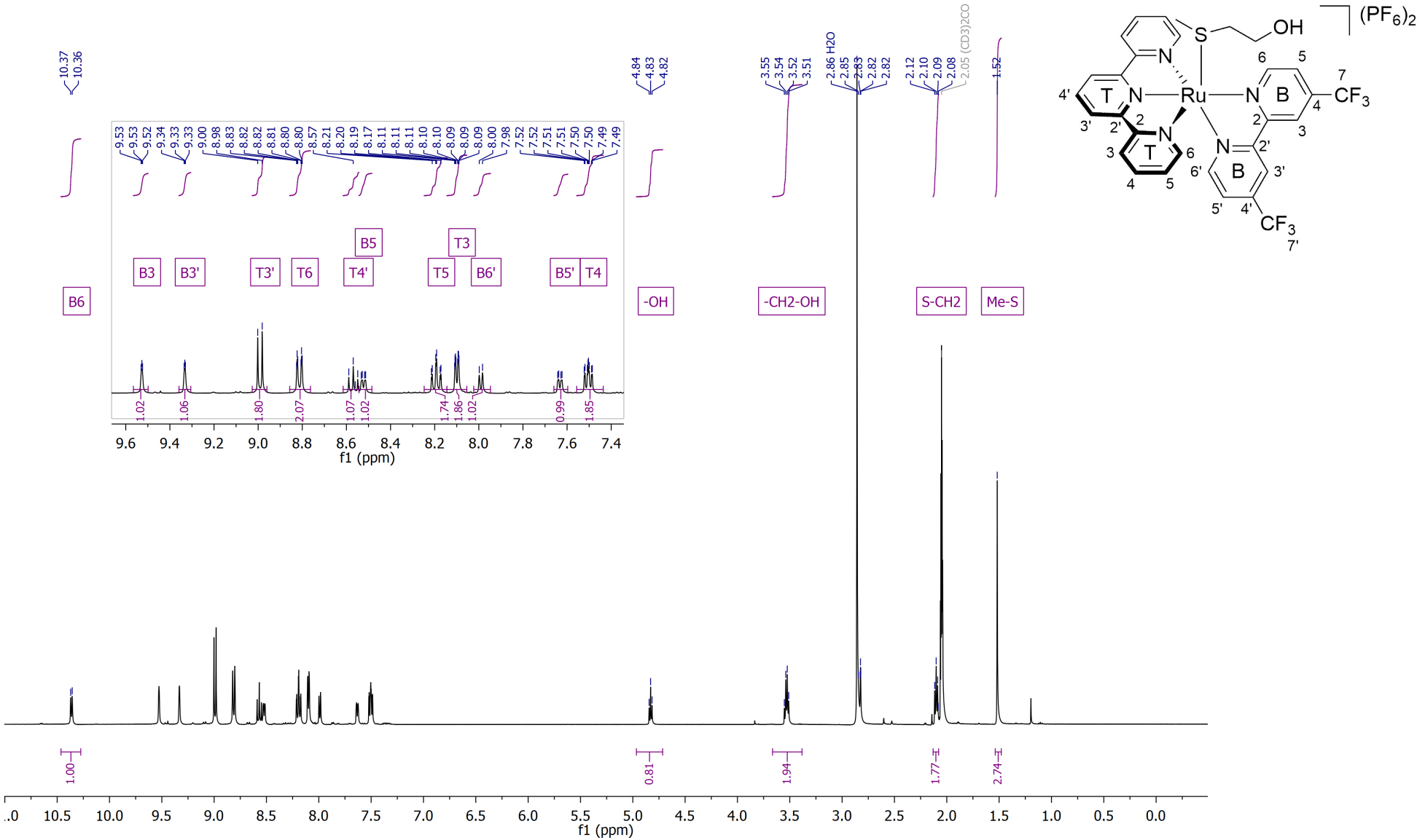

Figure S17. ^{1}H NMR (300 MHz, $(CD_3)_2CO$) of [Ru(tpy)(tfmbpy)(Hmte)]$(PF_6)_2$, [**8**]$(PF_6)_2$.

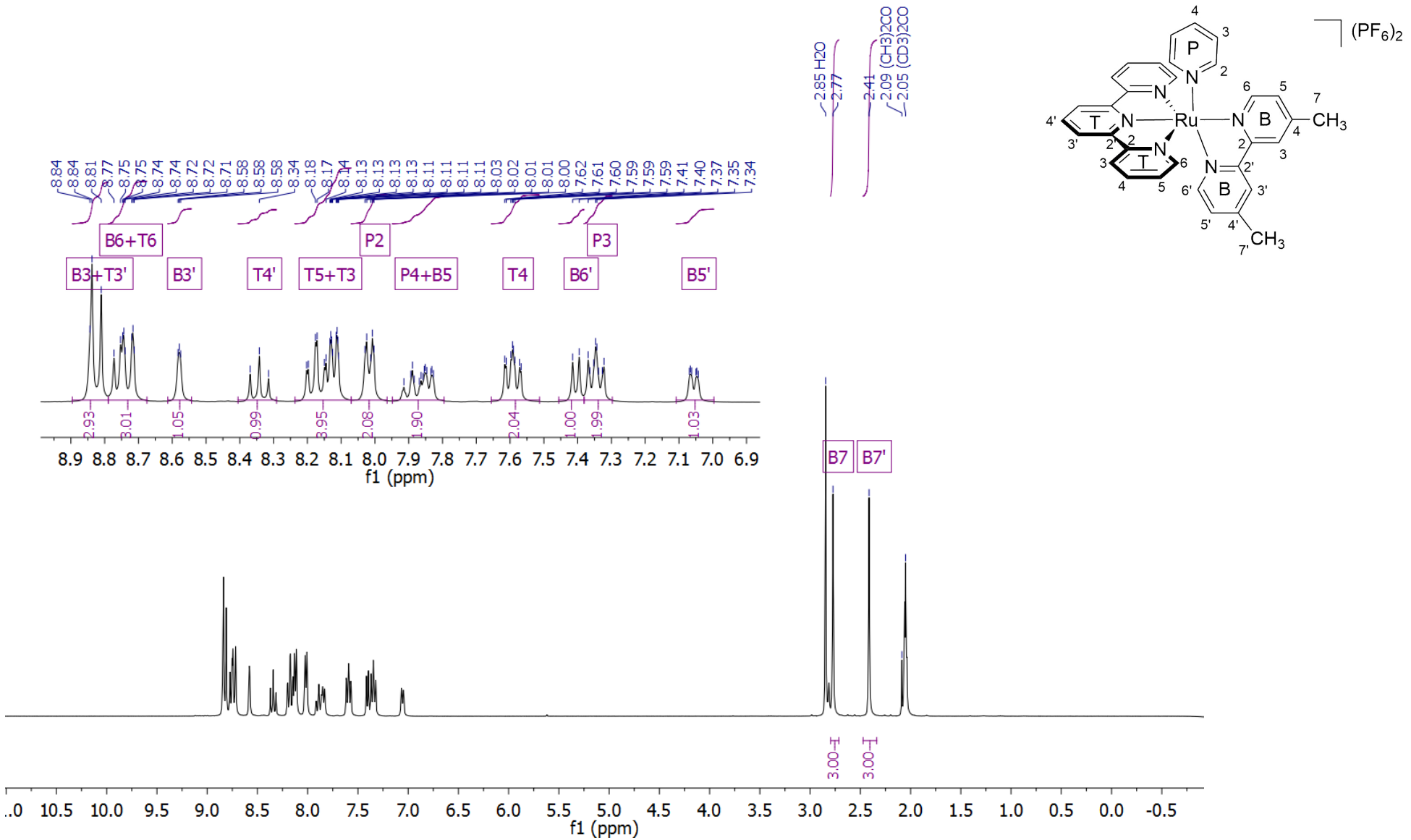

Figure S18. ^{1}H NMR (300 MHz, $(CD_3)_2CO$) of [Ru(tpy)(dmbpy)(py)]$(PF_6)_2$, [**9**]$(PF_6)_2$.

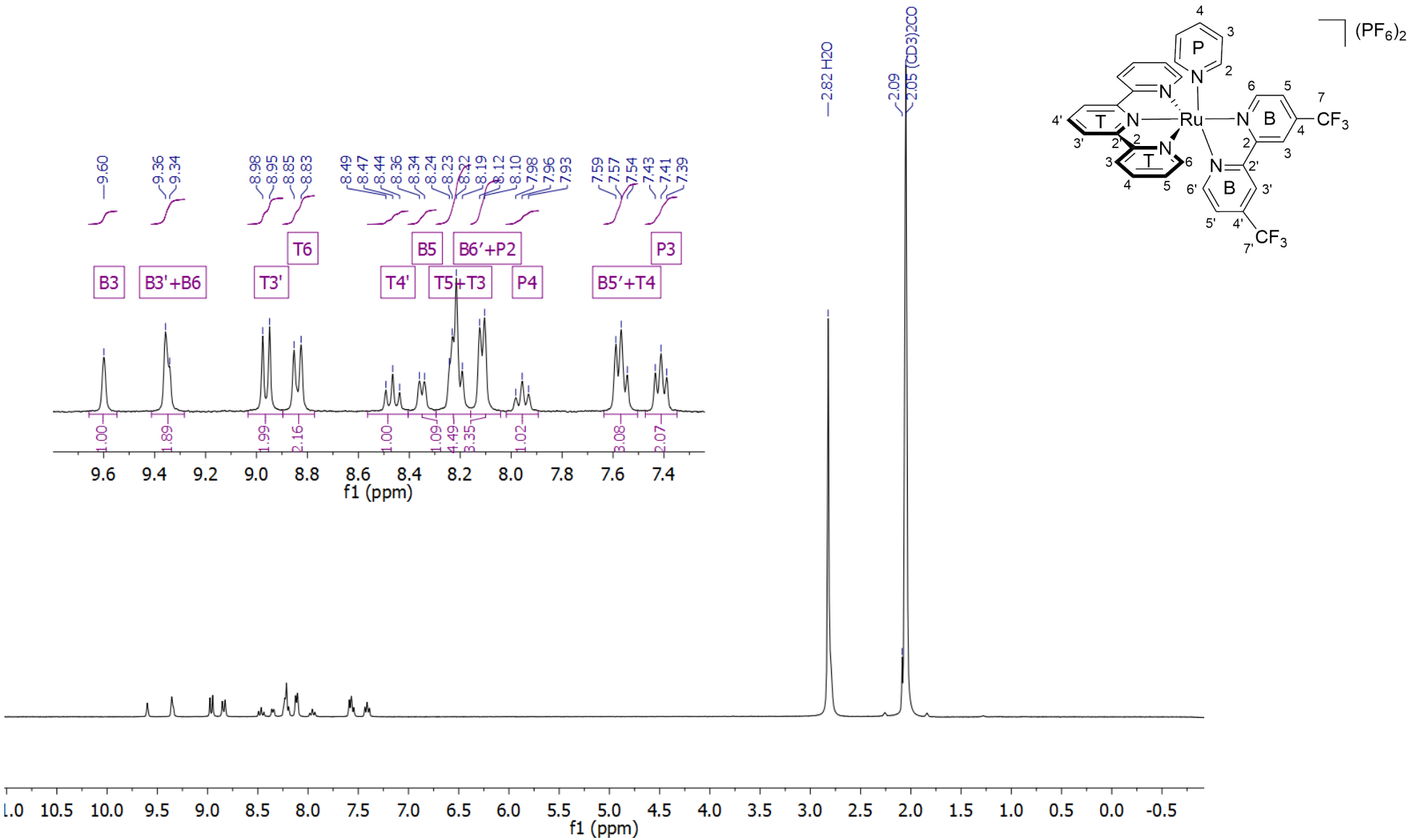

Figure S19. ^{1}H NMR (300 MHz, $(CD_3)_2CO$) of $[Ru(tpy)(tfmbpy)(py)](PF_6)_2$, [**10**]$(PF_6)_2$.

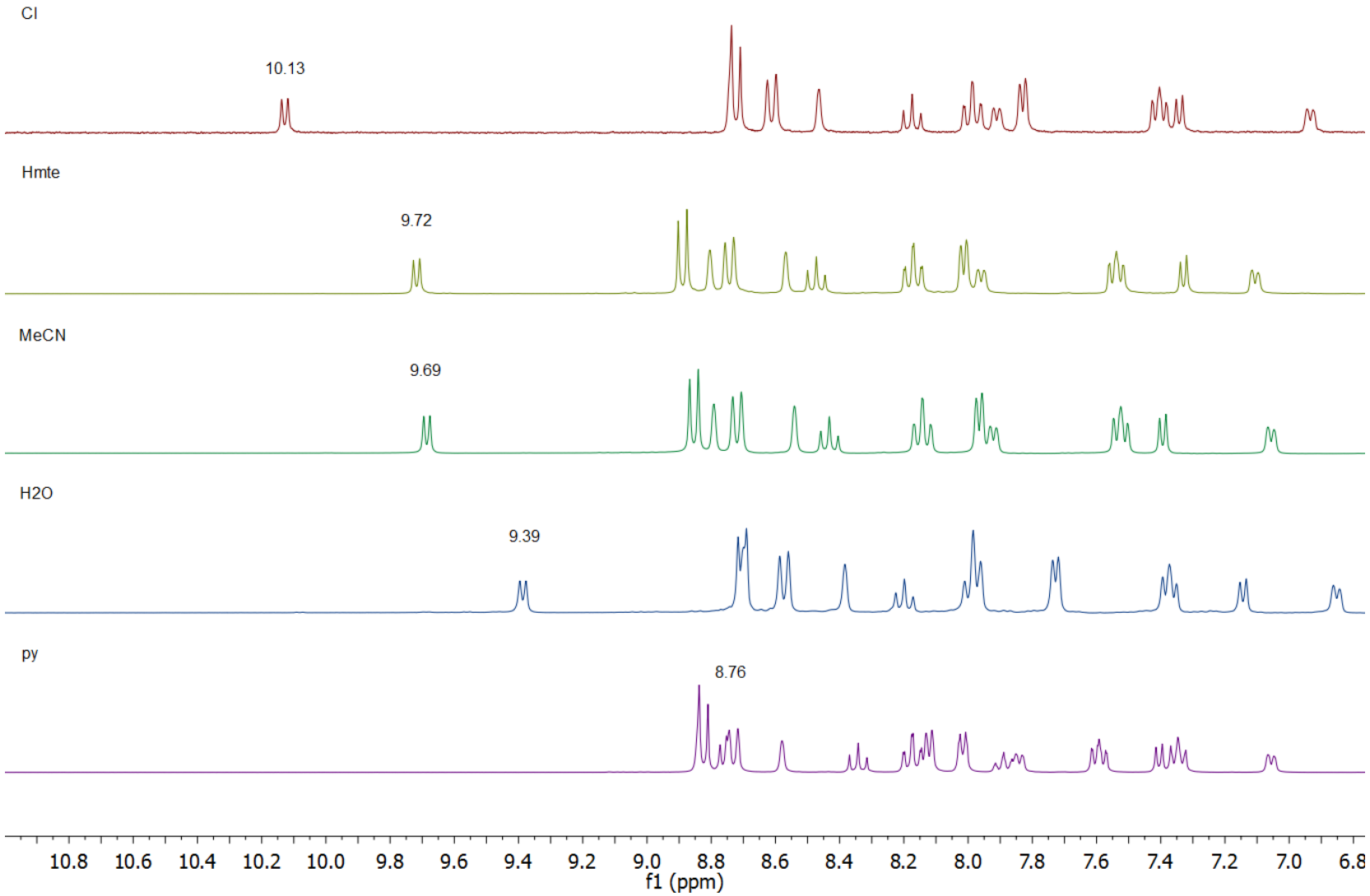

Figure S20. Aromatic region of ^{1}H NMR (300 MHz, $(CD_3)_2CO$) spectra for $[Ru(tpy)(dmbpy)(L)]^{n+}$.

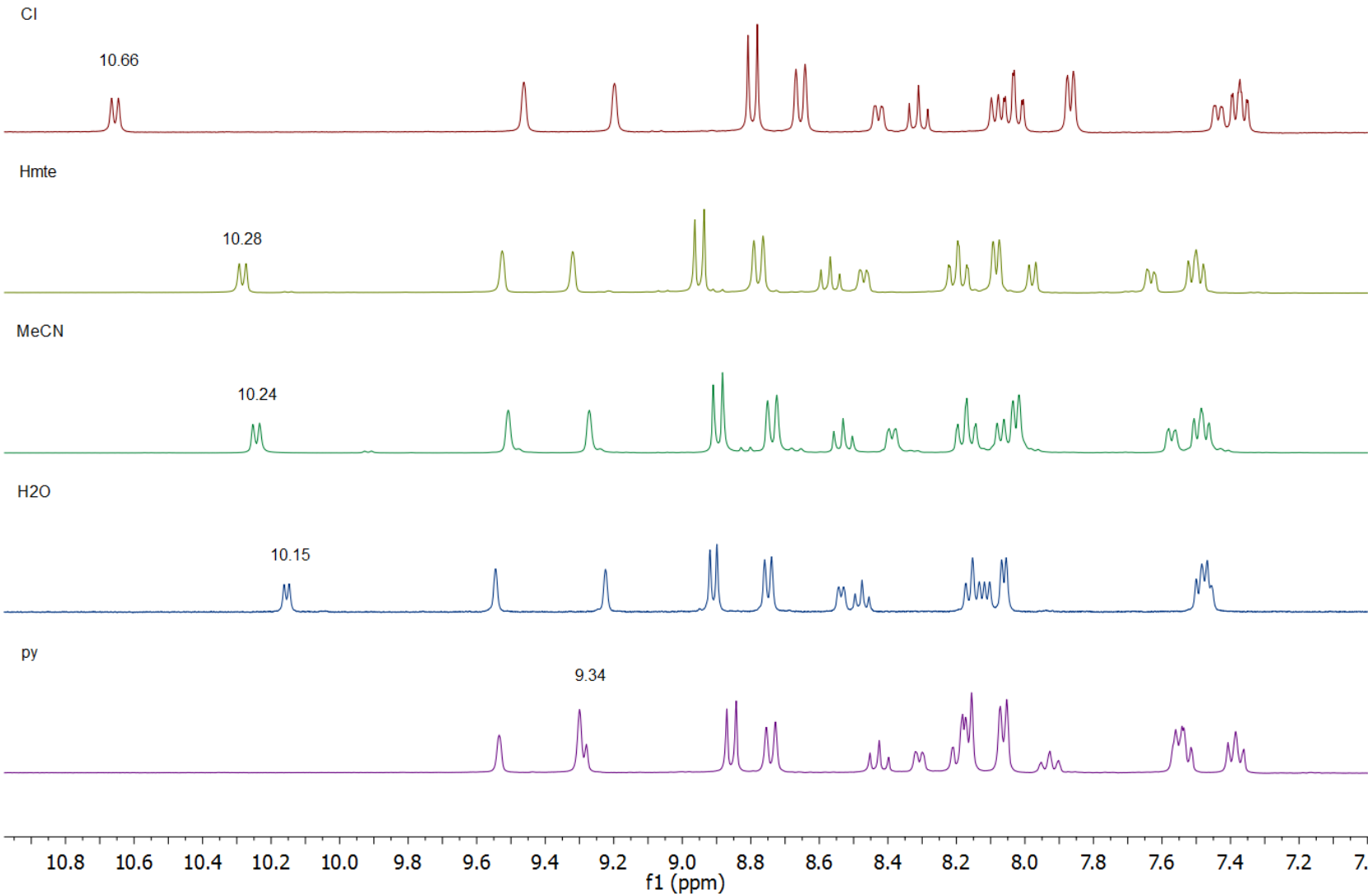

Figure S21. Aromatic region of ^{1}H NMR ($(CD_3)_2CO$) spectra for $[Ru(tpy)(tfmbpy)(L)]^{n+}$.

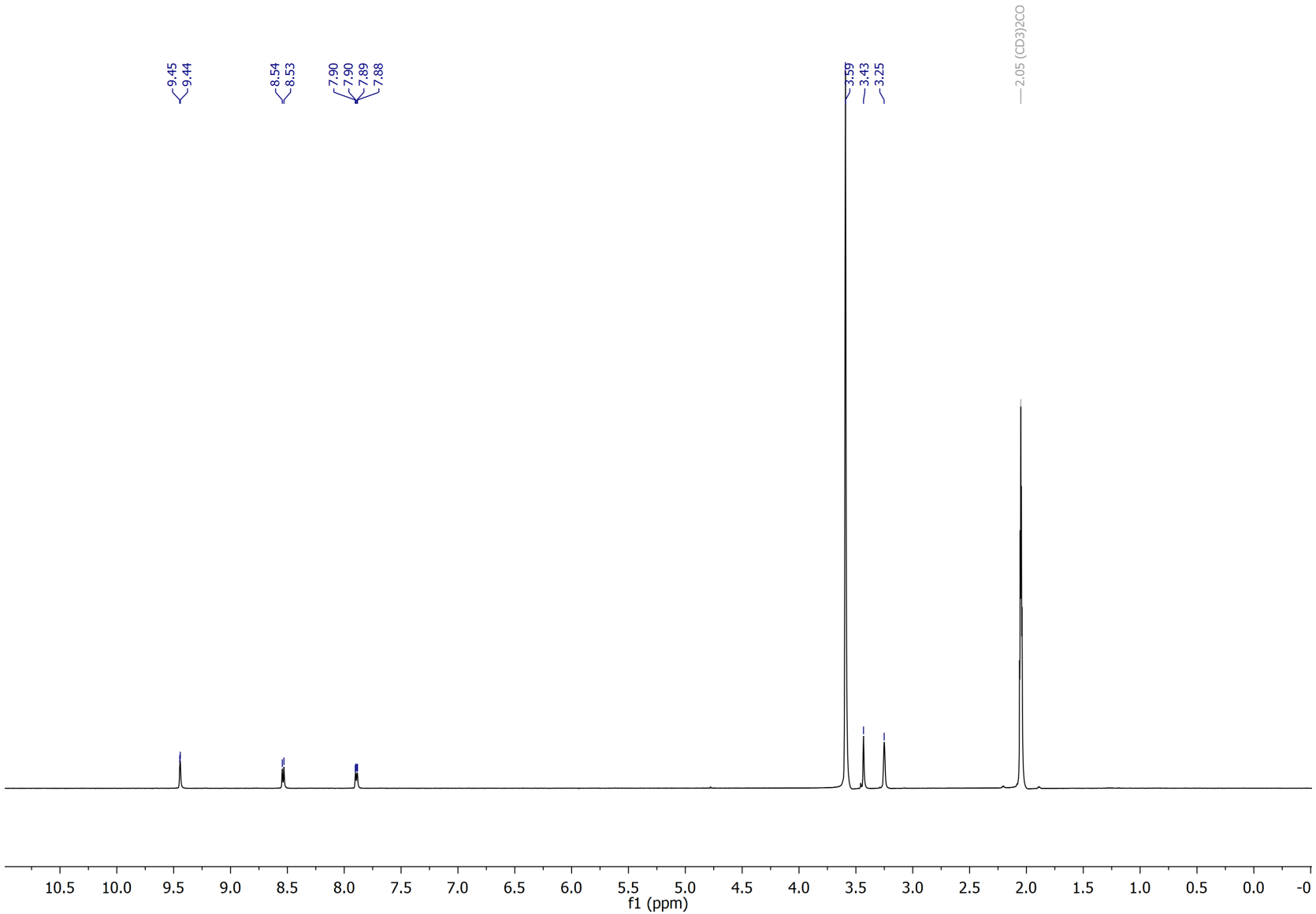

Figure S22. ^{1}H NMR (400 MHz, $(CD_3)_2CO$) of $[Ru(tfmbpy)_3]Cl_2$.

3. ES-MS of the Ru complexes

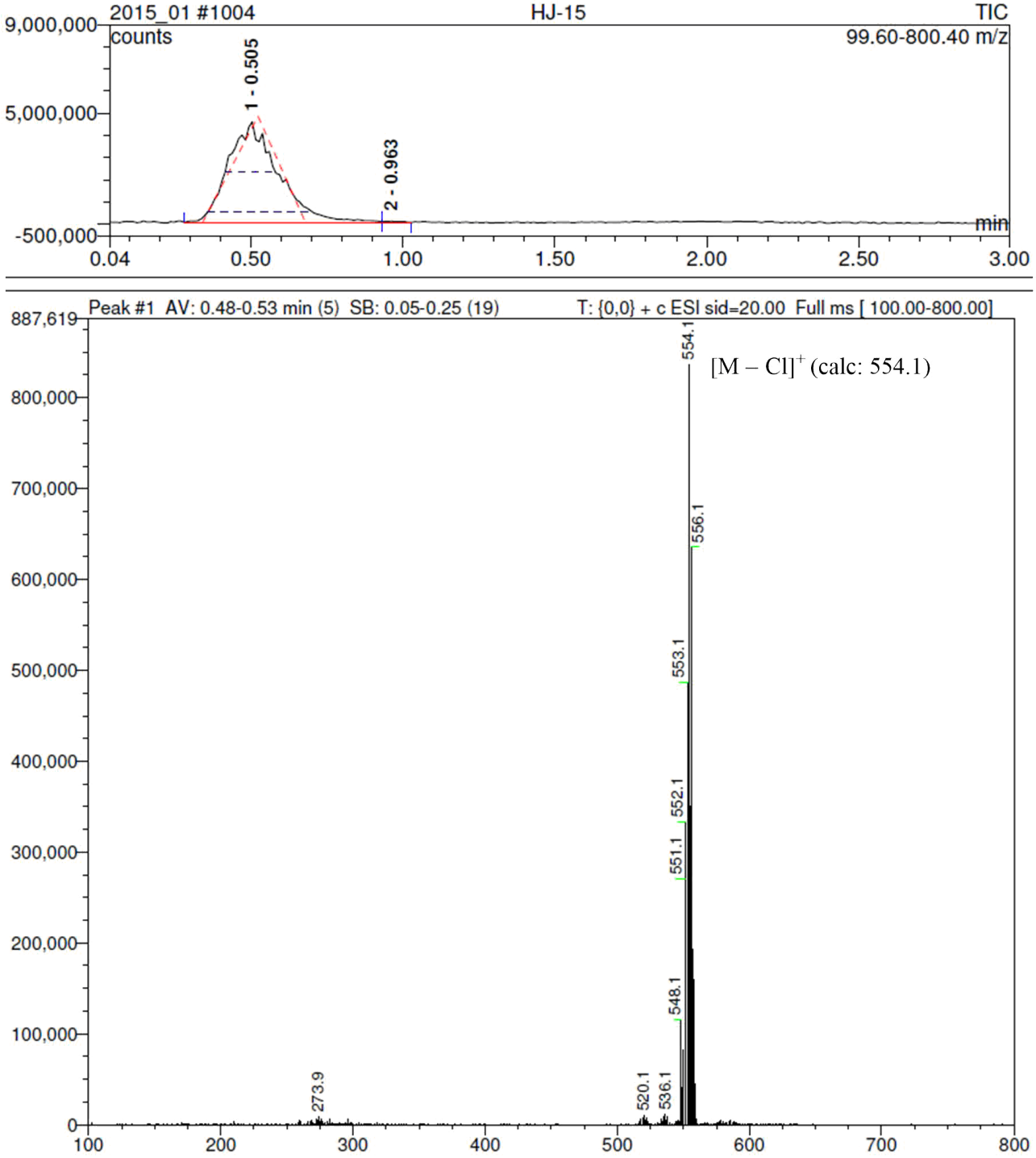

Figure S23. ES-MS of [Ru(tpy)(dmbpy)Cl]Cl, [**1**]Cl.

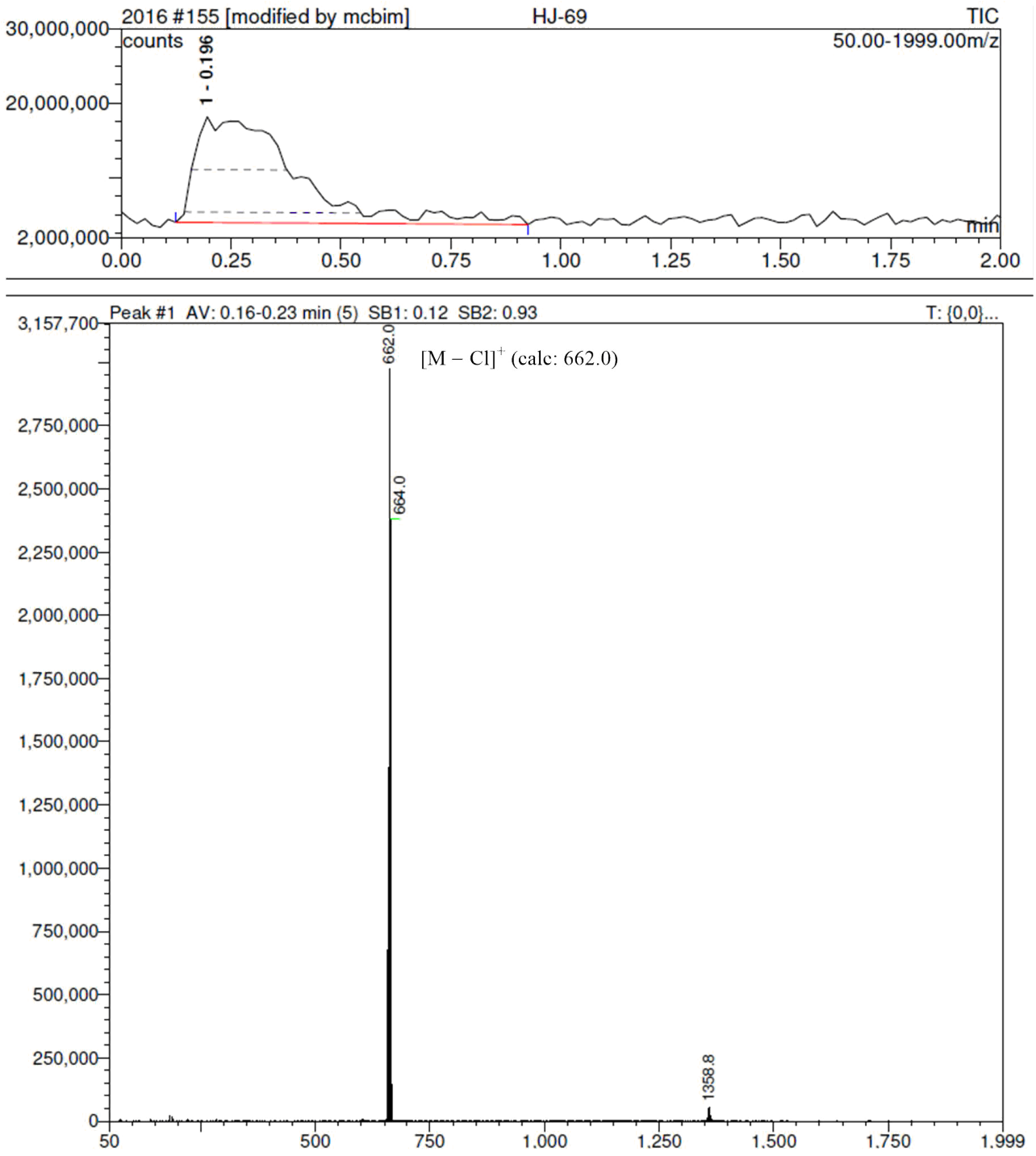

Figure S24. ES-MS of [Ru(tpy)(tfmbpy)Cl]Cl, [**2**]Cl.

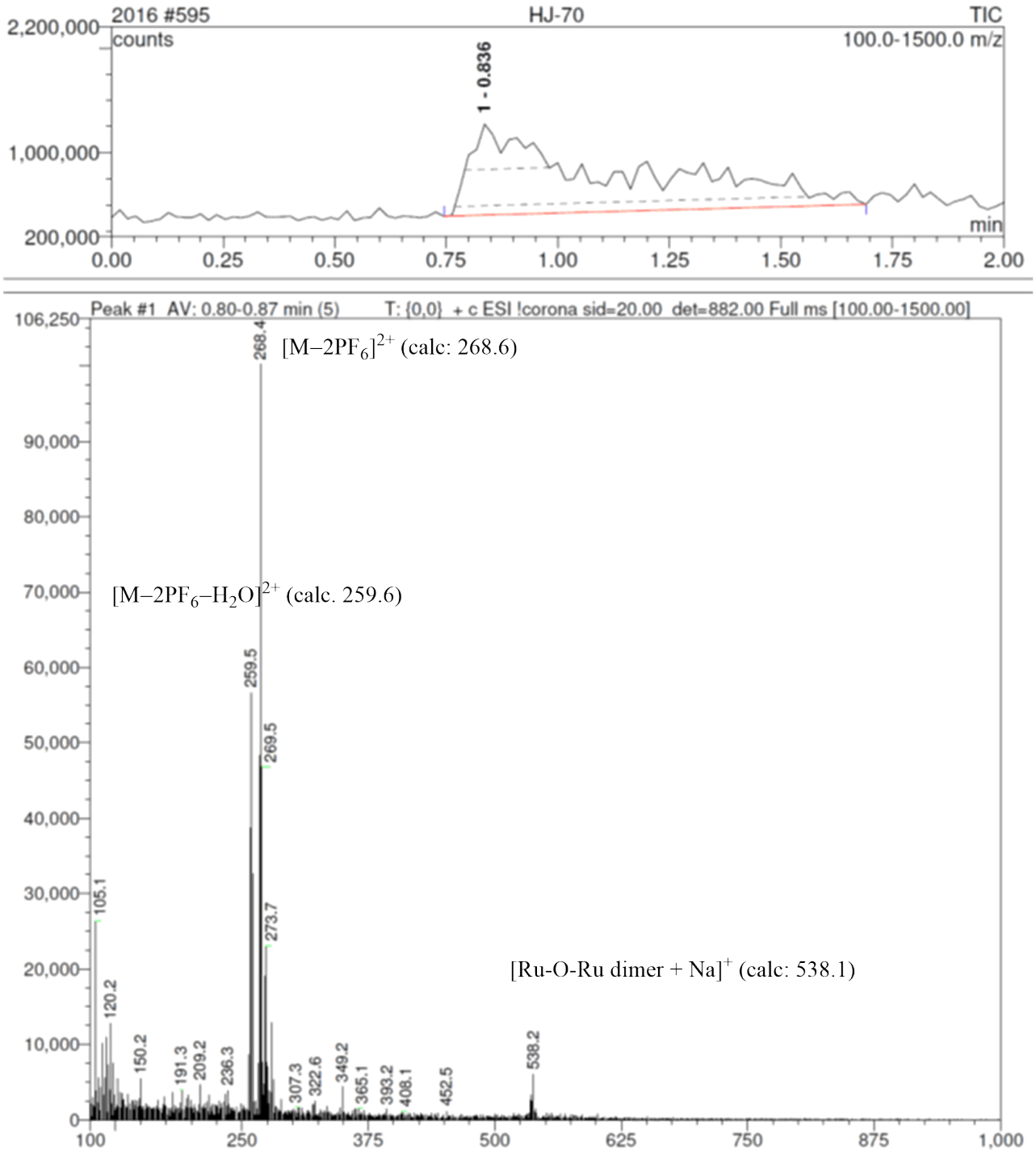

Figure S25. ES-MS of $[Ru(tpy)(dmbpy)(OH_2)](PF_6)_2$, $[\mathbf{3}](PF_6)_2$.

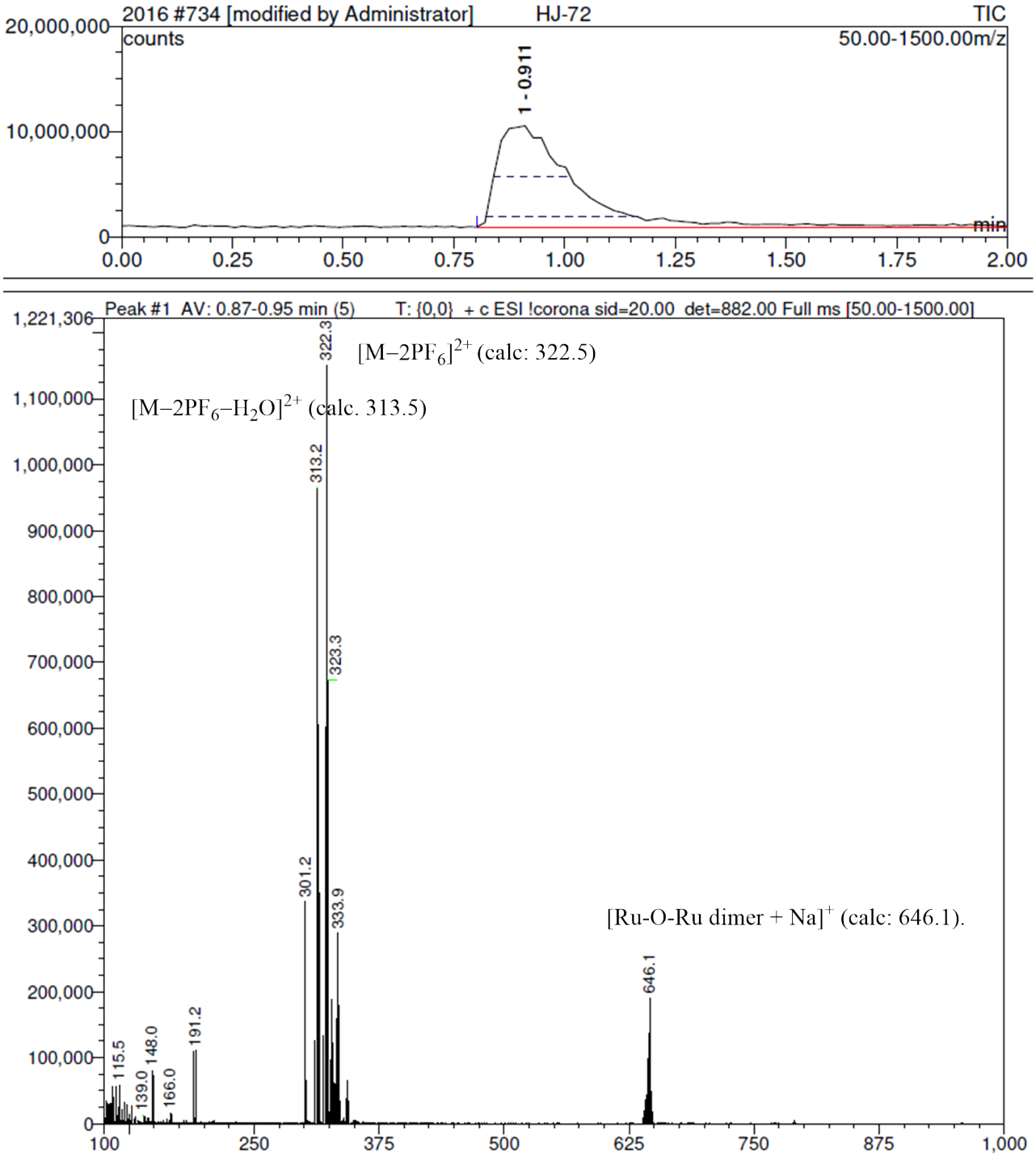

Figure S26. ES-MS of [Ru(tpy)(tfmbpy)(OH_2)](PF_6)$_2$, [**4**](PF_6)$_2$.

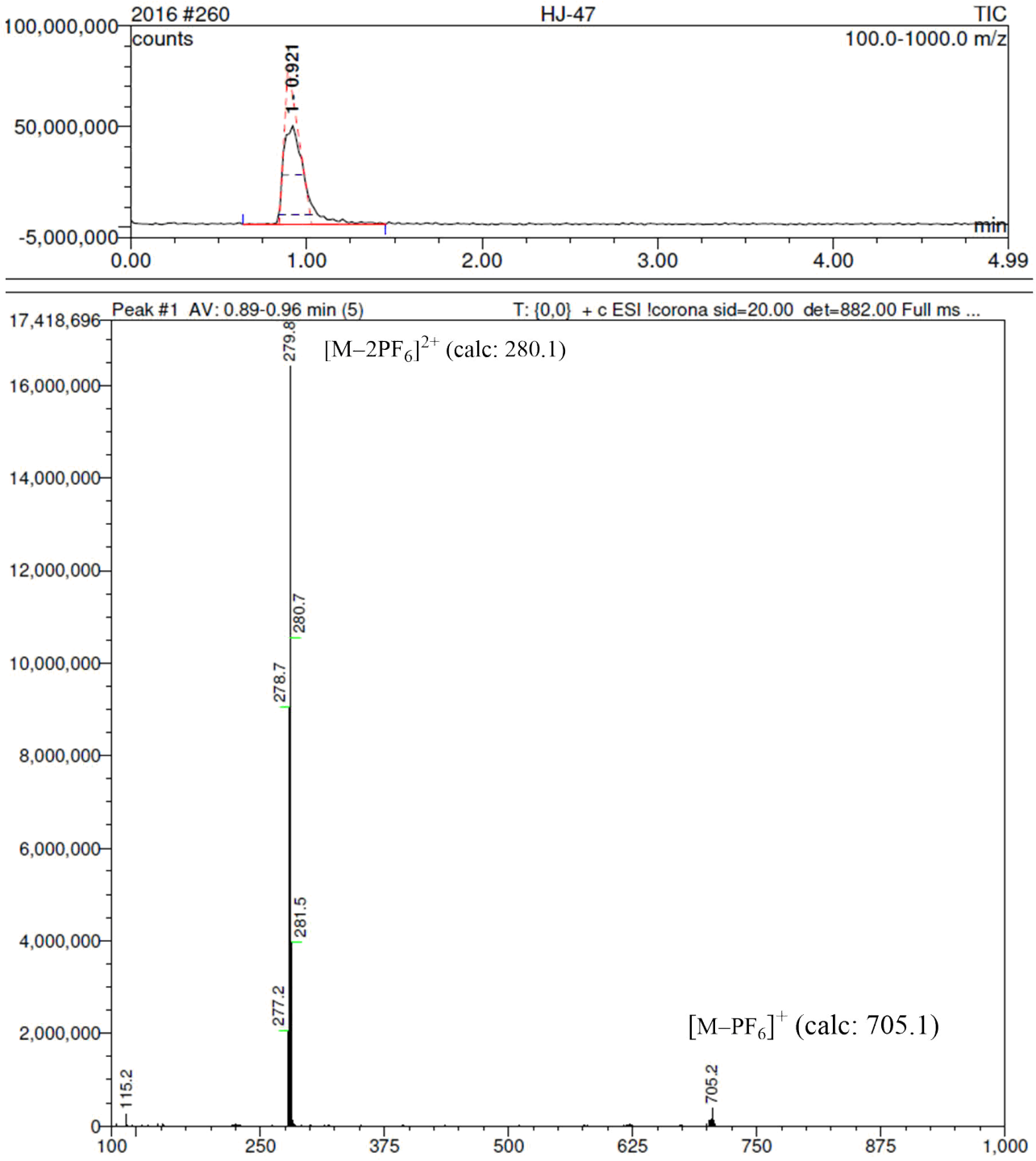

Figure S27. ES-MS of [Ru(tpy)(dmbpy)($NCCH_3$)](PF_6)$_2$, [**5**](PF_6)$_2$.

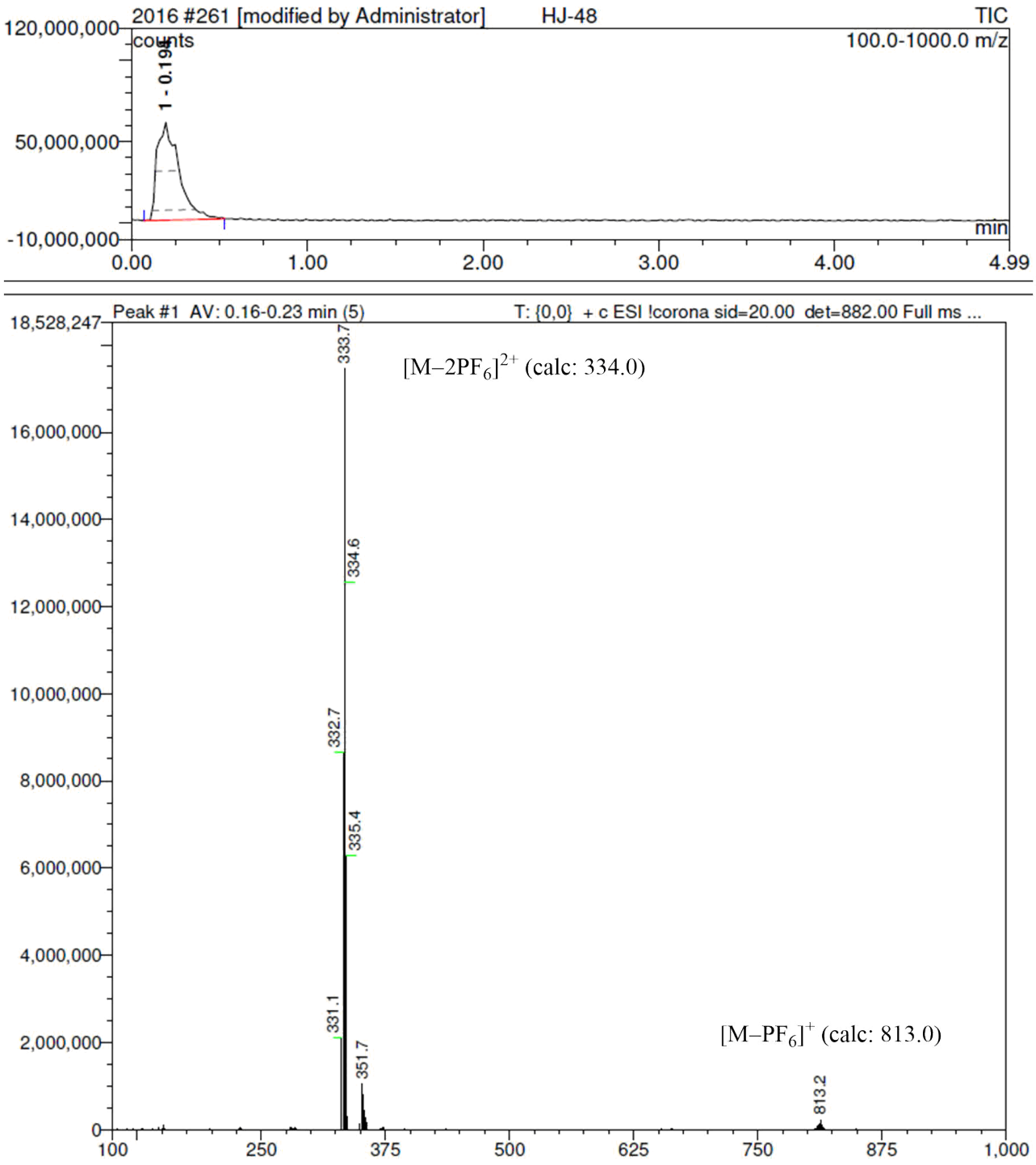

Figure S28. ES-MS of [Ru(tpy)(tfmbpy)(NCCH$_3$)](PF$_6$)$_2$, [**6**](PF$_6$)$_2$.

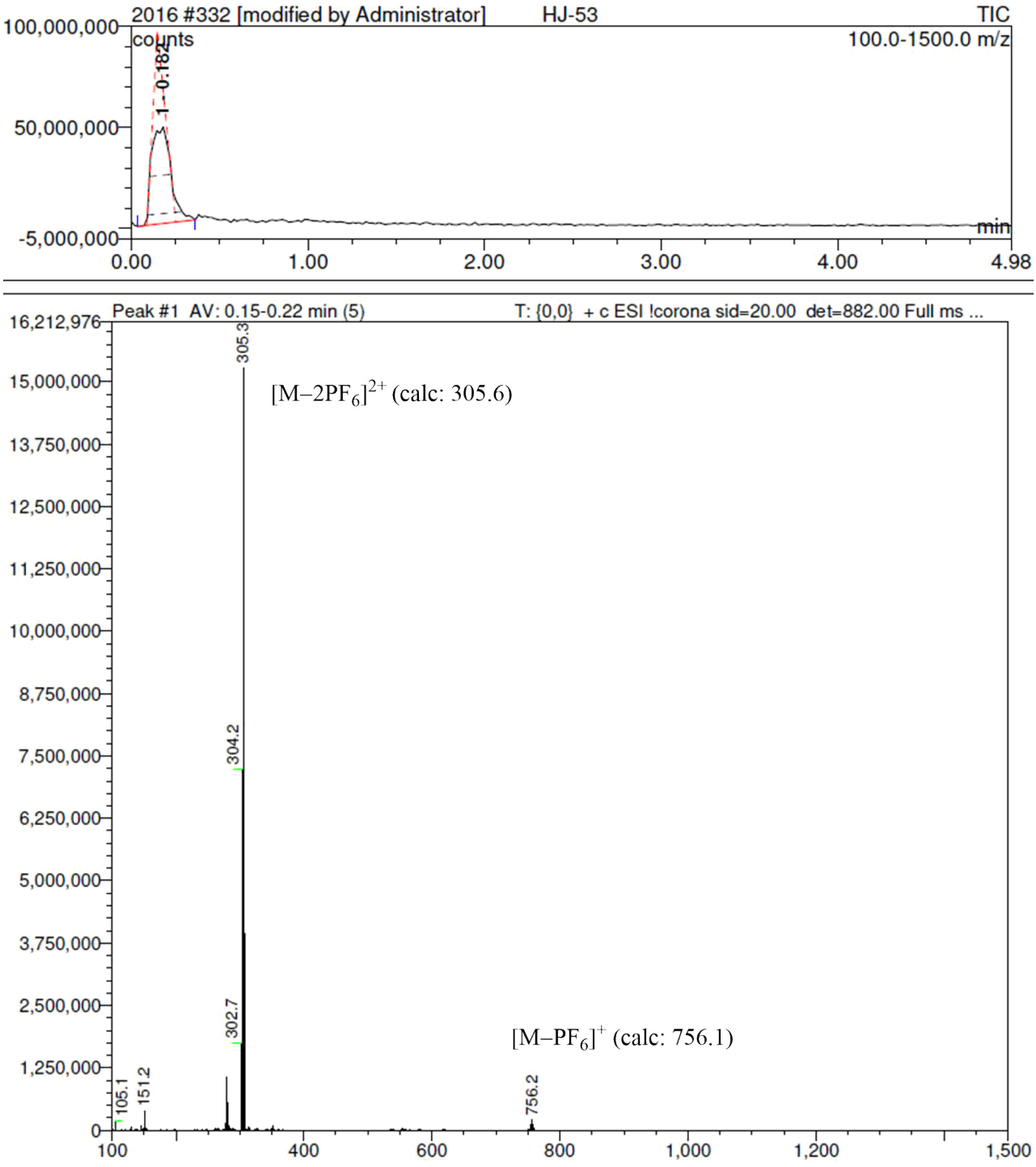

Figure S29. ES-MS of [Ru(tpy)(dmbpy)(Hmte)]$(PF_6)_2$, [**7**]$(PF_6)_2$.

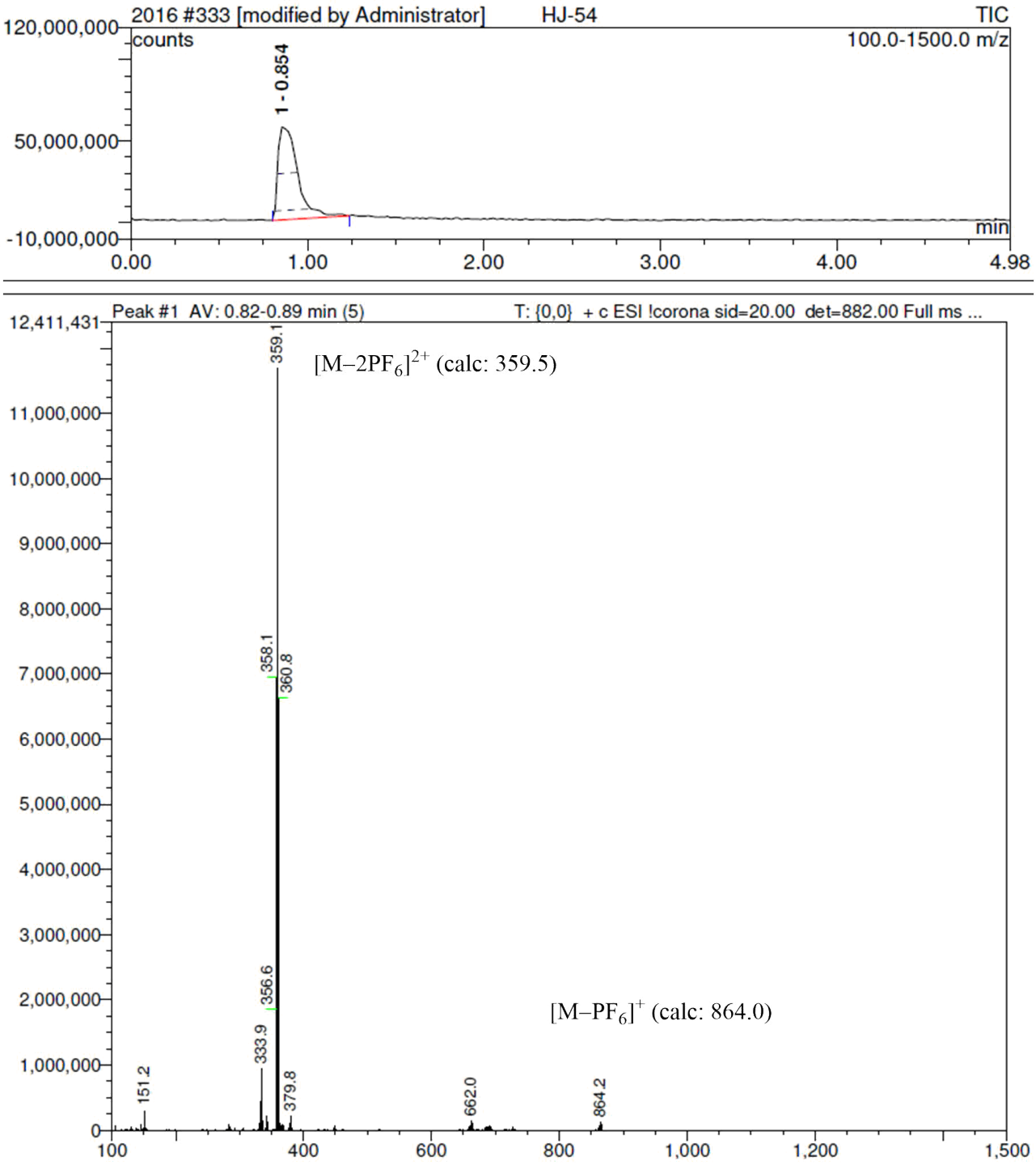

Figure S30. ES-MS of [Ru(tpy)(tfmbpy)(Hmte)]$(PF_6)_2$, [**8**]$(PF_6)_2$.

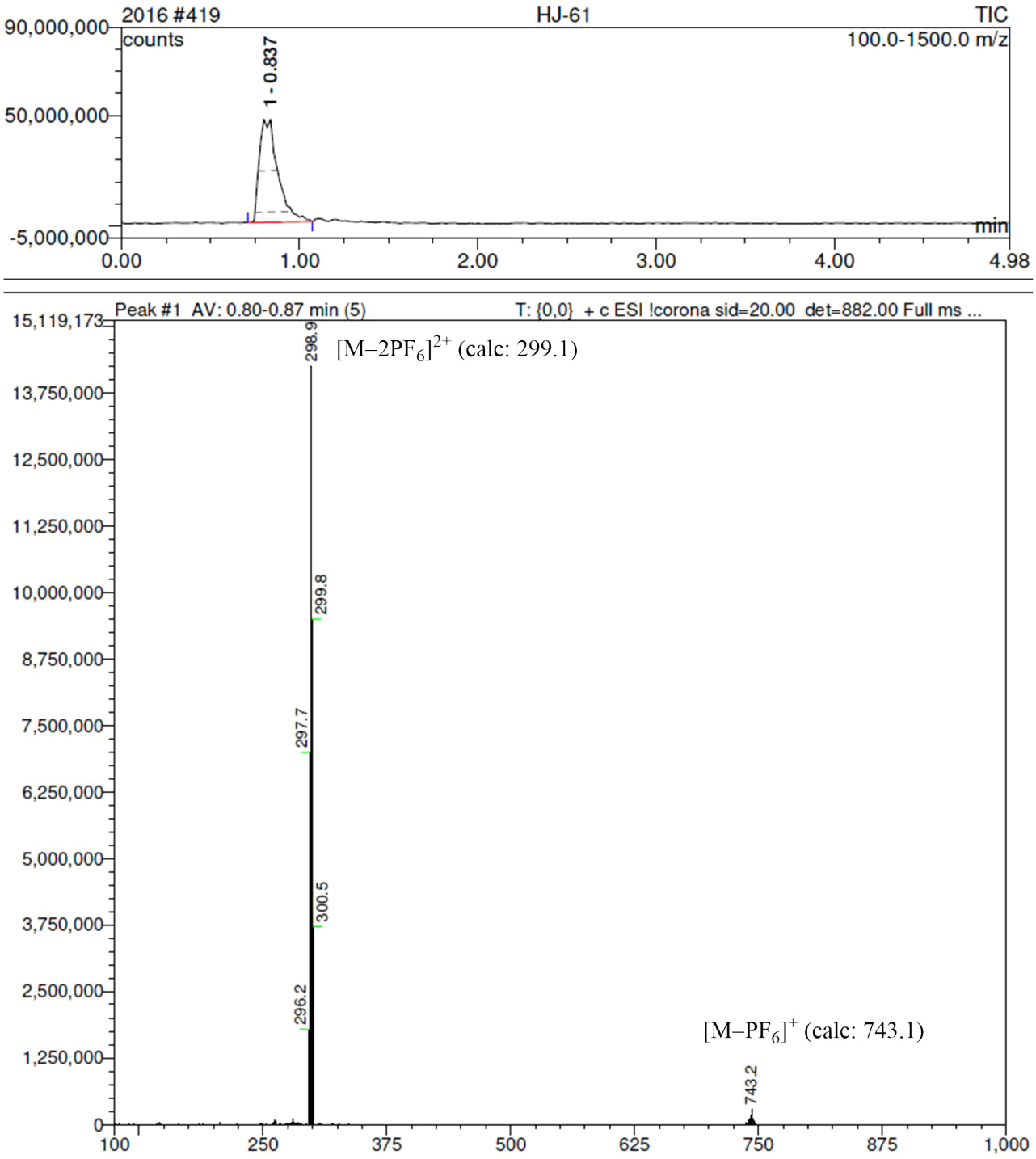

Figure S31. ES-MS of [Ru(tpy)(dmbpy)(py)]$(PF_6)_2$, [**9**]$(PF_6)_2$.

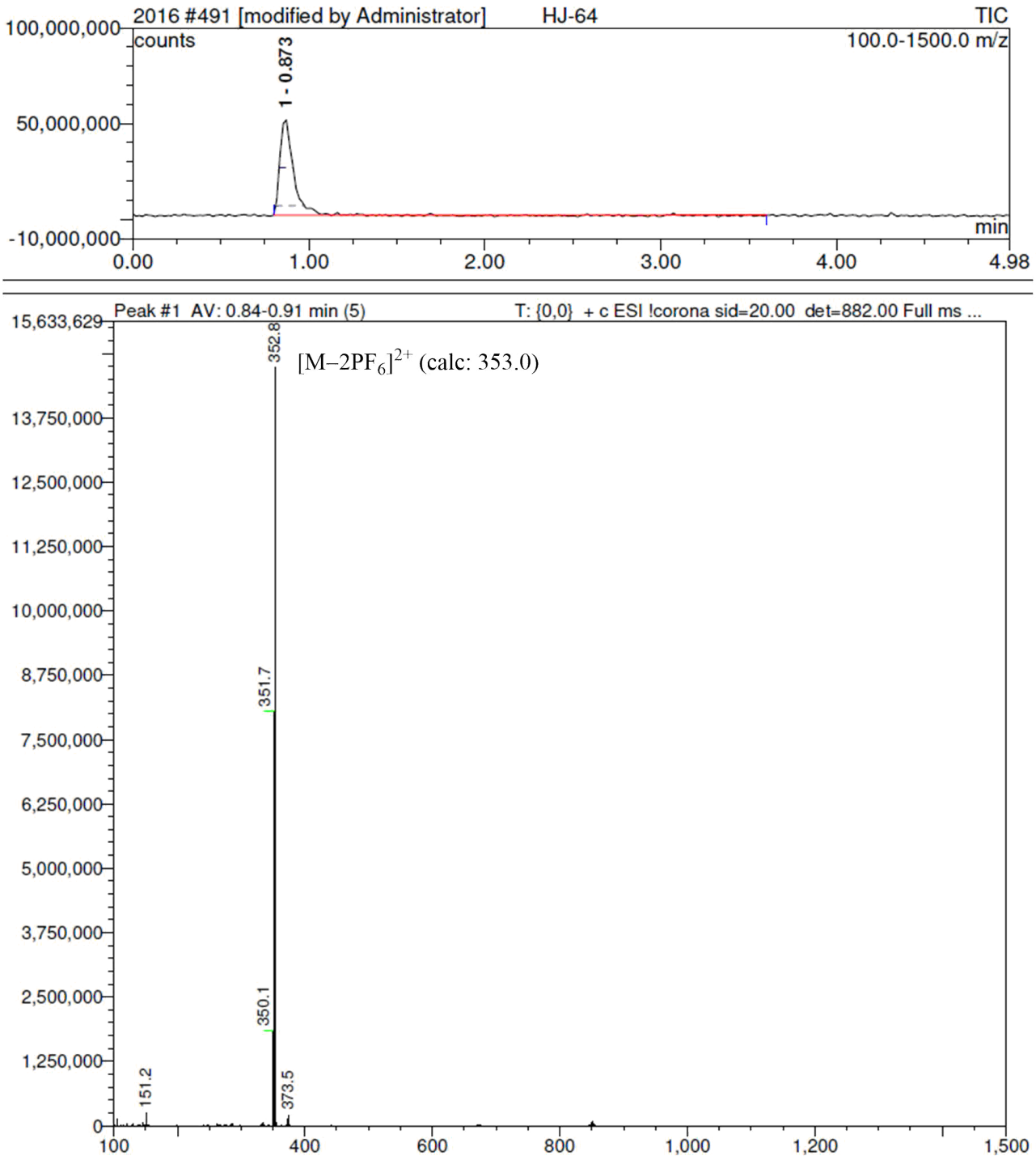

Figure S32. ES-MS of [Ru(tpy)(tfmbpy)(py)]$(PF_6)_2$, [**10**]$(PF_6)_2$.

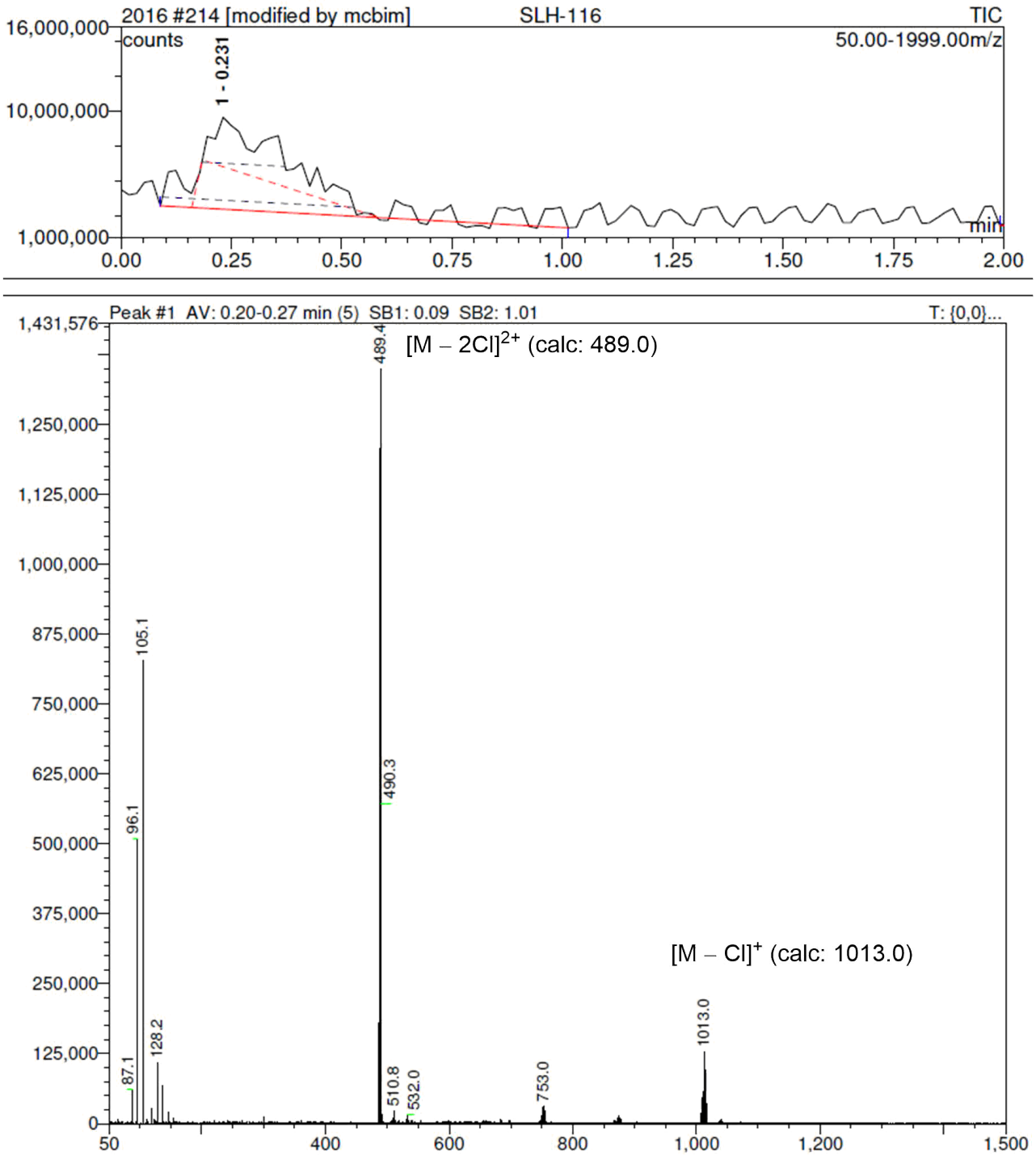

Figure S33. ES-MS of $[Ru(tfmbpy)_3]Cl_2$.

4. Single Crystal X-ray Crystallography.

Table S1. Crystal data and structure refinement for [**1**]Cl, [**2**](PF_6), [**5**](PF_6)$_2$, [**6**](PF_6)$_2$, [**7**](PF_6)$_2$, [**8**](PF_6)$_2$, [**9**](PF_6)$_2$, and [**10**](PF_6)$_2$.

	[**1**]Cl	[**2**](PF_6)	[**5**](PF_6)$_2$	[**6**](PF_6)$_2$	[**7**](PF_6)$_2$	[**8**](PF_6)$_2$	[**9**](PF_6)$_2$	[**10**](PF_6)$_2$
Crystal data								
Chemical formula	$C_{27}H_{23}ClN_5Ru$ ·C_2H_6O·Cl	$C_{27}H_{17}ClF_6N_5Ru$ ·F_6P·C_3H_6O	$C_{29}H_{26}N_6Ru$·2(F_6P) ·0.703(C_2H_3N)	$C_{29}H_{20}F_6N_6Ru$· 2(F_6P)·C_2H_3N	$C_{30}H_{31}N_5ORuS$ ·2(F_6P)·C_3H_6O	$C_{30}H_{24}F_6N_5ORuS$· 2(F_6P)	$C_{32}H_{28}N_6Ru$· 2(F_6P)·C_7H_8	$C_{32}H_{22}F_6N_6Ru$· 2(F_6P)·C_3H_6O
M_r	635.54	865.02	878.43	998.57	958.74	1007.61	979.75	1053.64
Crystal system, space group	Monoclinic, $P2_1/c$	Monoclinic, $P2_1/n$	Triclinic, *P*-1	Monoclinic, $P2_1/n$	Monoclinic, $P2_1/c$	Trigonal, *R*-3:*H*	Monoclinic, $P2_1/c$	Monoclinic, $P2_1/c$
Temperature (K)	110	110	110	110	110	110	110	110
a (Å)	12.1750 (5)	8.7205 (2)	10.6593 (4)	8.6380 (5)	9.04902 (11)	34.6961 (6)	15.5230 (4)	18.0695 (2)
b (Å)	14.2168 (5)	24.1351 (6)	12.9990 (5)	21.5817 (10)	11.28288 (14)	34.6961 (6)	19.4563 (5)	19.9997 (2)
c (Å)	15.7813 (7)	18.4535 (3)	13.7679 (6)	19.0970 (8)	36.8264 (5)	16.7145 (3)	13.0240 (3)	12.79332 (14)
α (°)	90	90	83.443 (3)	90	90	90	90	90
β (°)	95.737 (4)	101.672 (2)	73.885 (3)	96.896 (4)	90.8063 (11)	90	91.028 (2)	106.8441 (12)
γ (°)	90	90	69.727 (3)	90	90	120	90	90
V (Å^3)	2717.90 (19)	3803.60 (15)	1718.85 (13)	3534.4 (3)	3759.57 (8)	17425.5 (7)	3932.88 (17)	4424.95 (9)
Z	4	4	2	4	4	18	4	4
Radiation type	Cu *K*α	Cu *K*α	Cu *K*α	Cu *K*α	Cu *K*α	Cu *K*α	Mo *K*α	Cu *K*α
μ (mm^{-1})	6.74	5.20	5.49	5.69	5.60	5.69	0.58	4.59
Crystal size (mm)	0.63 × 0.48 × 0.05	0.44 × 0.05 × 0.02	0.26 × 0.14 × 0.03	0.42 × 0.07 × 0.03	0.16 × 0.08 × 0.05	0.30 × 0.13 × 0.06	0.39 × 0.11 × 0.08	0.41 × 0.21 × 0.03
Data collection								
Diffractometer	SuperNova, Dual, Cu at zero, Atlas							
T_{min}, T_{max}	0.102, 0.746	0.369, 0.901	0.447, 0.893	0.332, 0.862	0.558, 0.814	0.386, 0.754	0.684, 1.000	0.420, 0.892

No. of measured, independent and observed [$I > 2\sigma(I)$] reflections	15180, 5956, 5156	42386, 7464, 6016	22328, 6711, 6177	37035, 10903, 8212	25028, 7371, 6510	35681, 7552, 6301	30368, 9036, 7378	28892, 8673, 7432
R_{int}	0.037	0.078	0.038	0.046	0.030	0.041	0.038	0.045
$(\sin \theta/\lambda)_{max}$ (Å^{-1})	0.616	0.616	0.617	0.616	0.616	0.616	0.650	0.616
Refinement								
$R[F^2 > 2\sigma(F^2)]$, $wR(F^2)$, S	0.046, 0.125, 0.98	0.042, 0.113, 1.02	0.032, 0.084, 1.01	0.059, 0.160, 0.99	0.033, 0.085, 1.03	0.048, 0.138, 1.02	0.038, 0.094, 1.03	0.046, 0.132, 1.03
No. of reflections	5956	7464	6711	10903	7371	7552	9036	8673
No. of parameters	348	658	799	599	737	715	655	830
No. of restraints		706	1456	249	980	812	505	1150
H-atom treatment	H-atom parameters constrained							
$\Delta\rho_{max}$, $\Delta\rho_{min}$ (e Å^{-3})	1.29, -0.93	0.83, -0.73	0.80, -0.55	1.35, -1.87	0.61, -0.56	1.11, -0.82	0.59, -0.72	1.13, -0.61

Computer programs: *CrysAlis PRO*, Agilent Technologies, Version 1.171.37.35 (release 13-08-2014 CrysAlis171 .NET) (compiled Aug 13 2014, 18:06:01), *SHELXS2014*/7 (Sheldrick, 2015), *SHELXL2014*/7 (Sheldrick, 2015), *SHELXTL* v6.10 (Sheldrick, 2008).

References:

Sheldrick, G. M. (2015). Acta Cryst. C71, 3-8.

Spek, A.L. (2015). Acta Cryst. C71, 9-18.

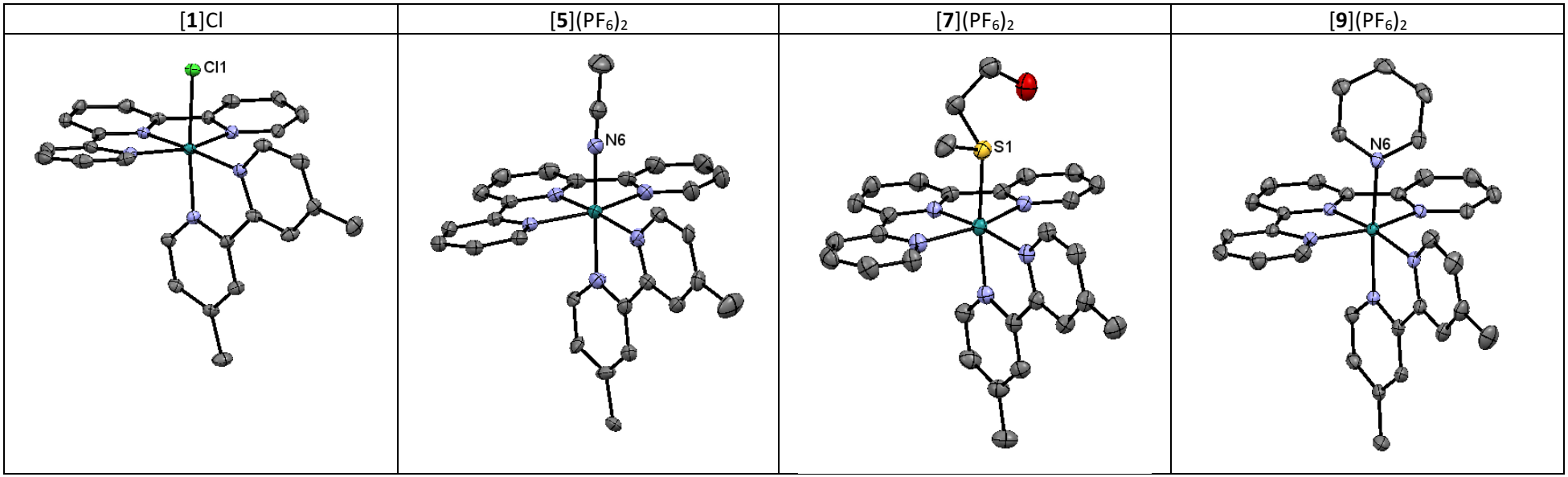

Figure S34. Displacement ellipsoid plots (50% probability level) of [**1**]Cl, [**5**]$(PF_6)_2$, [**7**]$(PF_6)_2$ and [**9**]$(PF_6)_2$. The counter-anions, disorder, hydrogen atoms, and solvents were omitted for clarity. See Figure 2 for other selected atom labels.

Experimental

All reflection intensities were measured at 110(2) K using a SuperNova diffractometer (equipped with Atlas detector) with Mo (λ = 0.71073 Å, only for [**9**](PF$_6$)$_2$) or Cu *K*α radiation (λ = 1.54178 Å) under the program CrysAlisPro (Versions 1.171.36.32 or 1.171.37.35 or 1.171.38.43, Agilent Technologies, 2013-2015). The same program was used to refine the cell dimensions and for data reduction. The structure was solved with the program SHELXS-2014/7 (Sheldrick, 2015) and was refined on F^2 with SHELXL-2014/7 (Sheldrick, 2015). Analytical numeric or numerical (Gaussian integration, only for [**9**](PF$_6$)$_2$) absorption correction using a multifaceted crystal model was applied using CrysAlisPro. The temperature of the data collection was controlled using the system Cryojet (manufactured by Oxford Instruments). The H atoms were placed at calculated positions (unless otherwise specified) using the instructions AFIX 23, AFIX 43, AFIX 137 or AFIX 147 with isotropic displacement parameters having values 1.2 or 1.5 *U*eq of the attached C or O atoms.

[1]Cl: The structure is ordered. The asymmetric contains one lattice EtOH solvent molecule. The crystal that was mounted on the diffractometer was twinned. The two twin components are related by a twofold axis along the reciprocal vector -0.0776**a*** + 0.0009**b*** + 0.9970**c***. The BASF scale factor refines to 0.2428(16).

[2](PF$_6$): The structure is partly disordered. The lattice acetone solvent molecule and the PF_6^- counterion are disordered over 2 and 3 orientations. All occupancy factors can be retrieved from the .cif file. The asymmetric unit includes one partially occupied and disordered lattice solvent molecule (most likely diethyl ether). Its contribution has been removed from the final refinement using the Squeeze procedure in Platon (Squeeze, 2015).

[5](PF$_6$)$_2$: The structure is partly disordered. Both counterions and the dmbpy ligand are found disordered over either two or three orientations. The occupancy factors for both major and minor components of the disorder are provided in the cif file.

[6](PF$_6$)$_2$: The structure is partly disordered. One of the two PF_6^- counterions was found to be disordered over two orientations, and the occupancy factor of the major component of the disorder refines to 0.698(15). The crystal that was mounted on the diffractometer was not a single crystal but rather a composite of 2 different fragments related by a rotation of *ca.* 3.6° along the reciprocal axis -0.2323**a*** + 0.2184**b*** + 0.9478**c***. The BASF scale factors refine to 0.5391(16).

[7](PF$_6$)$_2$: The structure is partly disordered. Both counterions and the lattice solvent acetone solvent molecule are found disordered over either two or three orientations. The occupancy factors for both major and minor components of the disorder are provided in the cif file.

[8](PF$_6$)$_2$: The 2-methylthio ethanol ligand, the two trifluoromethyl groups and one of the two PF_6^- counterions are found disordered over two or three orientations. The occupancy factors can be retrieved from the .cif file.
The contribution of one small amount of unresolved electron density (possibly a counterion with a small occupancy factor?)* has been removed from the final refinement using the Squeeze procedure in Platon (Squeeze, 2009)
* The two counterions found in the asymmetric unit were constrained to be fully occupied as the crystal contains a Ru(II) complex.

[9](PF$_6$)$_2$: The structure is partly disordered. One of the two PF_6^- counterions and the lattice toluene solvent molecule are found disordered over two orientations. The occupancy factors for both major and minor components of the disorder are provided in the cif file.

[10](PF$_6$)$_2$: The tfmbpy ligand, one of the two PF_6^- counterions, and one lattice acetone solvent molecule are found disordered over two orientations. The occupancy factors can be retrieved from the .cife file. The trifluoromethyl group C26/F1–F3 is likely to be disordered over more than 2 orientations (as the ellipsoids are rather elongated along one direction).
One lattice toluene solvent molecule is most likely partially occupied and very disordered. Its contribution has been removed from the final refinement using the Squeeze procedure in Platon (Squeeze, 2009)

All structures have been deposited in the Cambridge Crystallographic Data Center under the numbers CCDC 1544943-1544950.

5. Cyclic voltammograms

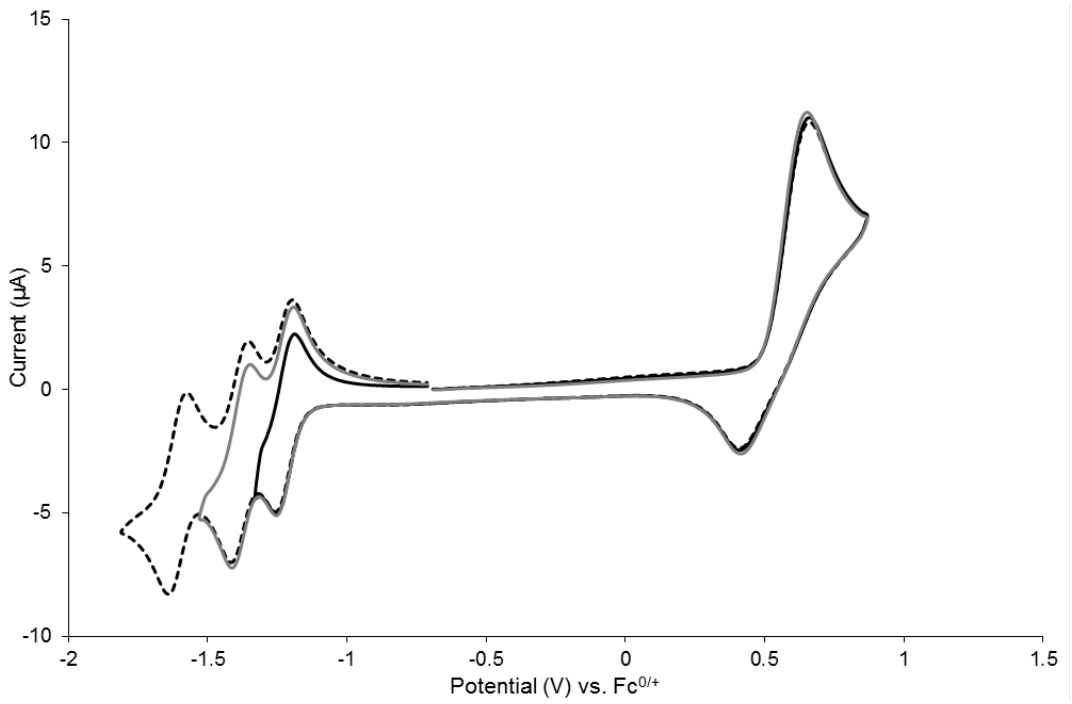

Figure S35. Cyclic voltammogram of 1 mM [Ru(tfmbpy)$_3$]Cl$_2$ complex in 0.1 M Bu$_4$NPF$_6$/CH$_3$CN (ν = 100 mV/s).

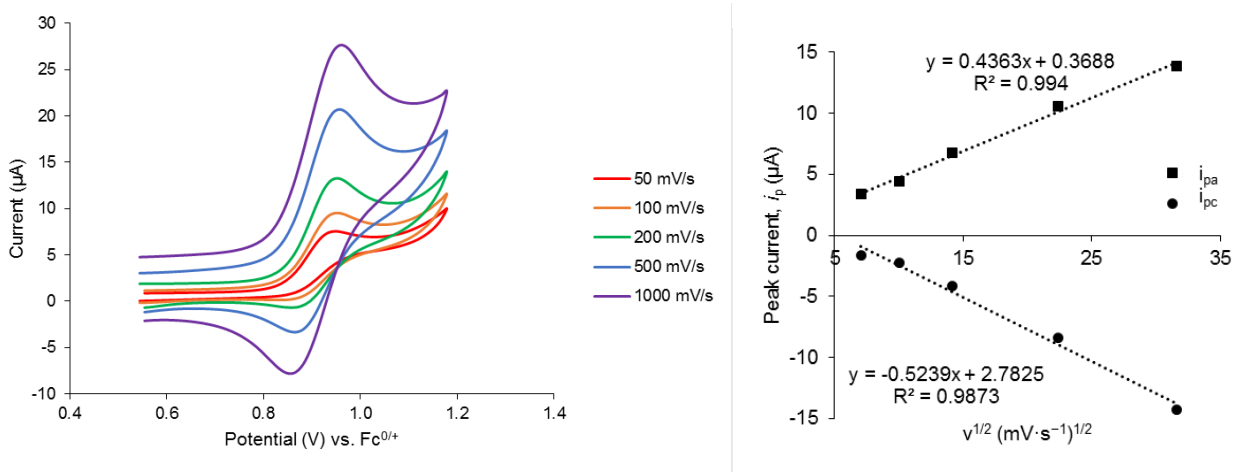

Figure S36. Cyclic voltammogram of $[\mathbf{7}]^{2+}$ around metal-based oxidation with different scan rates. 1 mM of the complex in 0.1 M Bu_4NPF_6/CH_3CN was used (left). Plot of peak current, i_p versus the square root of scan rates (right).

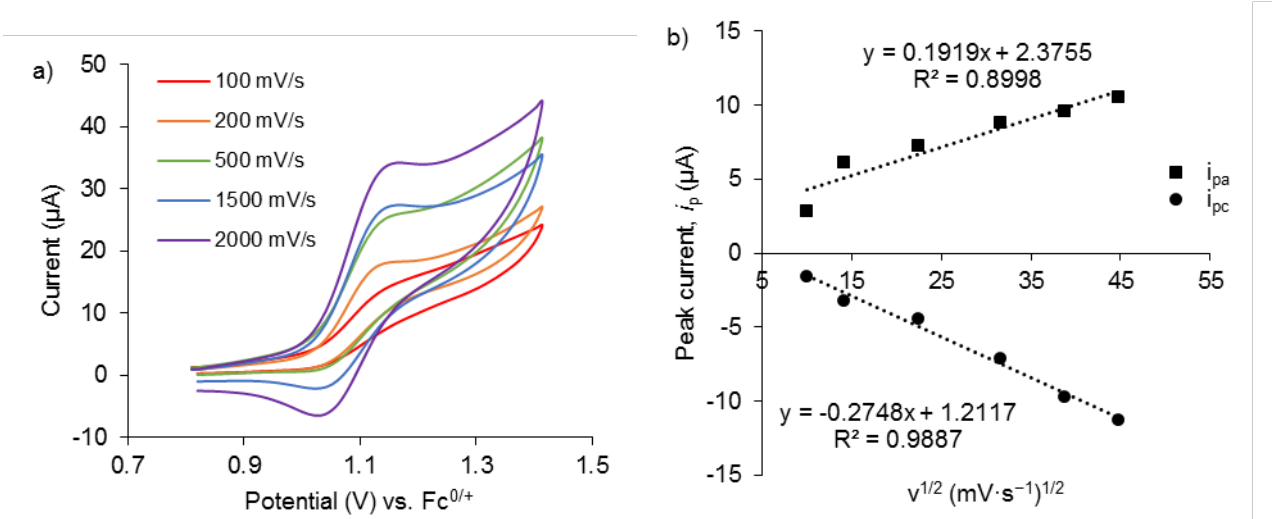

Figure 37. a) Cyclic voltammogram of $[\mathbf{8}]^{2+}$ around Ru-based oxidation potential with different scan rates. b) Plot of peak current, i_p versus the square root of scan rates. 1 mM of the complex in 0.1 M Bu_4NPF_6/CH_3CN was used.

6. UV-vis spectra of $[3]^{2+}$ and $[4]^{2+}$

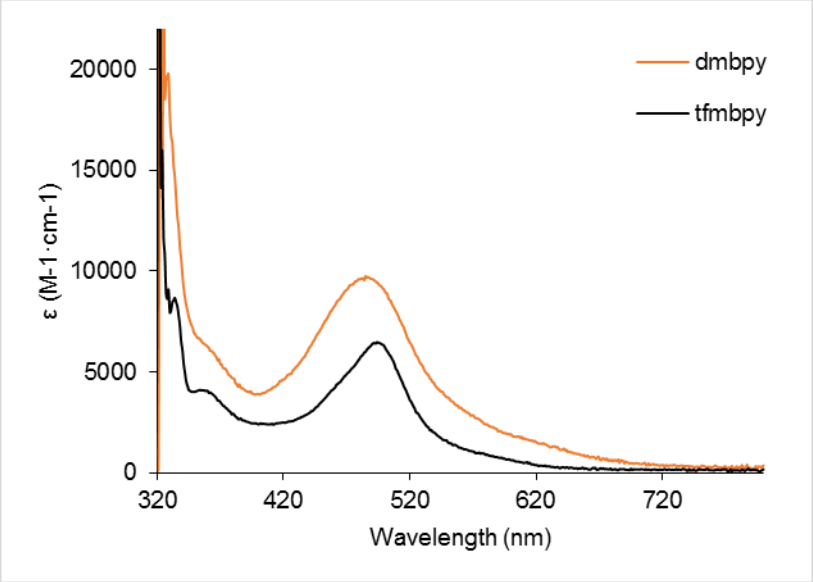

Figure S38. Electronic absorption spectra of $[Ru(tpy)(R_2bpy)(OH_2)](PF_6)_2$ measured in acetone.

7. Results of photosubstitution reactions

Table S2. Parameters of the photosubstitution reactions for complexes [**7**](PF$_6$)$_2$, [**8**](PF$_6$)$_2$, [**9**](PF$_6$)$_2$, and [**10**](PF$_6$)$_2$.

	[**7**](PF$_6$)$_2$	[**8**](PF$_6$)$_2$	[**9**](PF$_6$)$_2$	[**10**](PF$_6$)$_2$
k_φ (s^{-1})	1.78×10^{-3}	1.10×10^{-2}	1.91×10^{-5}	3.50×10^{-5}
Φ (Einstein $\cdot s^{-1}$)	1.08×10^{-7}	9.95×10^{-8}	1.08×10^{-7}	9.87×10^{-8}
A_e	0.558	0.507	0.501	0.485
$n_{Ru(tot)}$	4.88×10^{-7}	2.36×10^{-7}	1.98×10^{-7}	1.24×10^{-7}
φ_{PS}	0.011	0.038	5.1×10^{-5}	6.5×10^{-5}

i. [**1**](PF$_6$) and [**2**](PF$_6$)

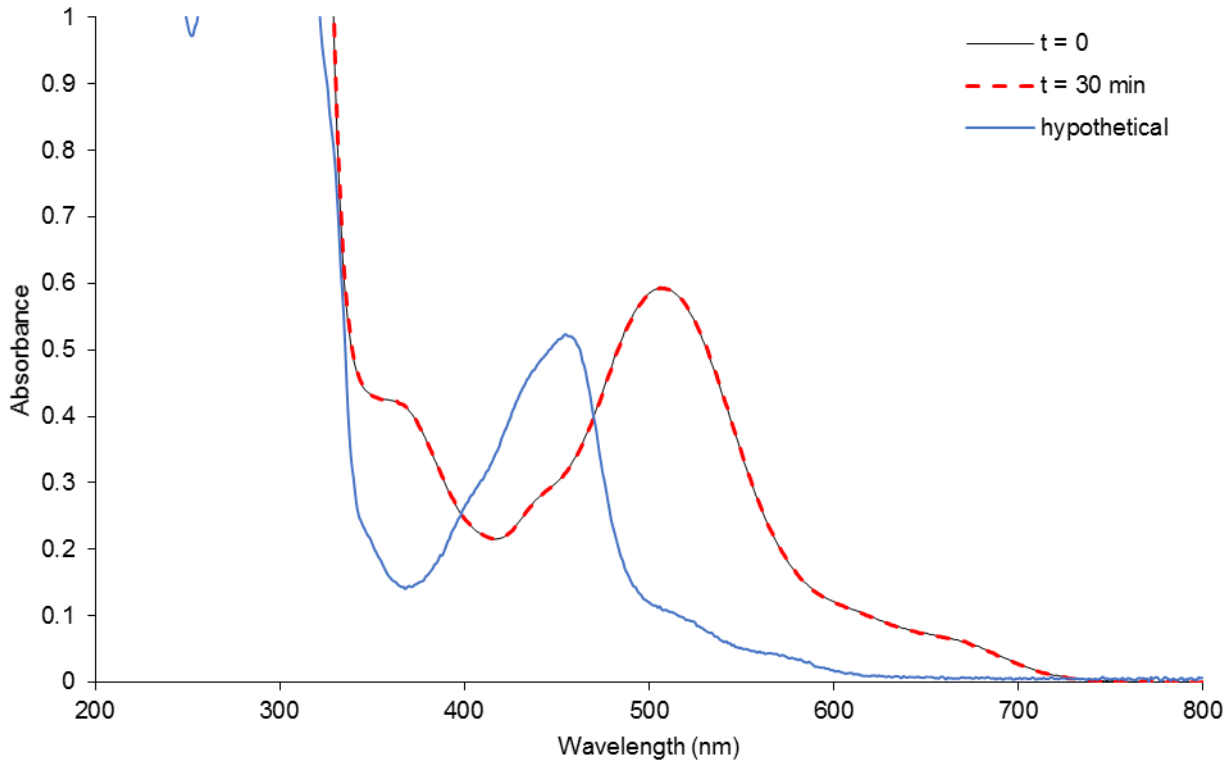

Figure S39. Electronic absorption spectra of [**1**](PF$_6$) irradiated by 490 nm light (photon flux = 1.05×10^{-7} Einstein$\cdot s^{-1}$) in CH_3CN for 30 min. T = 25 °C, $[Ru]_{tot} = 5.1 \times 10^{-5}$ M. Blue line is the hypothetical spectrum of $[\mathbf{5}]^{2+}$ fullly converted from $[\mathbf{1}]^{+}$.

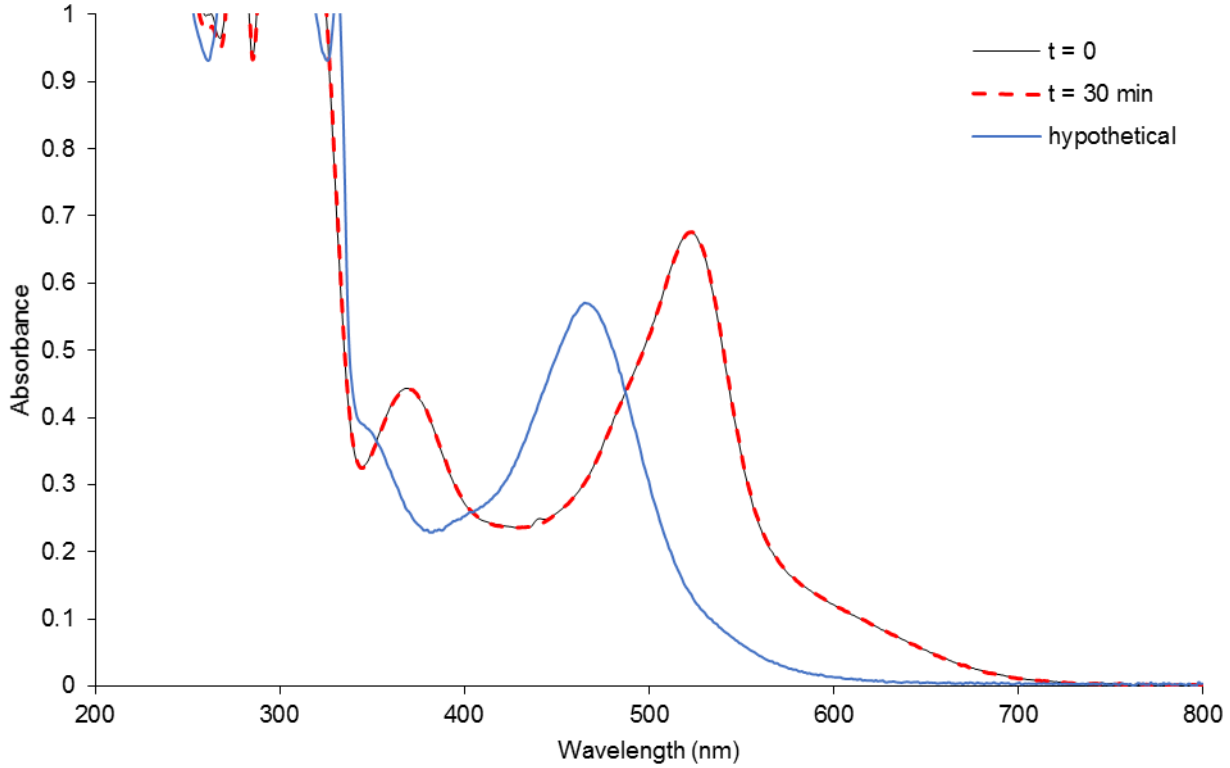

Figure S40. Electronic absorption spectra of [**2**](PF_6) irradiated by 490 nm light (photon flux = 1.06×10^{-7} Einstein·s^{-1}) in CH_3CN for 30 min. T = 25 °C, $[Ru]_{tot} = 5.1 \times 10^{-5}$ M. Blue line is the hypothetical spectrum of $[\mathbf{6}]^{2+}$ fully converted from $[\mathbf{2}]^{+}$.

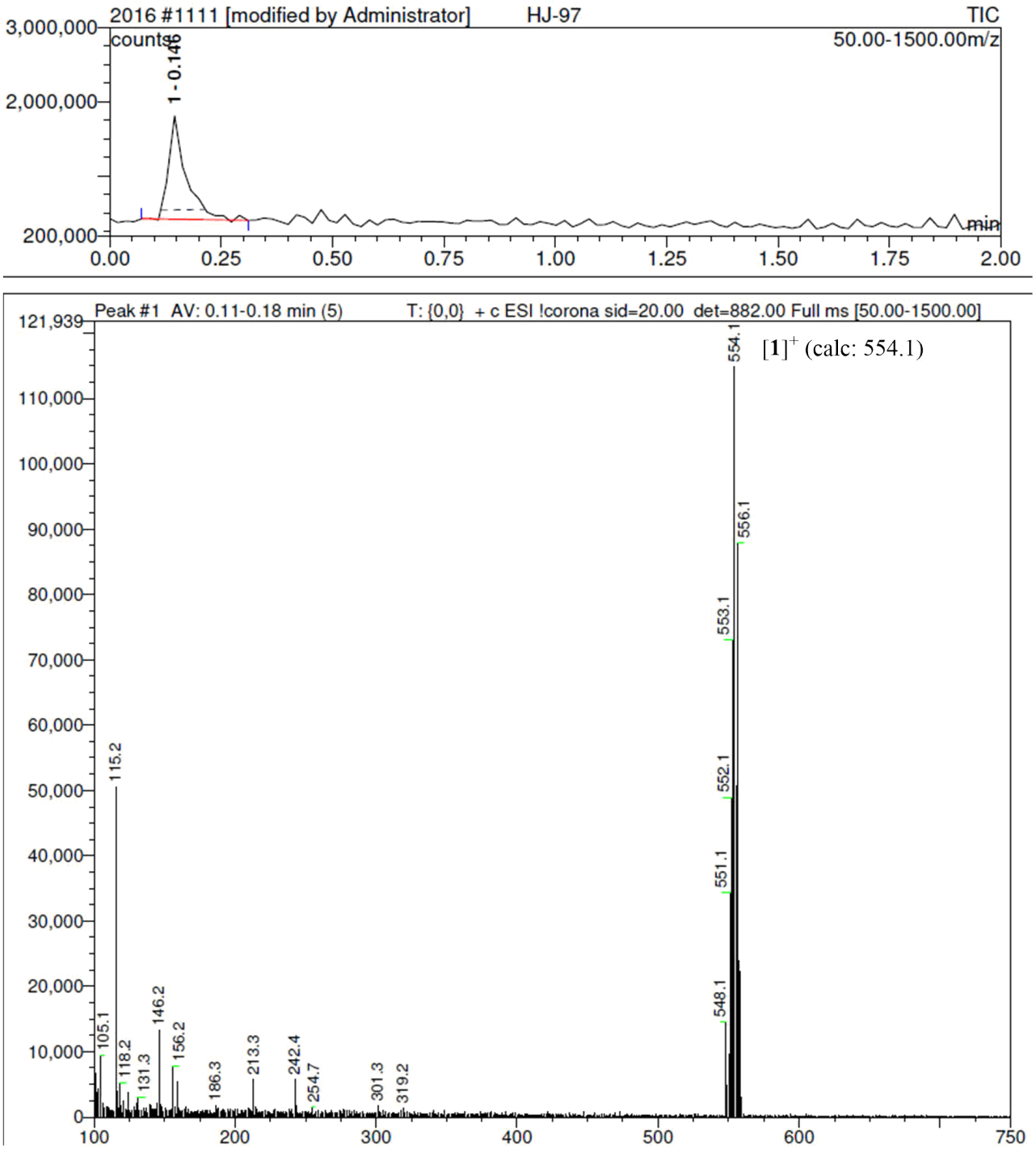

Figure S41. ES-MS of the final solution after the 30-min irradition of [**1**](PF_6) by 490 nm light in MeCN.

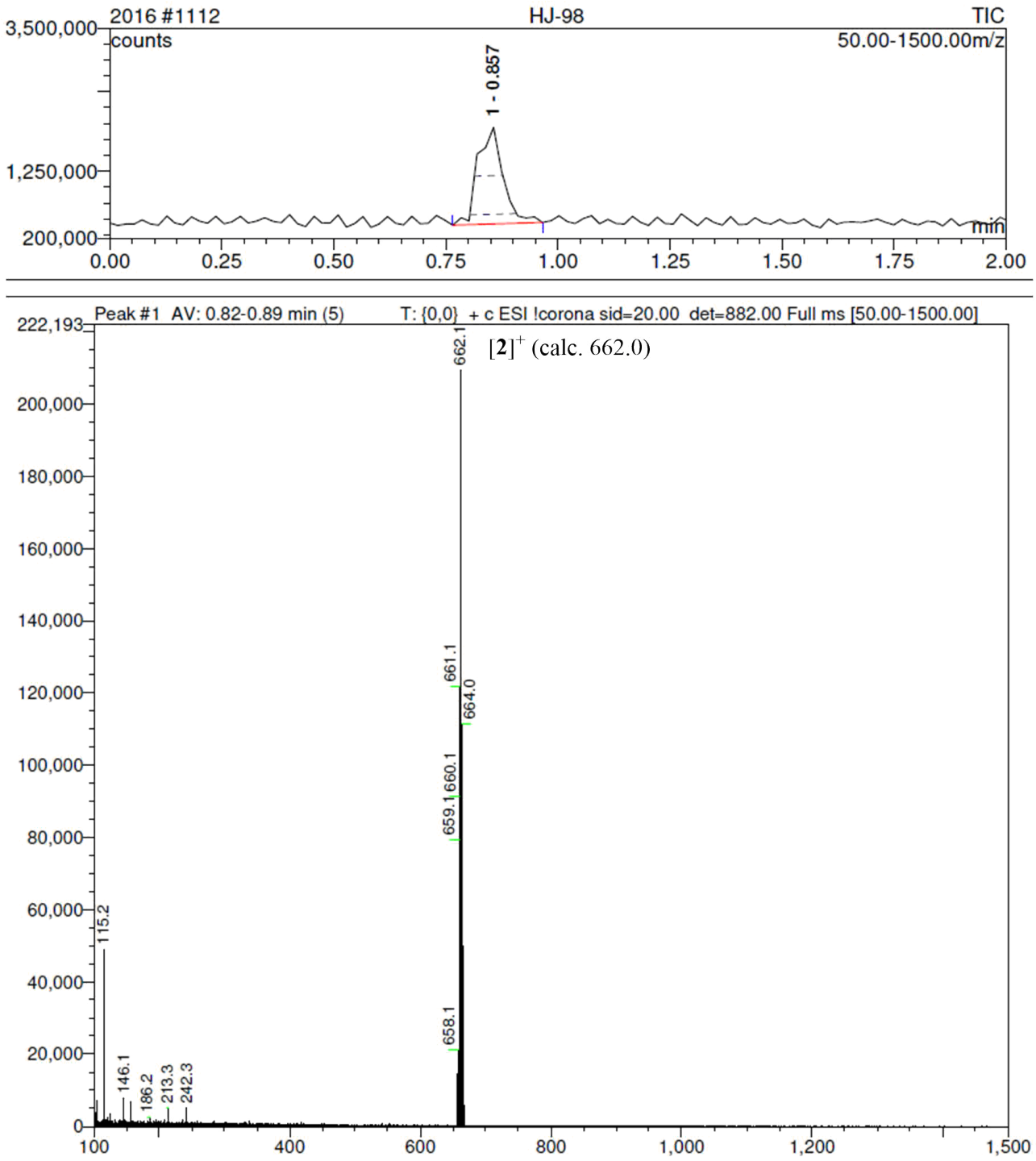

Figure S42. ES-MS of the final solution after the 30-min irradition of [**2**](PF_6) by 490 nm light in MeCN.

ii. [**9**]$(PF_6)_2$ and [**10**]$(PF_6)_2$

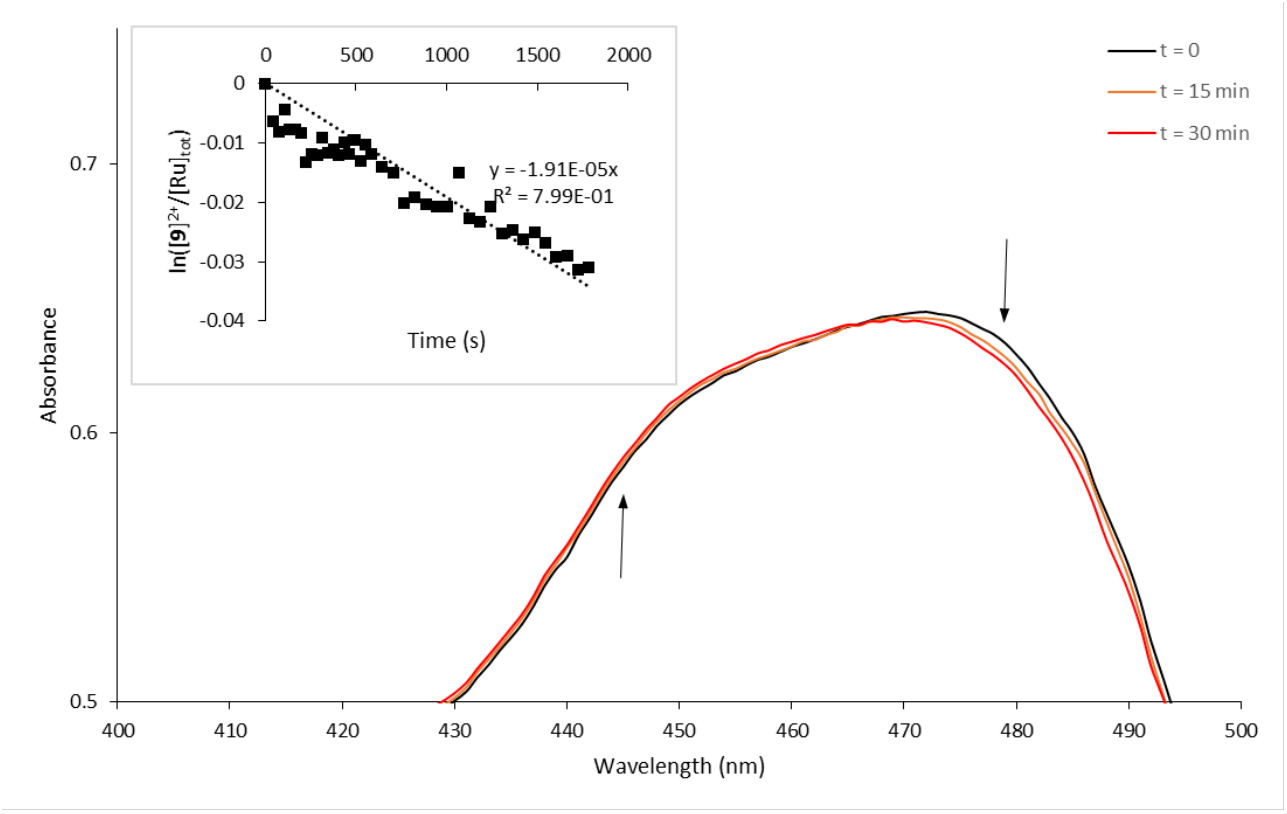

Figure S43. Time evolution of UV-vis spectra of [**9**]$(PF_6)_2$ irradiated by 490 nm light (photon flux = 1.08×10^{-7} Einstein·s^{-1}) in CH_3CN for 30 min. T = 25 °C, $[Ru]_{tot} = 6.6 \times 10^{-5}$ M. The inset is plot of $\ln([\mathbf{9}]^{2+}/[Ru]_{tot})$ versus irradiation time.

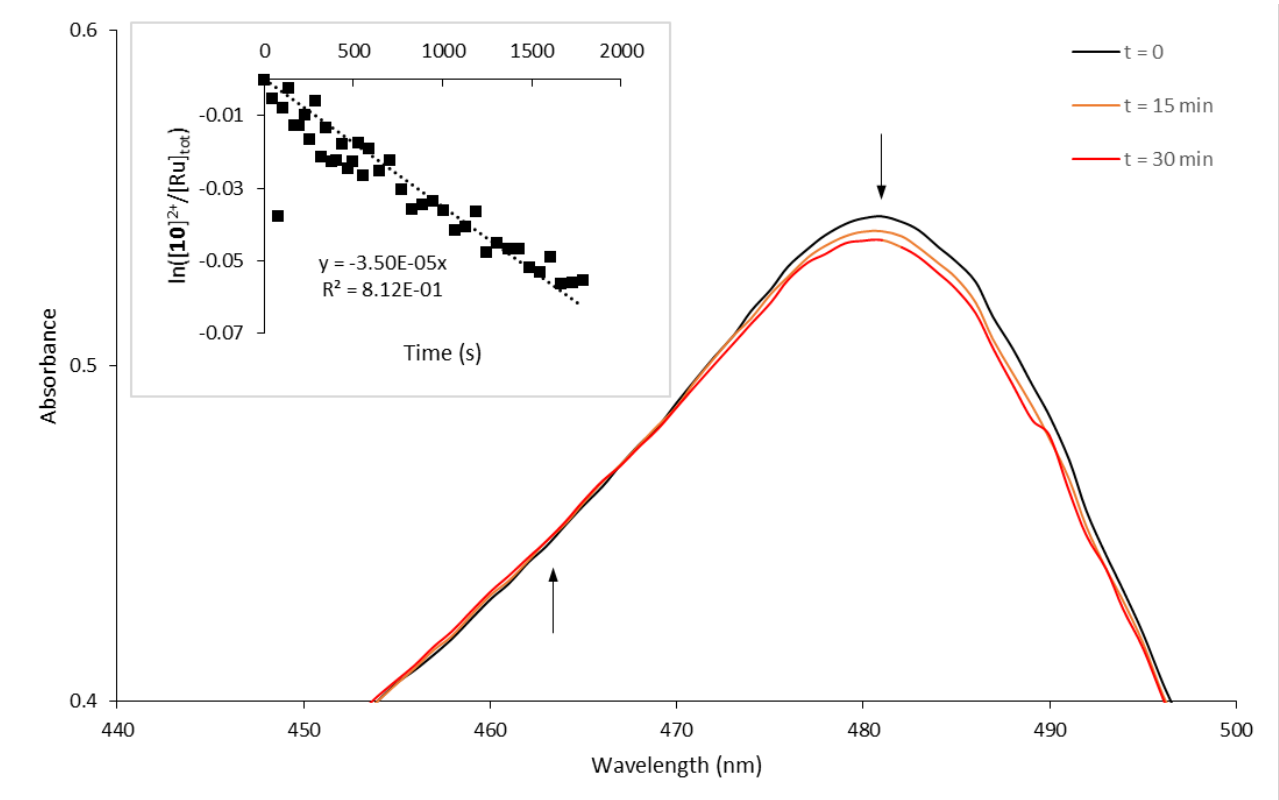

Figure S44. Time evolution of UV-vis spectra of [**10**]$(PF_6)_2$ irradiated by 490 nm light (photon flux = 9.87×10^{-8} Einstein·s^{-1}) in CH_3CN for 30 min. T = 25 °C, $[Ru]_{tot} = 4.1 \times 10^{-5}$ M. The inset is plot of $\ln([\mathbf{10}]^{2+}/[Ru]_{tot})$ versus irradiation time.

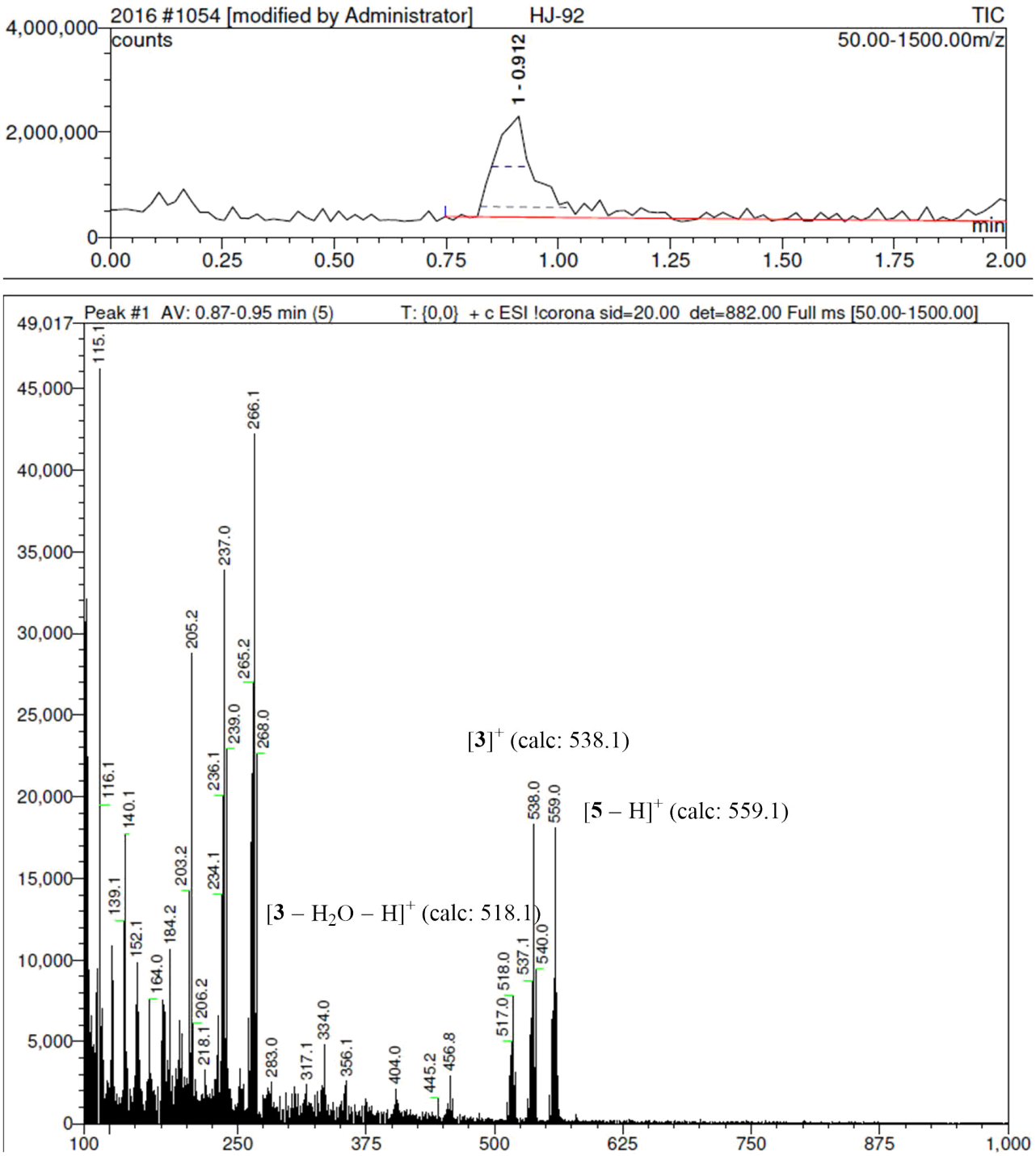

Figure S45. ES-MS of the solution at the final point of the photosubstitution reaction $[\mathbf{9}]^{2+} \rightarrow [\mathbf{5}]^{2+}$.

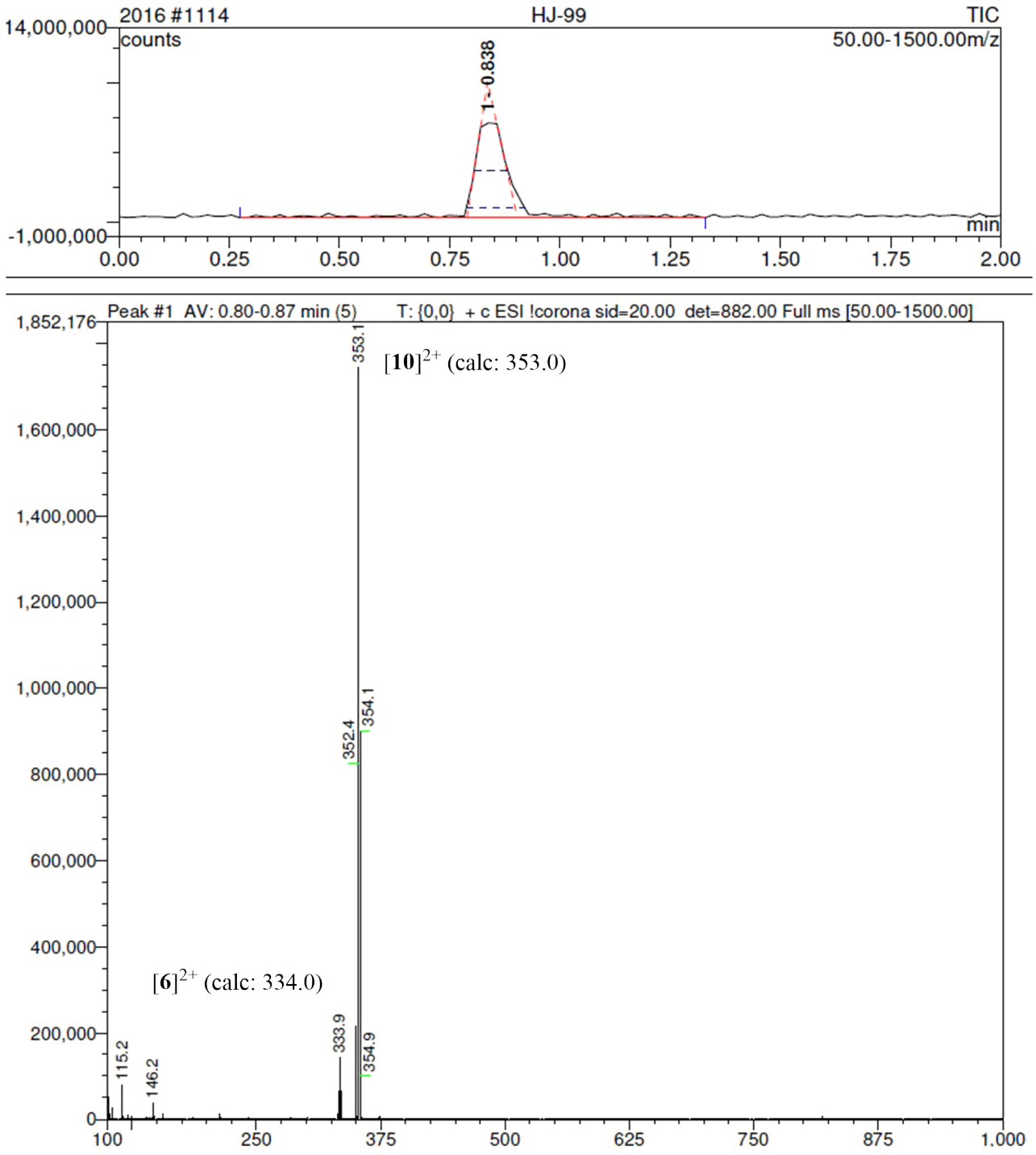

Figure S46. ES-MS of the solution at the final point of the photosubstitution reaction $[\mathbf{10}]^{2+} \rightarrow [\mathbf{6}]^{2+}$.

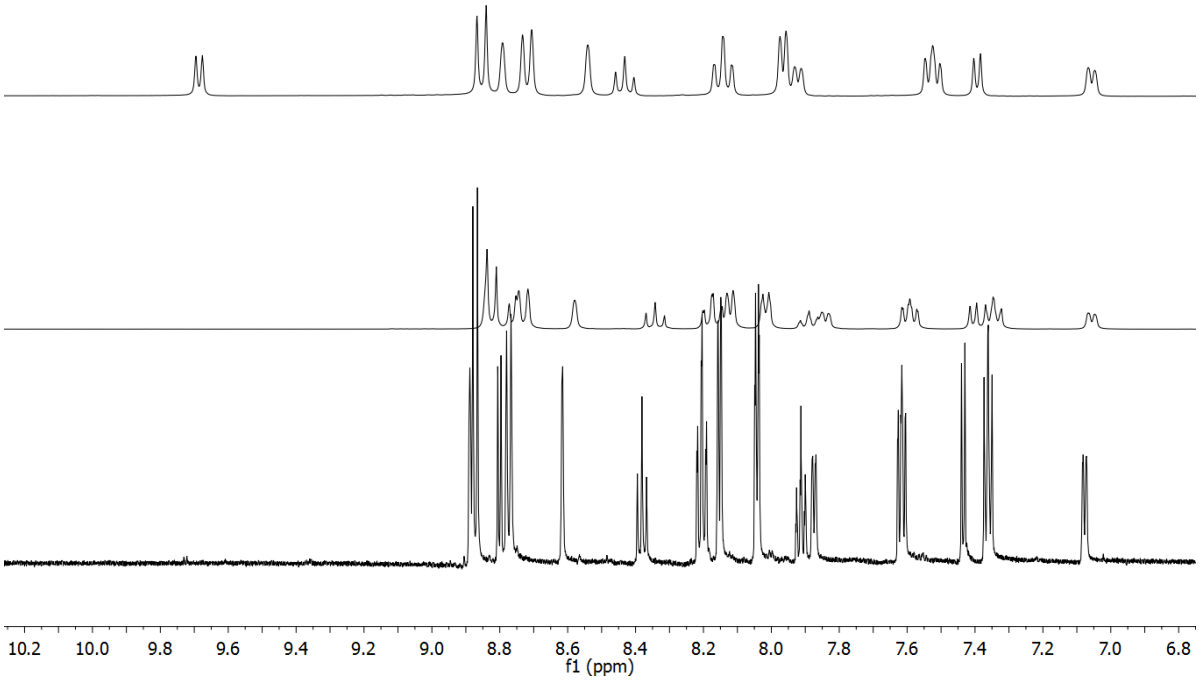

Figure S47. ^{1}H NMR spectra ($(CD_3)_2CO$) of the solution at the final point of the photosubstitution reaction $[\mathbf{9}]^{2+} \rightarrow [\mathbf{5}]^{2+}$ (bottom, 600 MHz), a pure $[\mathbf{9}]^{2+}$ (middle, 300 MHz), and a pure $[\mathbf{5}]^{2+}$ (top, 300 MHz).

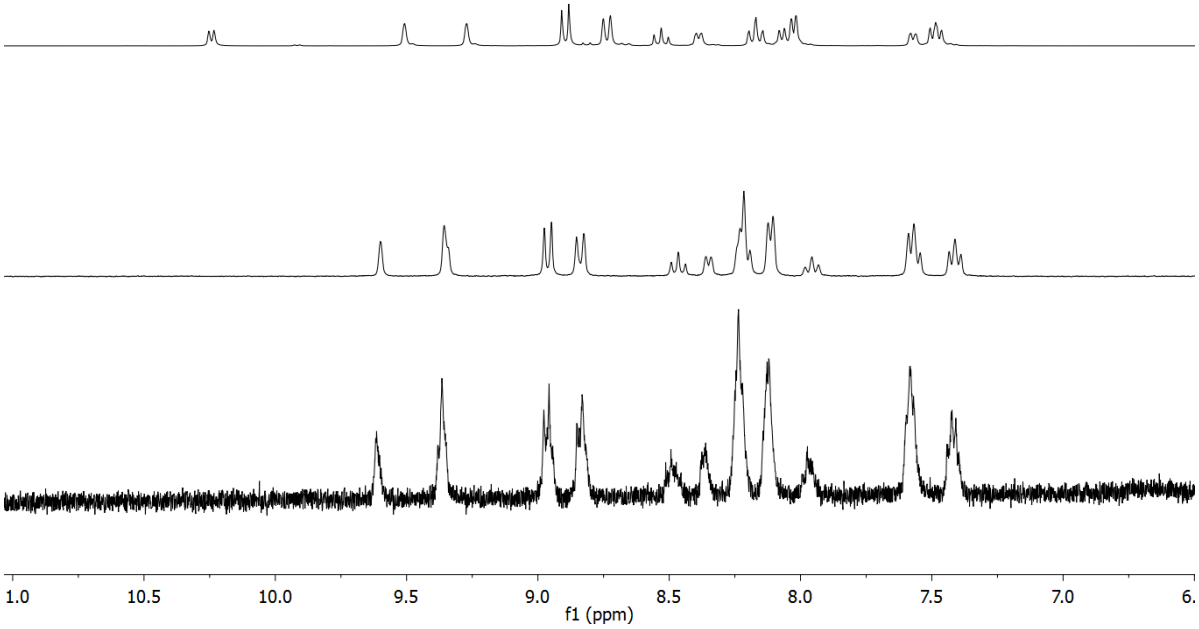

Figure S48. ^{1}H NMR spectra ($(CD_3)_2CO$) of the solution at the final point of the photosubstitution reaction $[\mathbf{10}]^{2+} \rightarrow [\mathbf{6}]^{2+}$ (bottom, 400 MHz), a pure $[\mathbf{10}]^{2+}$ (middle, 300 MHz), and a pure $[\mathbf{6}]^{2+}$ (top, 300 MHz).

iii. [**7**]$(PF_6)_2$ and [**8**]$(PF_6)_2$

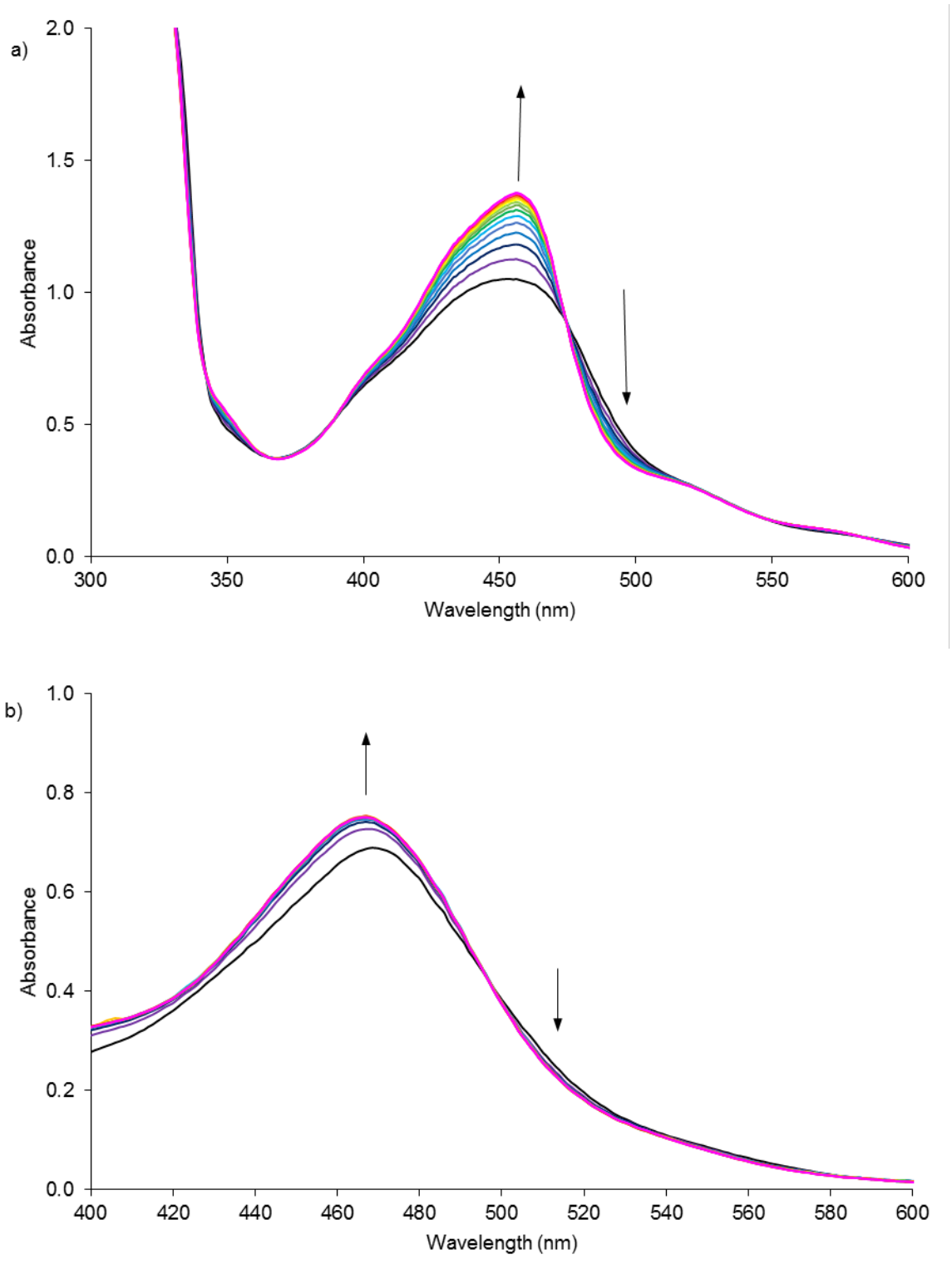

Figure S49. Time evolution of UV-vis spectra of a) [**9**]$(PF_6)_2$ and b) [**10**]$(PF_6)_2$ irradiated by 490 nm light in CH_3CN for 30 min. T = 25 °C. Each spectrum was taken every two minutes.

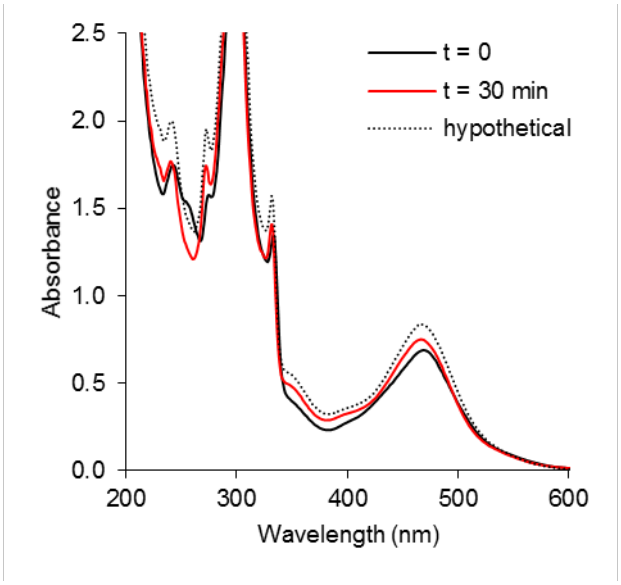

Figure 50. UV-vis spectra of [**8**]$(PF_6)_2$ irradiated by 490 nm light (photon flux = 9.95×10^{-8} Einstein·s^{-1}) in CH_3CN for 30 min. $[Ru]_{tot} = 7.9 \times 10^{-5}$ M. T = 25 °C. Dashed line shows the hypothetical spectrum of full conversion into $[\mathbf{6}]^{2+}$, black line shows initial, and red line shows after 30 min irradiation.

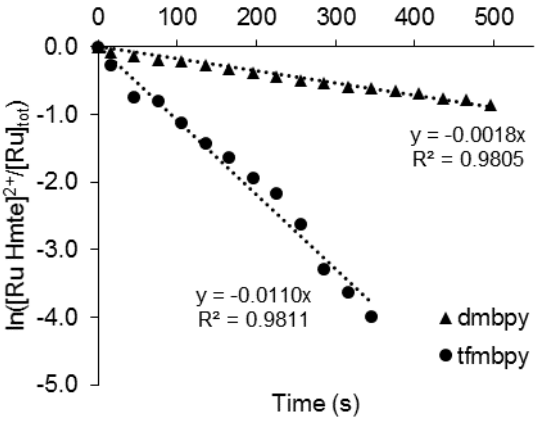

Figure 51. Plot of $\ln([Ru\ Hmte]^{2+}/[Ru]_{tot})$ versus irradiation time for the photosubstitution reactions of complexes $[\mathbf{7}]^{2+}$ and $[\mathbf{8}]^{2+}$ ($[Ru\ Hmte]^{2+}$ = the concentration of either $[\mathbf{7}]^{2+}$ or $[\mathbf{8}]^{2+}$, and $[Ru]_{tot}$ = total concentration of Ru complexes).

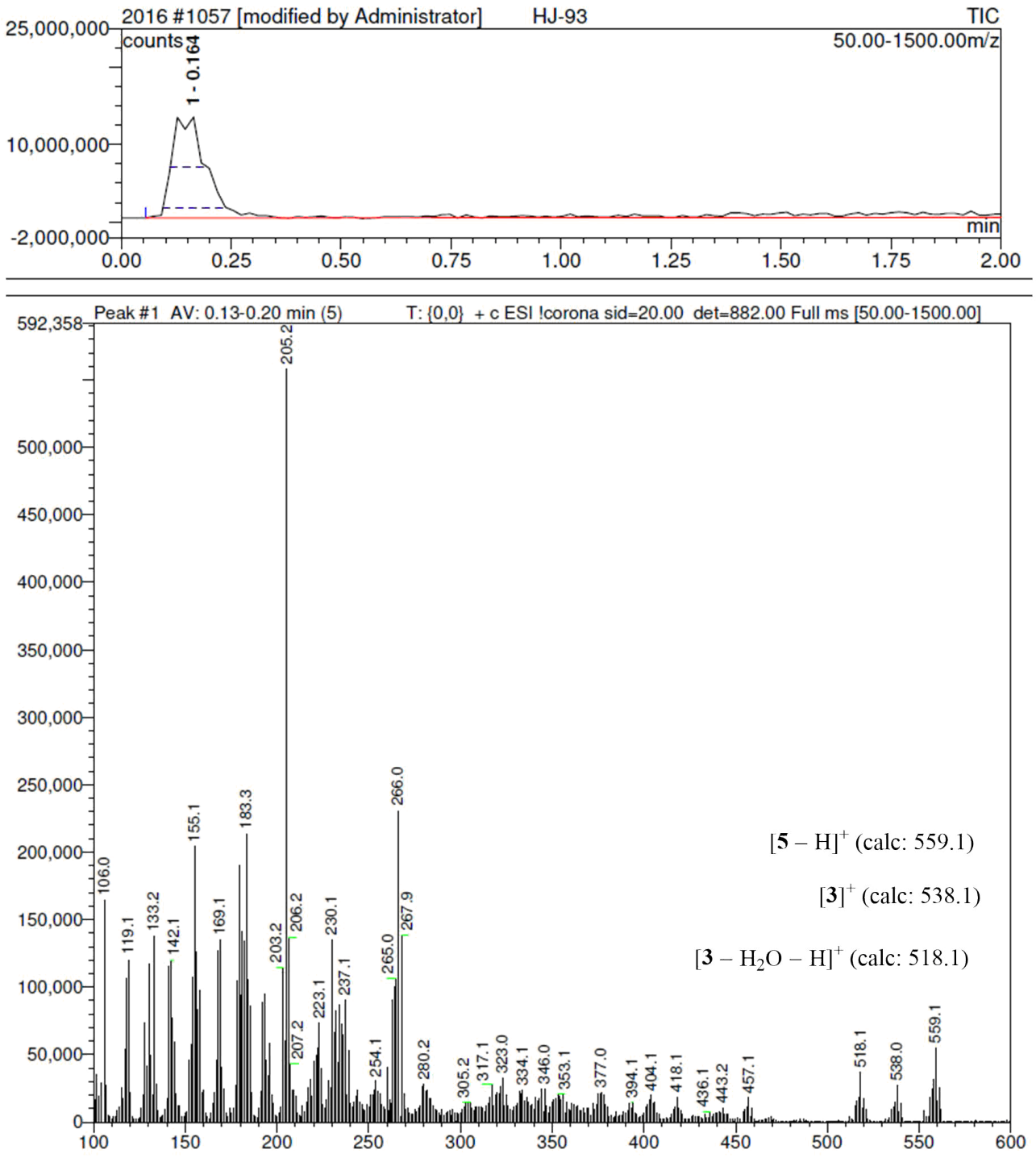

Figure S52. ES-MS of the solution at the final point of the photosubstitution reaction $[\mathbf{7}]^{2+} \rightarrow [\mathbf{5}]^{2+}$.

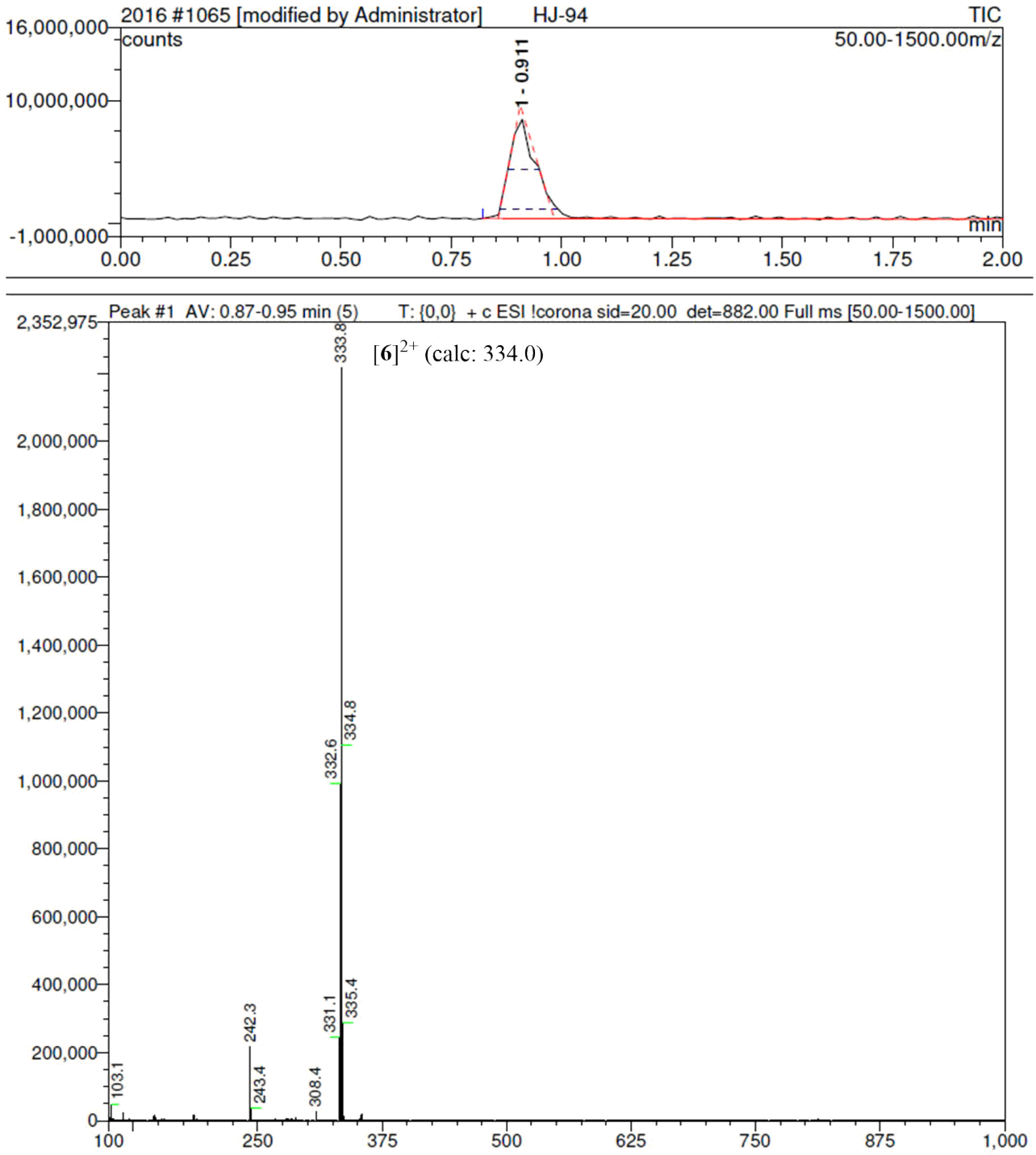

Figure S53. ES-MS of the solution at the final point of the photosubstitution reaction $[\mathbf{8}]^{2+} \rightarrow [\mathbf{6}]^{2+}$.

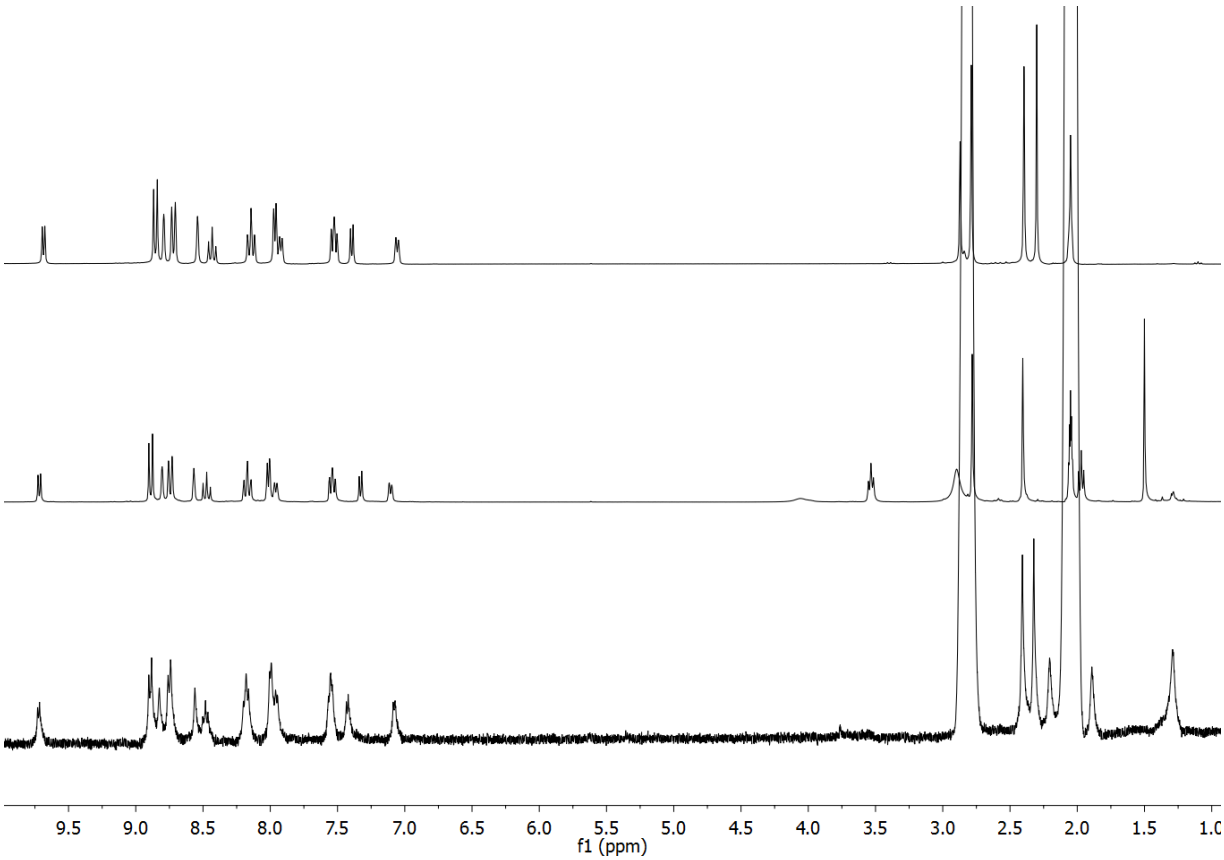

Figure S54. ^{1}H NMR spectra ($(CD_3)_2CO$) of the solution at the final point of photosubstitution reaction $[\mathbf{7}]^{2+} \rightarrow [\mathbf{5}]^{2+}$ (bottom, 400 MHz), a pure $[\mathbf{7}]^{2+}$ (middle, 300 MHz), and a pure $[\mathbf{5}]^{2+}$ (top, 300 MHz).

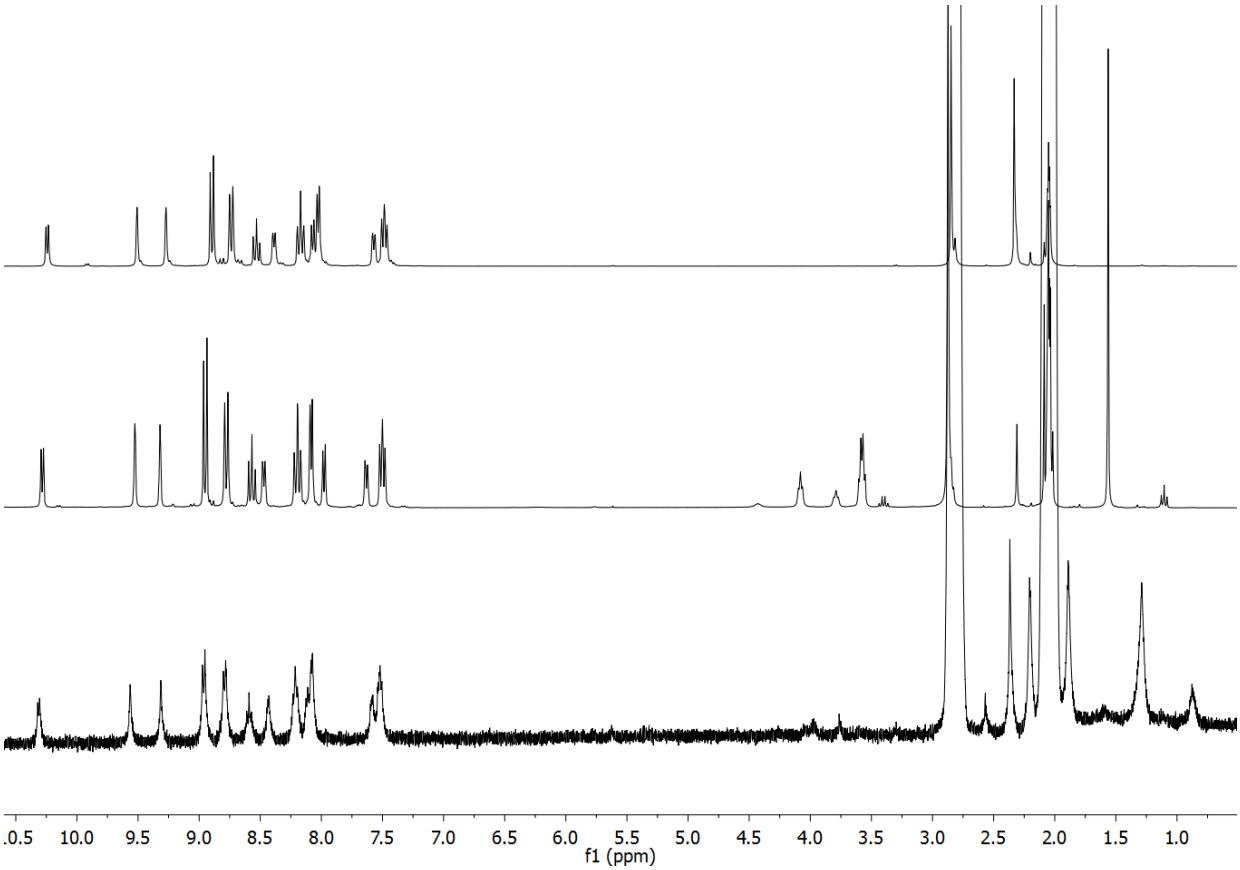

Figure S55. ^{1}H NMR spectra ($(CD_3)_2CO$) of the solution at the final point of photosubstitution reaction $[\mathbf{8}]^{2+} \rightarrow [\mathbf{6}]^{2+}$ (bottom, 400 MHz), a pure $[\mathbf{8}]^{2+}$ (middle, 300 MHz), and a pure $[\mathbf{6}]^{2+}$ (top, 300 MHz).

8. Thermal stability of $[7]^{2+}$, $[8]^{2+}$, $[9]^{2+}$, and $[10]^{2+}$

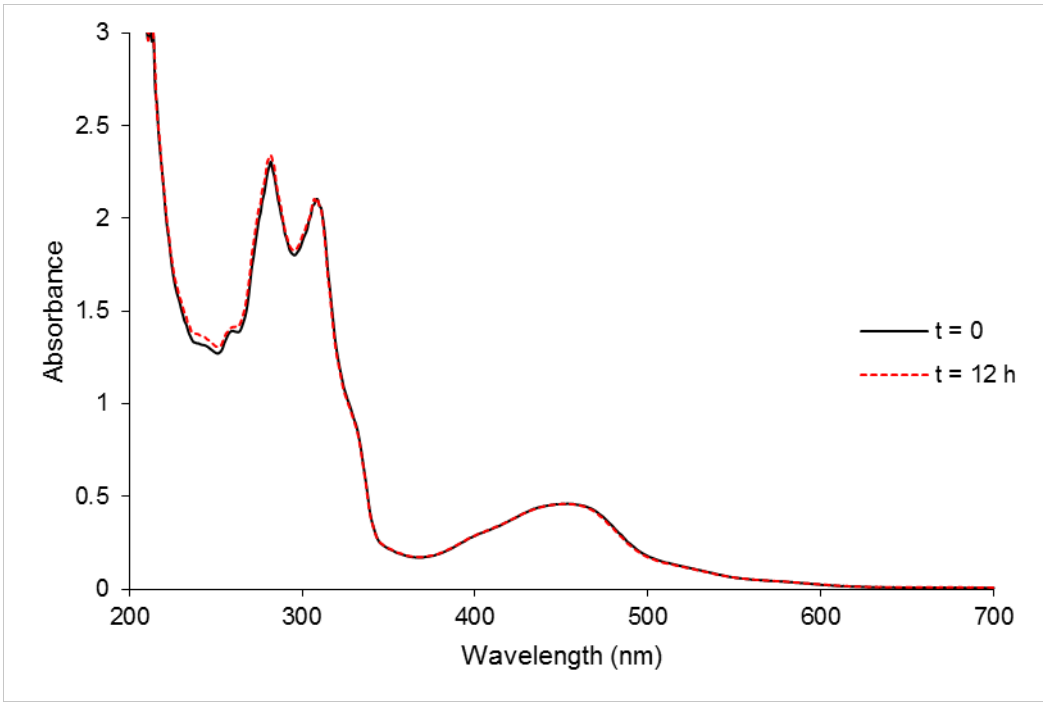

Figure S56. UV-vis spectra of [**7**]$(PF_6)_2$ in MeCN for 12 h.

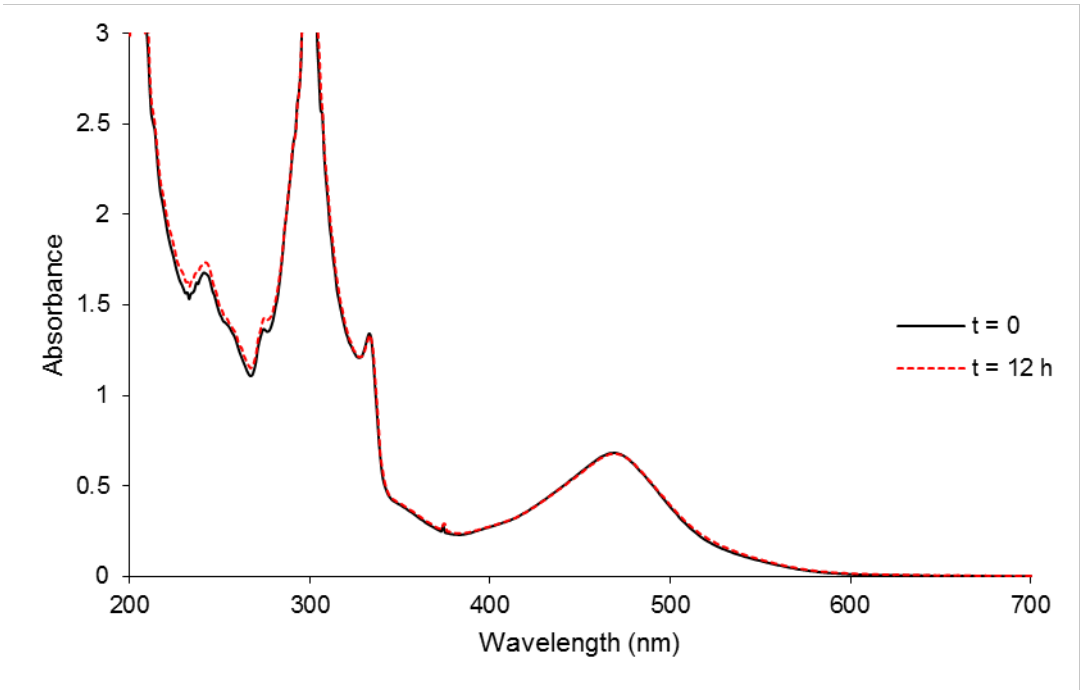

Figure S57. UV-vis spectra of [**8**]$(PF_6)_2$ in MeCN for 12 h.

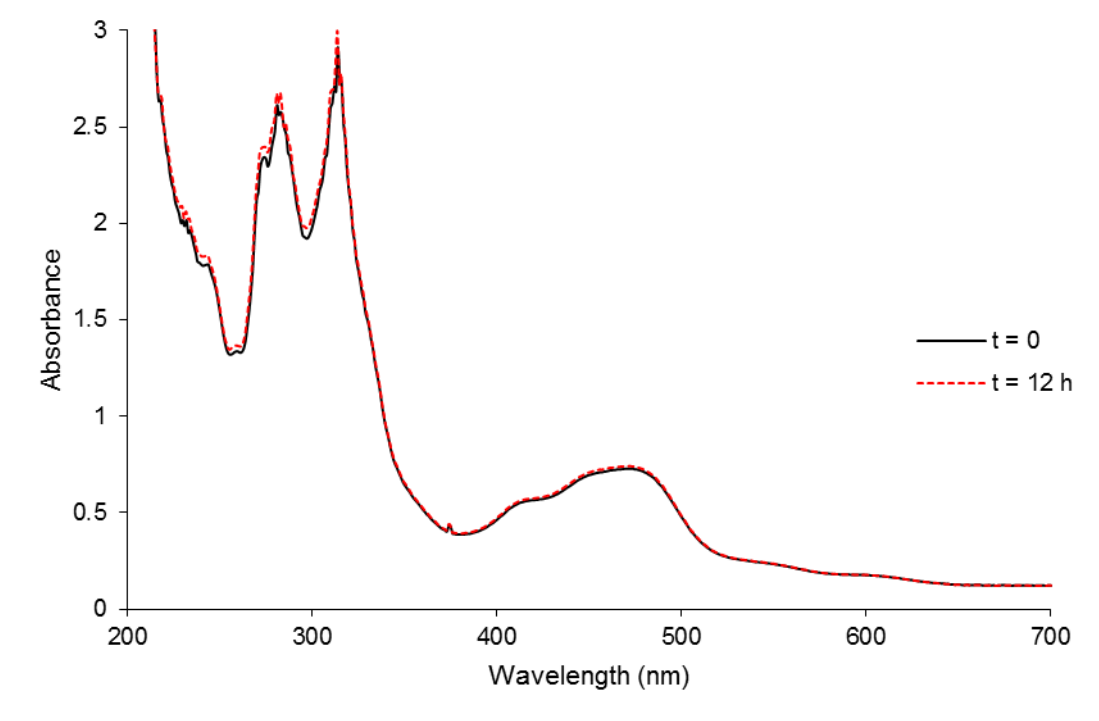

Figure S58. UV-vis spectra of [**9**](PF$_6$)$_2$ in MeCN for 12 h.

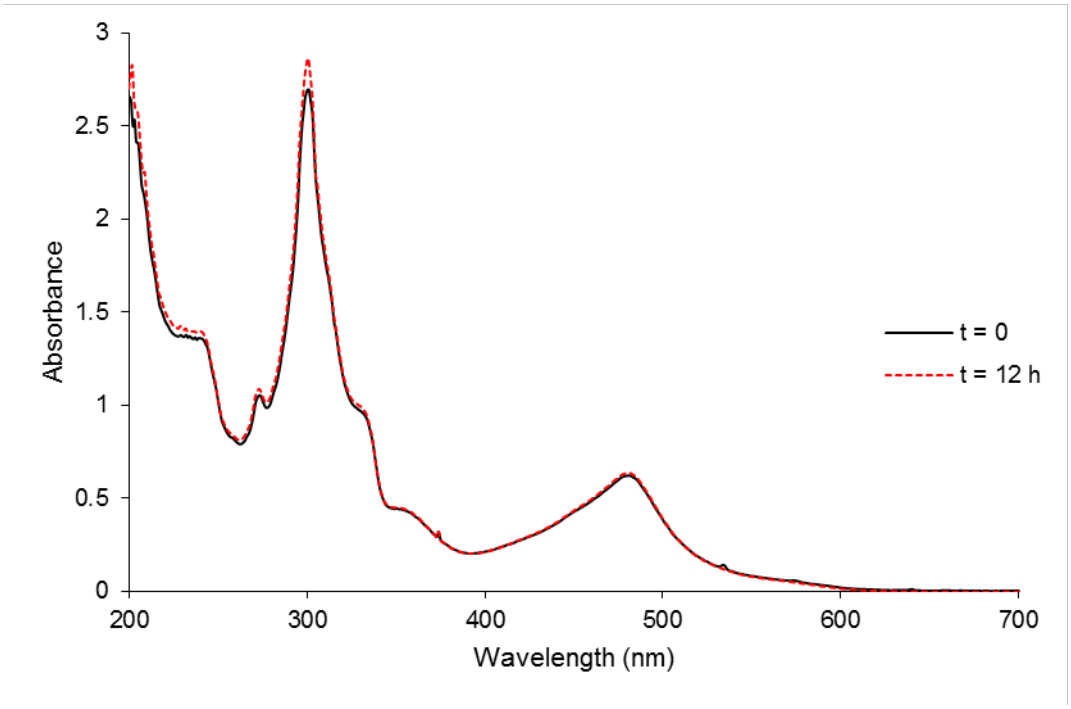

Figure S59. UV-vis spectra of [**10**](PF$_6$)$_2$ in MeCN for 12 h.

9. Photophysical properties

Table S3. Summary of photophysical properties of complexes [**1**]$^{+}$-[**10**]$^{2+}$, including absorbance λ_{max}[a], emission λ_{max}[b], emission quantum yield,[b] and photosubstitution quantum yields[c] (where applicable).

L	[Ru(tpy)(dmbpy)(L)](PF$_6$)$_n$				[Ru(tpy)(tfmbpy)(L)](PF$_6$)$_n$			
	λ_{abs} (nm)	λ_{em} (nm)	Φ_{em}	Φ_{PS}	λ_{abs} (nm)	λ_{em} (nm)	Φ_{em}	Φ_{PS}
Cl$^-$	506	767	8.4×10^{-4}		522	842	7.5×10^{-5}	
MeCN	456	660	8.7×10^{-6}		467	712	1.9×10^{-4}	
Hmte	455	640	3.5×10^{-5}	0.011	468	699	1.1×10^{-4}	0.038
Pyridine	470	669	4.9×10^{-5}	5.1×10^{-5}	481	721	1.9×10^{-4}	6.5×10^{-5}
H$_2$O (in acetone)	488	nd	nd		494	nd	nd	
[Ru(NN)$_3$](PF$_6$)$_2$	458[d]	630[d]	7.3×10^{-2} [d]		460	630	1.0×10^{-1}	

[a] Measurements were made at 293 K in CH_3CN unless otherwise specified

[b] Measurements were made in nitrogen-flushed (10 min) CH_3CN at 293 K.

[c] Measurements were made at 293 K in CH_3CN.

[d] Data from *J. Phys. Chem. A* **1999,** *103,* 7032-7041.

nd = not determined